Design and analysis of a thermoelectric energy harvesting system for powering sensing nodes in nuclear power plant

Jie Chen

Thesis submitted to the faculty of the Virginia Polytechnic Institute and State University in
partial fulfillment of the requirements for the degree of

Master of Science In
Mechanical Engineering

Lei Zuo, Chair

Scott T Huxtable

Brian Vick

Michael D Heibel

12/18/2015
Blacksburg, VA

Keywords: Thermoelectric generator, nuclear power plant monitoring, modeling, Optimization

Design and analysis of a thermoelectric energy harvesting system for powering sensing nodes in nuclear power plant

Jie Chen

ABSTRACT

A thermoelectric energy harvester system aimed at harvesting energy for locally powering sensor nodes in nuclear power plant coolant loops has been designed, fabricated and tested. A complete modeling method that considered the impact of the heat sinks, a heat pipe and the insulating material on system performance has been proposed, and yields good accuracy in power anticipation. The effect of gamma radiation on thermoelectric harvester has been determined experimentally. The system could generate a match load voltage of 4.15V and a maximum output power of 2.25W at a temperature difference of 128.3 ℃ in lab-based experiments with 2 TEM of 1.1” by 1.1”, which was sufficient to power all the electronics designed for this application. An optimization towards the current system was carried out based on the proposed modeling method, the maximum power is then anticipated to reach at 3.78W by integrating 6 TEMs; the maximum efficiency is anticipated to reach to 2.4% by integrating 4 TEMs.

Design and analysis of a thermoelectric energy harvesting system for powering sensing nodes in nuclear power plant

Jie Chen

Public Abstract

In this work, a thermoelectric energy harvester system aimed at harvesting energy for locally powering sensor nodes in nuclear power plant coolant loops has been designed, fabricated and tested. A complete model to analyze the system performance has been proposed, and validated by comparing with experimental results. This model has good accuracy in voltage, power output and can be adapted in any heat sink, heat pipe assisted thermoelectric system. Using this model, an optimization of the thermoelectric energy harvesting system has been performed which is applicable to any energy harvester of this variety.

With experimental validation, the system is capable of generating sufficient energy to power all the sensors and electronical circuits designed for this application. The effect of gamma radiation on this thermoelectric harvester has also been proved to be small enough through radiation experiment.

Contents

List of figures

List of tables

Nomenclature

A	Surface area [m^2]
A_b	Heat sink base plate surface area [m^2]
A_c	Heat sink fin cross section surface area [m^2]
A_d	Heat sink non radiative impact area [m^2]
A_{eff}	Heat sink effective convection area [m^2]
A_{ex}	Heat pipe hot side external area [m^2]
A_f	Heat sink fin area [m^2]
A_p	Heat sink primary area [m^2]
A_{tem}	TEM cross sectional area [m^2]
A_4	Heat pipe cross section of core area [m^2]
C_{sf}	Constant in evaluating Nusselt number
C_1, C_2, C_3, C_4	Constant in ΔT governing equation
c_{pl}	Liquid specific volume heat capacity [J/(kg·K)]
c_{pv}	Vapor specific volume heat capacity [J/(kg·K)]
D	Water/steam pipe diameter [m]
$f(Pr)$	Universal Prandtl number correlation
Gr	Grashof number
$G_{\sqrt{S}}$	Body gravity function
g	Gravitational acceleration [m/s^2]
H_f	Fin height [m]
h_c	Convective heat transfer coefficient [W/(m^2·K)]
h_{ex}	Convective heat transfer coefficient at external surface of heat pipe [W/(m^2·K)]
h_r	Radiative heat transfer coefficient [W/(m^2·K)]
I	Current [A]
K_C	Cold side aggregated thermal conductance [W/K]
K_{C1}	Iterated cold side aggregated thermal conductance [W/K]

K_{ce}	Sealing ceramic thermal conductance [W/K]
K_H	Hot side aggregated thermal conductance [W/K]
K_{PN}	P/N junction thermal conductance [W/K]
k	Thermal conductivity [W/(m·K)]
k_{amb}	Thermal conductivity of ambient air [W/(m·K)]
k_b	Thermal conductivity of heat sink base [W/(m·K)]
k_{ce}	Thermal conductivity of sealing ceramic [W/(m·K)]
k_{in}	Thermal conductivity of electric insulation [W/(m·K)]
k_l	Thermal conductivity of working fluid [W/(m·K)]
k_N	Thermal conductivity of N-type leg [W/(m·K)]
k_p	Thermal conductivity of P-type leg [W/(m·K)]
k_s	Thermal conductivity of source [W/(m·K)]
k_w	Thermal conductivity of wick structure [W/(m·K)]
k_{wl}	Thermal conductivity of wick layer [W/(m·K)]
L	Length [m]
L_b	Length of heat sink base [m]
L_{ce}	Length of ceramic layer [m]
L_N	Length of N-type leg [m]
L_P	Length of P-type leg [m]
l_a	Length of heat pipe adiabatic section [m]
l_c	Length of heat pipe condenser section [m]
l_e	Length of heat pipe evaporator section [m]
l_{eff}	Effective heat pipe length [m]
M	Liquid transport factor [W/m^2]
m	Fin efficiency factor [1/m]
$\dot{m}$	Mass flow rate [kg/s]
N	Fin number (section 6-1) Thermoelectric module pair number (section 4-6 & 6-8)
Nu	Nusselt number
Nu_D	Nusselt number based on pipe diameter

$Nu_{\sqrt{S}}$	Nusselt number based on characteristic length
$Nu_{\sqrt{S}}^{\infty}$	Diffusive limit of a cuboid
n	Pair number of P/N legs
P	Power [W]
P_f	Perimeter of fin cross section [m]
P_o	Power in optimization [W]
P_v	Vapor pressure [Pa]
Pr	Prandtl number
P_1	Iterated power [W]
Q_C	Heat flowing out the module [W]
Q_H	Heat flowing in the module [W]
q	Heat flow [W]
$\dot{q}$	Heat flow rate [W/s]
q_b	Heat flowing in base [W]
q_c	Heat flowing out a P/N junction [W]
q_{ce}	Heat flowing in sealing ceramic [W]
q_h	Heat flowing in a P/N junction [W]
q_{hs}	Heat flowing in heat sink [W]
q_{hs1}	Iterated heat flowing in heat sink [W]
q_{max}	Maximum heat flow through fins [W]
R	Thermal resistance [K/W]; Ideal gas constant (section 4.2)
R_a	Axial thermal resistance in heat pipe [K/W]
R_{al}	Thermal resistance of aluminum plate in module
R_b	Thermal resistance of heat sink base [K/W]
R_{bot}	Thermal resistance of module bottom conductor [K/W]
R_{ce}	Thermal resistance of sealing ceramic [K/W]
$R_{ce,b}$	Thermal resistance of module bottom ceramic [K/W]
$R_{ce,f}$	Thermal resistance of module function layer ceramic [K/W]
$R_{ce,t}$	Thermal resistance of module top ceramic [K/W]

R_{fa}	Heat sink fin area thermal resistance [K/W]
R_{fun}	Thermal resistance of module functional layer [K/W]
R_{hp}	Heat pipe overall thermal resistance [K/W]
R_{hs}	Heat sink overall thermal resistance [K/W]
R_{hs1}	Iterated heat sink overall thermal resistance [K/W]
R_i	Internal electrical resistance of module [Ω]
R_{in}	Thermal resistance of electrical insulation layer [K/W]
R_L	External load resistance [Ω]
R_N	N-type leg thermal resistance [K/W]
R_P	P-type leg thermal resistance [K/W]
R_p	Aluminum adaptor plate thermal resistance [K/W]
R_r	Heat pipe thermal resistance in radial direction [K/W]
R_S	Heat source thermal resistance [K/W]
R_{sp}	Heat sink spreading thermal resistance [K/W]
R_{tem}	Thermoelectric module thermal resistance [K/W]
R_{tg1}~R_{tg4}	Thermal grease resistance at contact surfaces [K/W]
R_{top}	Thermal resistance of module top conductor layer [K/W]
R_{tot}	System total thermal resistance [K/W]
R_1	External resistance at evaporator side of heat pipe [K/W]
R_2	Conductive thermal resistance of wall at evaporator [K/W]
R_3	Conductive thermal resistance of wick at evaporator [K/W]
R_4	Convective thermal resistance at evaporator [K/W]
R_5	Thermal resistance due to mass transfer [K/W]
R_6	Convective thermal resistance at condenser [K/W]
R_7	Conductive thermal resistance of wick at condenser [K/W]
R_8	Conductive thermal resistance of wall at condenser [K/W]
R_9	External resistance at condenser side of heat pipe [K/W]
R_{10}	Axial thermal resistance of heat pipe wall and wick [K/W]
Ra	Rayleigh number
Ra_y	Rayleigh number in y direction of heat sink

$Ra_{\sqrt{S}}$	Rayleigh number with a characteristic length of S
Re	Reynolds number
Re_D	Reynolds number based on pipe diameter
r_i	Radius of inner layer in heat pipe [m]
r_o	Radius of outer layer in heat pipe [m]
S	Characteristic length [m]
S_{opt}	Optimized fin space [m]
T	Temperature [℃]
T_{amb}	Ambient air temperature [℃]
T_C	Cold side temperature of module [℃]
T_c	Cold side temperature of P/N leg [℃]
T_H	Hot side temperature of module [℃]
T_h	Hot side temperature of P/N leg [℃]
T_m	Mean temperature of module [℃]
T_{sink}	Heat sink fin average surface temperature [℃]
T_{sink1}	Iterated heat sink fin average surface temperature [℃]
t_b	Heat sink base thickness [m]
V	Voltage [Volts]
V_o	Open circuit voltage [Volts]
V_1	Iterated voltage [Volts]
W_a	Width of surface without fins on heat sink [m]
W_b	Width of heat sink base plate [m]
y	Y direction length [m]
Z	Figure of merit [1/K]

Greek symbols

α	Seebeck coefficient; summed Seebeck coefficient [V/K]
$\overline{\alpha}$	Average Seebeck coefficient [V/K]
α_P	P-type Seebeck coefficient [V/K]

α_N	N-type Seebeck coefficient [V/K]
β	Thermal expansion coefficient [1/K]
ε	Porosity of heat pipe
ϵ	Spreading ratio of spreading resistance
η	System efficiency
η_f	Fin efficiency
η_o	Optimized efficiency
λ	Latent heat of working fluid [J/kg]
μ_v	Dynamic viscosity of vapor [Pa·s]
μ_L	Dynamic viscosity of liquid [Pa·s]
ν	Kinetic viscosity [m^2/s]
ρ_l	Density of liquid [kg/m^3]
ρ_N	N-type electrical resistivity [Ω·m]
ρ_P	P-type electrical resistivity [Ω·m]
ρ_v	Density of vapor[kg/m^3]
σ	Surface tension [N/m]
ΔP_v	Change in vapor pressure [Pa]
ΔT	Temperature difference [℃]
ΔT_{sat}	Temprature difference
$\Delta T_1 \sim \Delta T_{10}$	Temperature difference due to corresponding thermal resistance in heat pipe [℃]
ΔV	Voltage difference [Volts]

Acknowledgments

First and foremost, I would like to offer my sincerest appreciation and gratitude to my graduate advisor, Prof. Lei Zuo, for his unwavering academic support, collegiality, and mentorship throughout my entire graduate life. He also spent countless hours proofreading my thesis.

It is a genuine pleasure to express my deep sense of gratitude to Prof. Scott Huxtable, Prof. Brian Vick and Dr. Micheal Heibel who served as my thesis defense committee and offered me valuable guidance.

It is also my pleasure to express my gratitude to the staffs in Westinghouse Electric Company, who provided their radiation equipment for the radiation test and helped me through the whole experiment.

I want to extend my gratitude to my lab-mate Mr. Shaoxu Xing who helped me on the design of electrical circuits, Mr. Yongjia Wu who collaborated with me on modeling, Mr. Jackson Klein who helped me with the experimental setup and data recording. I also would like thank other lab-mates who shared research experiences with me over the years.

I would also thank to my family, who consistently supported me on the journey to fulfill my dreams, and who motivated me to surmount all difficulties.

For the ancestors who have paved the path before me upon whose shoulders I stand. Thank you.

This project is funded by the DOE Office of Nuclear Energy’s Nuclear Energy University Programs (NEUP), DE-NE0000747.

1 Introduction

1.1 Motivation

The Fuskushima Daiichi nuclear incident in March 2011 represented an unprecedented challenge on the process monitoring technologies. When severe accidents happen, the temperature, pressure and nuclear radiation level can be extremely high. However, both the off-site and on-site power supply, namely, the power from grids and from back-up batteries, may be depleted or lost as can be seen from Fukushima accident. With massive loss of power across the plant in accident, the backup batteries will be drained up ultimately. As a result, the monitoring system may lose function and therefore it cannot collect immediate information regarding on nuclear plant status.

When both off-site and on-site power become unavailable, the whole plant will be malfunctioned. The Loss of offsite power in nuclear plants is one type of the most frequent incidents in the U.S. A total number of 42 power-out incidents in the U.S from 1997 to 2004 have been recorded. Among these incidents, 24 had caused critical operation problems and 18 more resulted in shutdown of plant. These incidents had the potential to become irreversible accidents if the onsite power source had also failed.

A typical nuclear reactor has 50-200 temperature sensors and 500-2000 pressure sensors to measure various critical parameters for safe and reliable operation. Unfortunately, the conventional sensors including the RTD temperature sensors, capacitance pressure cells and the emerging fiber-optic sensors can be melt or radioactively darkened in harsh environments. Therefore, a design of dual mode langasite (La3Ga5SiO14, a new piezoelectric crystal) thickness shear hybrid pressure/temperature sensor integrated with multi-source energy harvester is proposed.

It is hard to prevent the disasters like Fuskushima accident. However, constructing a self-powered sensing network that could work even after such accidents occur would substantially improve the reliability of sensing system and hereby the reliability of the nuclear power plant. A package of whole integrated design should include a multi-source energy harvester with power management, a langasite resonant dual mode pressure-temperature sensor, and a wireless radio transceiver. The system must be able to sustain in harsh environments and work stably in a relatively long operation period.

1.2 Objectives

The primary goal of this work is to develop a thermoelectric energy harvester, which should be capable of sustaining harsh environment in nuclear power plant and providing sufficient energy to power the electronics, i.e. Langasite T & P dual mode sensor, energy management circuits, wireless communication circuit, signal conditioning circuit. The secondary goal is to develop the circuits stated above and then integrate them with the energy harvester.

1.3 Thesis Organization

The motivation and organization of this thesis are included in the chapter 1. Backgrounds involved in this project such as thermoelectric materials, generators, nuclear reactors, environmental conditions, and sensing requirements are introduced in chapter 2. Then, chapter 3 will be dedicated to the design of thermoelectric harvester, in which the condition and power requirement surveys are carried out and the detailed design is introduced. Detailed analytical modeling of the whole system will be introduced in chapter 4. In Chapter 5, the experimental setup of laboratory-based test and radiation-based test are introduced. Results from both chapter 4 and 5 are shown and discussed in chapter 6. Next, the nuclear radiation mitigation techniques are summarized in chapter 7. The conclusions and future works of this project are stated in the last chapter 8.

2 Background & Literature review

2.1 Energy harvesting

Energy harvesting refers to the process by which extra waste energy from ambient source (vibration, heat, solar and acoustic, .etc.) is converted and stored. The research projects on energy harvesting materials and systems have witnessed a rapid increment during past decades. A large number of innovative applications have been proposed and implemented, ranging from wireless sensing nodes of factories to the adaptive wearable energy harvester on human body, from utilizing kinetic energy of a bulk ocean wave buoy to scavenging electrostatic energy using a microscale cantilever beam [1]. In this section, different energy harvesting approaches will be summarized; and thermoelectric energy harvesting will be introduced in detail.

Different ambient sources offer various energy harvesting methods, as well as various efficiencies. Paradiso summarized the common energy harvesting sources, methods and their conversion efficiencies in terms of power density as shown in the following table [2].

Table 2-1 Comparison of source power density for different energy harvesting application

Energy source	Power density	Note
Ambient RF	<1µW/cm2	Unless near a transmitter
Ambient light	100mW/cm2 (directed exposure to sunlight)	Common polycrystalline solar cells are 16%–17% efficient, standard monocrystalline cells approach 20%.
	100 µW/cm2 (illuminated office)	
Thermoelectric	60 µW/cm2	A typical commercial thermoelectric generator at ΔT=5°C.
Vibrational microgenerators	4 µW/cm3 (human motion ~Hz) 800 µW/cm3 (machines ~kHz)	Highly dependent on excitation (power tends to be proportional to ω3 and y02, where ω is the driving frequency and y0 is the input displacement), and larger structures can achieve higher power densities.
Ambient airflow	1 mW/cm2	Demonstrated in MEMS turbine at 30 liters/min.

Energy harvesting from solar is marked with its convenience and high power density, and has been investigated over decades. However, the relatively large scale in device size and less efficiency at nights render it less effective for continuous powering. Energy harvesting through heat including thermoelectric, pyroelectric, thermionic, etc., which generally provide relatively stable energy source. Vibrational energy harvesting have four basic methods, piezoelectric, electrostatic, electromagnetic and magnetostrictive, among which piezoelectric and electrostatic are more appropriate for small scale energy harvesting, while electromagnetic is appropriate for large scale. Though the existence of radio frequency is ubiquitous, energy harvesting through RF is less popular in most cases because of its relatively low power density. However, it could be adopted for some special use such as powering remote devices, known as wireless charging, when its energy is broadcasted [3].

2.2 Thermoelectric materials

Thermoelectric (TE) materials are a type of materials that can directly convert heat into electricity and vice versa based on thermoelectric effects, a bunch of effects containing Seebeck effect, Peltier effect and Thomson effect. The effect that the heat is converted to electricity at the junctions of P-type and N-type thermoelectric materials is called Seebeck effect. In fact, when the temperature difference is applied to the both ends of P/N junctions, the charge carries (electrons (e^-) in N-type leg, “holes” (e^+) in P-type leg) will be drove to the cold side so that a voltage gradient is formed. Conversely. The Peltier effect refers to the phenomenon that when a current flows through the TE junction, heat will be generated or removed, corresponding to the different directions of current. Peltier effect may also coexist with Seebeck effect, as the heat generation or removal might be caused the Seebeck induced current when external load is attached [4]. Figure 2-1 shows the Seebeck effect and the Peltier effect in a typical P/N junction structure.

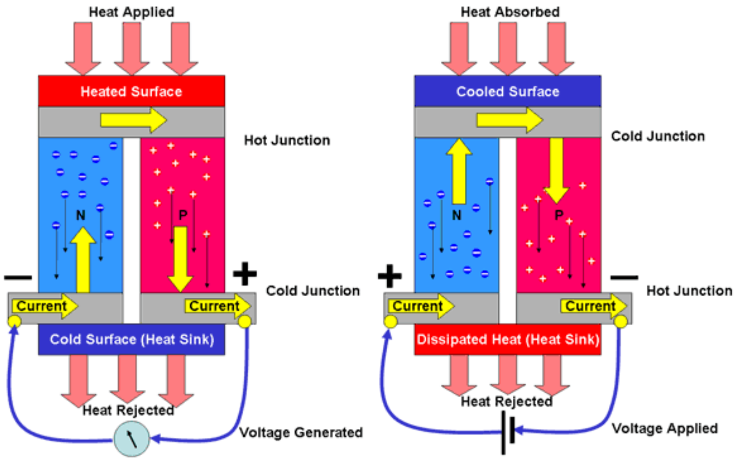

Figure 2-1 Schematic shown of Seebeck effect (left) and Peltier effect (right)

The measure of Seebeck effect is named as Seebeck coefficient, α, with the unit of V/K, which is a temperature dependent property that marks the voltage generation in response to an applied temperature gradient. Indeed, Seebeck coefficient is a function of carrier concentration in TE materials [5]. Seebeck coefficient can be found experimentally as

$$\alpha = \frac{\Delta V}{\Delta T} \tag{1}$$

where ΔV and ΔT are voltage and temperature difference, respectively. The Thomson effect describes the impact of temperature dependency of Seebeck coefficient on the heat flow. To be specific, heat flows into or out of a homogeneous conductor when an electric current flows between two points in the conductor at different temperatures. Due to the fact that Thomson effect is less dominant in thermoelectric energy harvesting process, it is sometime neglected.

Figure of merit value, ZT, is another important indicator of thermoelectric material, and is defined as

$$\mathrm{Z} = \frac{\alpha^2 \sigma}{k} T \tag{2}$$

where σ and k, are the electrical conductivity (Ω·m) and thermal conductivity (W/m·K) of TE, respectively [6]. The ZT value determines how efficiently a given material can convert heat into electricity. From the above equation, we can see that to harvest more energy, a higher electrical conductivity is favored since it ensures a larger current; a lower thermal conductivity is favored since it leads a larger temperature difference; and a more elevated Seebeck coefficient is favored since it would directly enhance the voltage generation per unite temperature gradient. Therefore, the major way to optimize a TE material is to increase power factor $\alpha^2\sigma$ by either increasing carrier concentration (or electrical conductivity) or by decreasing the lattice thermal conductivity (or the overall thermal conductivity) [7].

There are several types of semiconducting materials that can be regarded as thermoelectric materials. Generally, alloyed semiconductors with high carrier concentration are the most efficient bulk thermoelectric materials, since the alloying process undermines the heat conduction among lattices, especially when heavy elements are employed, such as Bi, Te, Pb, and Sb[8]. Conventional bulk alloying materials, such as Bi2Te3, PbTe and SiGe, have been investigated for decades. Among all the materials, Bi2Te3 is the most popular TE material used for low temperature range (<300 ℃) with a decent ZT value of 1.0 [9]. PbTe, or PbTe-Sb series, are more frequently used in moderate temperature range; while SiGe is more suitable for elevated temperature range. Doping of bulk material with other elements is another effective method to reduce lattice thermal conductivity without influencing electrical conductivity. However, the research in conventional materials achieved a modest improvement until the of nanostructured materials, such as, superlattices, nanowires and quantum dots (ranging from 2-D structure down to 0-D structure), were introduced and experimentally proved [10-11, 13-15].

Nanostructures, or the low-dimensional structures, when employed in the conventional materials, effectively reduce the lattice thermal conductivity while moderately change Seebeck coefficient and electrical conductivity [12]. Then, a net increase of ZT can be achieved. Venkatasubramanian achieved a ZT value of 1.2 with Bi_2Te_3 superlattice material under room temperature, marks the first attempt to improve the ZT value of conventional material Bi_2Te_3 by using nanostructure approach [13]. Boukai successfully fabricated silicon nanowires, measured the thermoelectric related properties, and then reported a 200 times increment in the ZT value when comparing to its bulk material [14]. Herman reported that a quantum dot superlattices material PbTe had a ZT value of 0.9 under room temperature, doubled from the bulk results [15].

Another approach to improve ZT value other than going nanostructured is synthesizing new complex materials, which generally have low lattice thermal conductivity [9]. Skutterudites, Half-Heusler and clathrates are the major new materials whose attributes are closed to PEGC (phonon glass-electron crystal) material, an ideal classification of material [16]. Containing void space in its lattice structure, skutterudites ($CoSb_3$), are usually thermally conductive, and have a ZT of only 0.8 at 600K. However, filling the "caged" structure with dopant such as Yb, La, Ba will effectively reduce thermal conductivity, and yield higher ZT as 1.2, and even higher with multiple dopants [17-18]. Clathrate and Half-Heusler are crystals with large unit cells. A Czochralski-grown clathrate $Ba_8Ga_{16}Ge_{30}$ possess a remarkably high ZT value of 1.63 at 1100K; and a spark-plasma-sintered $Hf_{0.6}Zr_{0.4}NiSn_{0.98}Sb_{0.02}$ is reported to have ZT value of 1.0 at 1000K [19-20]. The ZT value of different bulk materials including nanostructured bulk materials are summarized in the following Figure 2-2.

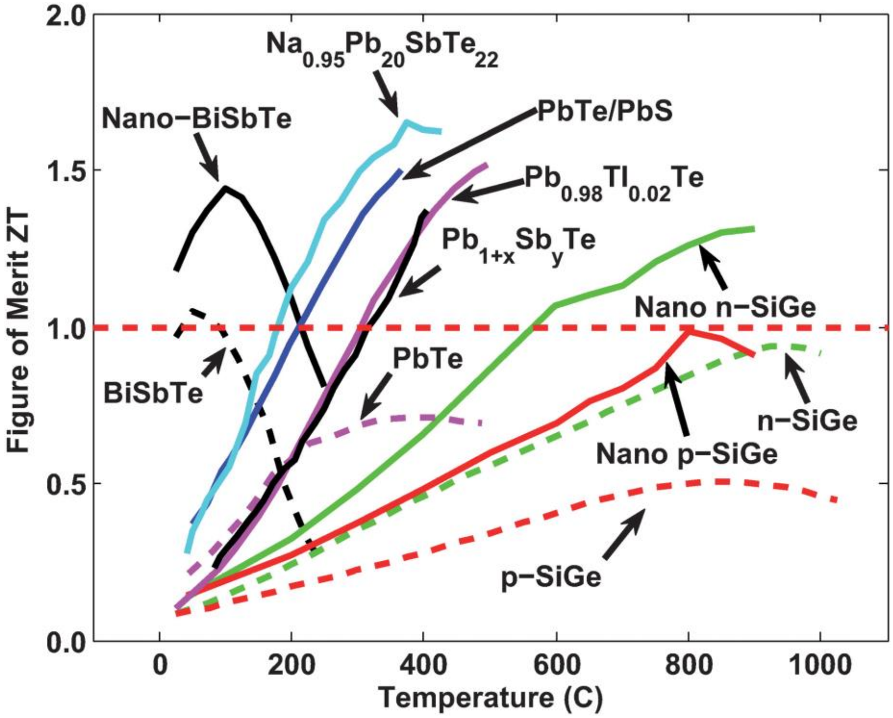

Figure 2-2 ZT value of current state of the art TE materials versus temperature [9]

The development of microelectromechanical system (MEMS) fabrication techniques facilitates the research in low-dimensional TE materials, not only for the conventional materials, but also for the complex new materials. A bunch of thermoelectric materials were fabricated with MEMS methods with a clear reduction in their lattice thermal conductivity. Then, more state-of-art MEMS energy harvester prototypes were developed [21-24].

2.3 Thermoelectric generator applications, and modeling

Thermoelectric module is a solid-state heat engine that consists of a bunch of P/N legs connected electrically in series and thermally in parallel. It has significant advantages such as: being mechanically simple with no moving parts, operating quietly and stably, and being environmentally benign. However, its less efficiency (normally less than 5%) restricts its extensive usage except special usage in aero engineering, military, and medical applications, such as spacecraft powering, sensing nodes powering [25]. New applications were proposed and attempted recently, such as wearable thermoelectric generator for small carry-on electronics powering, solar thermoelectric, and exhaust pipe energy scavenge [26-28].

The operational principle of a typical thermoelectric generator and a typical commercialized module used in this project are shown in figure 3.

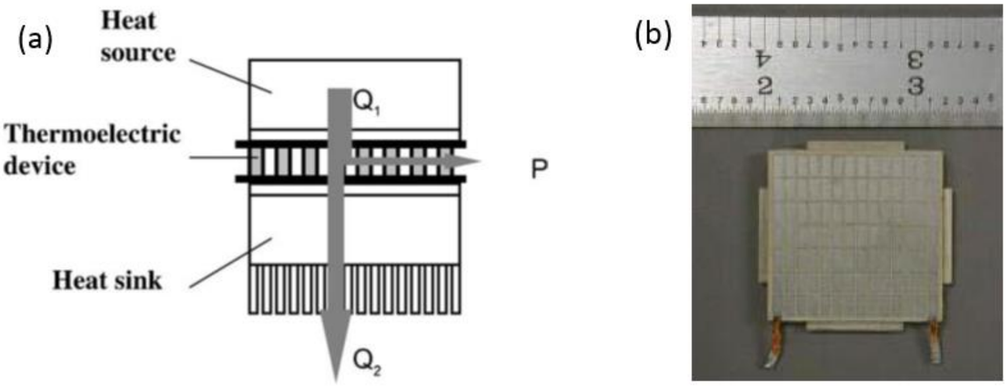

Figure 2-3 (a) schematic of thermoelectric generator operation and system arrangement [25]; (b) a typical commercialized product purchased from Hi-z Technology Corporation

From the above figure, one can easily figure out the system arrangement of a thermoelectric generator. Besides the thermoelectric module (TEM), a heat source and a heat sink is needed at both sides of TEM to finish a thermal circuit. The source provides an elevated temperature or an input heat flow at the hot side; while the cold side heat sink serves as heat dissipation tool so that a lower temperature can be achieved.

Given that this application is targeted on harvesting energy on steam/water pipeline of nuclear power plant, the review of TEG devices and modeling will mainly focus on on-pipe thermoelectric generator. There are two typical on-pipe thermoelectric energy harvester applications, vehicle exhaust pipe and water (steam) pipe in factory, based on the pipe size difference. The major restriction in harvesting thermal energy from high temperature pipe is TEG's sustainability in high temperature conditions. As stated above, Bi_2Te_3 TEM remains the major commercially available product for its low cost and high reliability. However, most Bi_2Te_3 TEMs has a maximal working temperature of about 250°C. According to Fu's work, exhaust pipe inner wall temperature may be more than 500 ℃ [28]. A typical secondary loop of nuclear power plant may have temperature up to more than 300 ℃ [29]. Thus, two options could be selected to extend the usage of Bi_2Te_3 modules here: one approach is to use TEGs made of high temperature sustainable TE materials; another one is to design a system whose functional part has a temperature under the upper operational temperature limit of current TEGs.

For exhaust pipe thermal energy harvesting application, there are a large quantity of publications on device level design and modeling. The first attempt to harvest energy from exhaust pipe by TEG was conducted in 1963 [30]. Then, various prototypes have been developed. Haidar builted a TEG system with commercially available modules, in which an aluminum spreader block was designed to mount TEM on the exhaust. With 4 TEM, a maximum power of 12.2W was generated under a temperature difference of 237 ℃ [31]. Then several heat exchanger integrated design were developed. Ikoma developed a SiGe module with 8 pairs of legs for an elevated temperature usage, and a generator system with heat exchanger on a rectangular exhaust pipe. 72 modules were integrated and yielded a maximum power of 35.6W with a 563 ℃ temperature difference [32]. Thacher constructed a similar structure with 16 HZ-20 thermoelectric modules and reported a maximum power output of 255.1W with a lower temperature difference of 173.72 ℃ [33]. Hsu developed two generations of exhaust-based thermoelectric generators, and conducted extensively study on system performance in low-temperature range with prototypes. A decent power output of 44.13W was achieved with temperature difference of 88.3 ℃ in low temperature range for the first generation with 8 TEM, and a moderate power output of 12.41W was achieved with temperature difference of 30K [34-35].

Another type innovative design is heat pipe assisted TEG for exhaust system, which theoretically provide better heat conductance between source and TEM. Relatively less amount of works have been done for this type of design. Heat pipe is a heat-transfer device that takes the advantage of phase change to efficiently transport heat from one end to another end. A typical heat pipe should have low thermal resistance and thus serves as a super thermal conductor. Detailed description of heat pipe working principle will be discussed in the following chapters.

Goncalves developed an artwork of heat pipe assisted thermoelectric generator, which consists of multiple heat pipes inserted into an exhaust pipe, thus the heat in the fluid will be absorbed by the heat pipe and then conducted to the hot end of TEM [36]. A concept artwork is shown below.

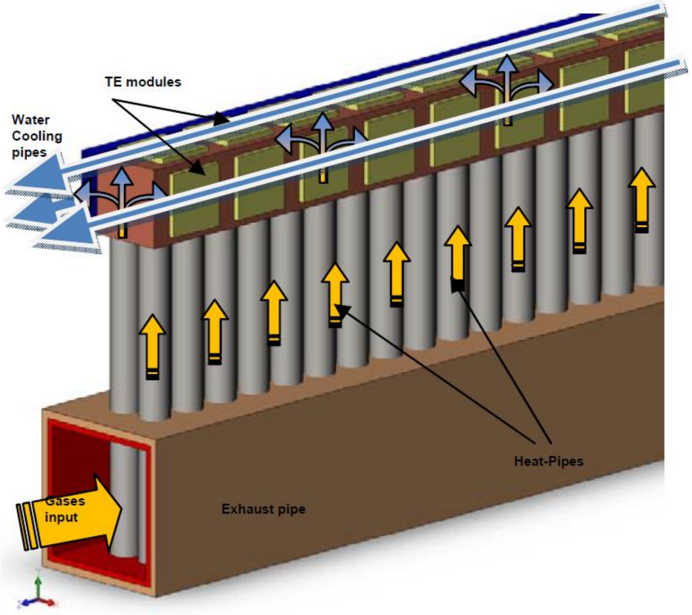

Figure 2-4 Artwork of an exhaust-based thermoelectric generator using heat pipes [36].

Further, Goncalves proposed to use variable conductance heat pipe instead of normal heat pipe for this application to achieve a passive control of temperature at the hot side of TEM. Then a series of study focusing on the feasibility of using variable conductance heat pipe in this application have been conducted theoretically and experimentally by this group [37-39]. Different versions of prototypes were built and tested with a considerably good temperature control results achieved. Heat pipe assist thermoelectric generators for other applications, have also been developed recently. Date studied how to implement heat pipes at the cold side of the TEM, and connected the hot side to a solar heated water tank [40]. At peak solar hours, 0.756 kW·h of electricity can be generated with 36 TEMs. KIM studied a loop thermosiphon assisted TEG with different working fluid in the looped heat pipe [41].

For steam pipe thermal energy harvesting application, moderate works have been done possibly because the installation of thermoelectric harvester on existing part is difficult. However, the relatively constant temperature difference between most operating steam/water pipes and ambient air still renders thermoelectric generator a promising tool for energy scavenging. Dell constructed a prototype that can be implemented onto the steam pipe and steam meter robustly [42]. Also, two special heat pipe assisted heat sink are connected to the TEG to further reduce thermal resistance at the cold side of TEG. The approximate power output is 6.9W with 4 commercial modules as the temperature gradient reaches to 63 ℃. Remeli made an attempt to utilize heat pipe in the design to harvest energy between two pipes with different temperatures [43]. Maharaj extend the use of TEG to the industrial plants, and fabricated a TEG with two units: one is a flat surface TEG unit mounted on the combustion chamber wall, while another one is on steam pipe [44]. Tewolde proposed a design that could be directly mounted onto the outer surface of steam pipe, and reached to a match load power of 1.0W during real application based test that is enough to power the data transmitting system [45].

It should be noticed that there are various methods to harvest energy with fluids, while thermoelectric is only approach. Efforts have been made to harvest energy via vibration. During pipeline operation period, flow induced vibration exists on both pipe and inner structure when vortex happens or flow direction changes. A bunch of works have been done on harvesting vibrational energy using piezoelectric materials [46-48]. One advantage of using piezoelectric energy harvester is its relatively smaller size comparing to TEG. Additionally, kinetic energy of fluid can also be used to generate electricity by using electromagnetic energy converter. However, using electromagnetic method always prerequisite moving part-rotating impeller which may cause unwanted resistance to the flow. Hoffmann designed an electromagnetic energy harvester for smart metering, and collected 720 mW of power during with a maximized flow rate of 20 L/min [49].

On the thermoelectric generator mathematical modeling side, plentiful models and reviews are published [50-56]. Zhao summarized the current materials, modeling methods and applications of thermoelectric generator [50]. Fraisse summarized the prevailing modeling techniques for thermoelectric process in an order of complexity, and compared the accuracy yielded with all models [51]. The simplest model, which assumes the heat flow in the whole thermal circuit is constant, can be found in Priya's book [1]. The thermoelectric process is indeed coupled by heat conduction, Seebeck effect, Peltier effect, Thomson effect and Joule heating, among which heat transfer effect has a major impact on the system. A mathematical modeling considering the heat transfer's influence was given by Chen [52]. In most cases, the modeling of thermoelectric process does not include the Thomson effect since its impact on overall TEG performance is low. Chen built a sophisticated model to investigate the impact of Thomson effect, and derived close-form solutions for the power output and efficiency in terms of Thomson coefficient [53]. Sahin worked on the impact of leg geometry on the thermoelectric generator, and indicated that trapezoid shape could improve the efficiency but reduce the power generation [54]. Rodr ǵuez used Finite element method to solve the thermoelectric generator analytically [55]. Optimization could be achieved when a mathematical modeling is done. Chen performed an optimization towards a two-stage thermoelectric generator by searching for the optimum heat transfer surface and the pair numbers using non-equilibrium thermodynamics and finite-time thermodynamics [56]. Rowe extended the investigation of modeling from the physical processes to the evaluation of a thermoelectric generator via manufacture quality factor, power density, cost effectivity and reliability [57].

Besides the modeling for a single module, several mathematical models have been presented for integrated designs for specific applications [58-60]. Hsiao investigated the detailed mathematical modeling techniques for waste heat recovery from automobile engines based on an integrated design [58]. Gou conducted modeling and experimental study on a design targeting on harvesting energy from a flow channel, and optimized the design by enhancing heat transfer capacity at cold side [59]. He designed a solar heat pipe energy harvesting unit and performed a steady state modeling for the prototype [60].

Apart from mathematical modeling, numerical modeling using commercial finite element software has widely being used in analyzing thermoelectric in both module and device level [61-63]. Jaegle modeled thermoelectric transient process and the structure mechanic in one pair of P/N leg [61]. By applying different boundary conditions, the voltage, power and deformation outputs were studied. Wang used a numerical method to examine the influence of heat sink on the system performance, and hereby optimized the design of heat sink to reach a maximum the TEG output power [62]. Weng built up a thermoelectric generator targeted on harvesting waste heat from an automobile, and did a numerical simulation to evaluate the output power in different geometry [63].

2.4 Nuclear reactors

A nuclear reactor is a device used to generate electricity by utilizing a controlled nuclear chain reaction. Heat generated from nuclear fission or fusion is transported to the working fluid (normally water) and then converted into electricity by turbines [64]. Nuclear reactors are used to generate electricity in nuclear power plants and propulsion system of ships. Regardless of the types of reactors, they share same key elements: fuel, moderator, control rods, pressure vessel and coolant loop, steam generators, containment. Functions of above elements are summarized here: For fuel material, Uranium is the fuel for most reactors; a moderator is a material used in core to slow down fast neutrons to initiate more fission; control rods are rods that inserted with neutron absorbing material to control reaction rate; coolant loops are circulations with liquid to transport energy from core to generator; containment is the structure around the reactor and associated steam generators to protect outside from radiation [65].

Based on the moderator material, there are graphite-moderated reactors, water moderated reactors, light-element-moderated reactors, among which water moderated reactors are the major type and can be divided further as heavy-water reactors and light-water reactors. Nuclear fission reactors can also be classified into three types by their coolant materials as water cooled reactors, liquid metal cooled reactors and gas cooled reactors. Water cooled reactor can be further divided into light water and heavy water cooled reactors, where light water cooling is the dominant type [66].

All current nuclear power plants in commercial operation are summarized in the following Table 2-2 [65]. The fundamental distinction between the PWR and the BWR is: In the BWR coolant moderator, pressure is lowered so that water is boiled to form steam and passed directly to the turbine-generator, whereas in the PWR the coolant moderator is maintained above saturation pressure by a pressurizer so that almost no boiling occurs in the reactor [67].

Table 2-2 Summary of current nuclear power plants in operation

Reactor type	Number	Fuel type	Coolant	Moderator
Pressurized water reactor (PWR)	277	enriched UO_2	water	water
Boiling water reactor (BWR)	80	enriched UO_2	water	water
Pressurized heavy water reactor (PHWR)	49	natural UO_2	heavy water	heavy water
Gas-cooled reactor (AGR & Magnox)	15	natural U & enriched UO_2	CO_2	graphite
Light water graphite reactor (RBMK & EGP)	11	enriched UO_2	Water	graphite
Fast neutron reactor (FBR)	2	PuO_2 & UO_2	liquid sodium	none

3 Design

3.1 Design base—working conditions survey

3.1.1 Estimation of temperature profile in nuclear power plant

Since PWR and BWR are the major types of nuclear power plant. The investigation on the temperature source for energy harvesting will be focused on these reactors. A typical BWR layout is given in the following Figure 3-1 [68].

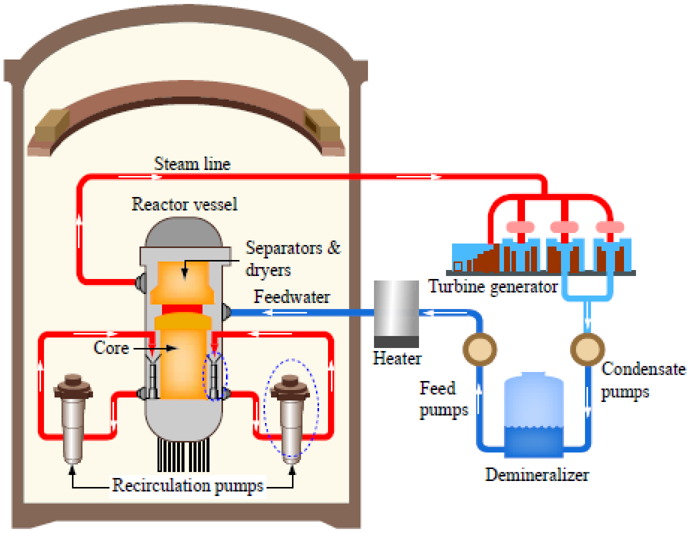

Figure 3-1 Boiling water reactor (BWR) plant layout

A typical BWR has only one coolant circle for power generation in which the water is at lower pressure (75 times of atmosphere pressure) to ensure the temperature in the core to be around 285 ℃. Cold water will be heated by a heater and then pumped to the core inlet. Then steam will come out from core outlet and then transport its heat to turbine generator where steam is cooled and flows back to the heater to finish the cycle. Typical temperature at inlet and outlet are 278.3 ℃ and 287.2 ℃, respectively. The steam temperature is remained at 287.2 ℃ after it flows out from core outlet.

Comparing with BWR, there are more coolant loop cycles in a PWR, a primary cooling circuit where water flows to the core of the reactor under very high pressure, and a secondary cycle in which steam is generated in steam generator and flows to turbine. The plant layout of a typical PWR is shown in Figure 3-2.

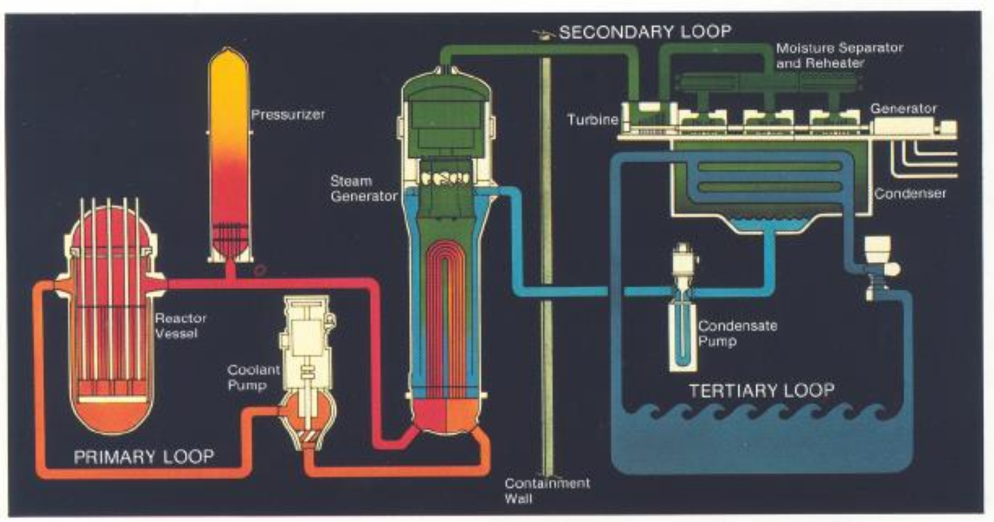

Figure 3-2 Pressurized water reactor (PWR) plant layout [67].

The designed temperature of a PWR reactor vessel is about 343 ℃. The temperature at reactor coolant pump suction is about 275 ℃ to 292 ℃. Water in the reactor core reaches about 315 ℃ to 325 ℃, why means pressure must be kept at about 150 times of atmospheric pressure to prevent water from boiling. A steam generator separates the primary loop and secondary loop, where the inlet temperature is around 325 ℃ under elevated pressure of 150 to155 bar, and the outlet temperature is reduced to about 292 ℃ after releasing pressure [67].

The temperature profile of BWR and PWR coolant loop will are summarized in follow Table 3-1.

Table 3-1 temperature profile of coolant system in PWR and BWR.

	Reactor core inlet/outlet temperature (℃)	Primary loop mean temperature (℃)	Primary loop mean Pressure (bar)	Secondary loop Mean temperature (℃)
BWR	278/287	287	75	Not specific
PWR	275~292/315~325	317	155	292

3.1.2 Investigation of radiation environment in nuclear power plant

Radiation is hazardous to electrical devices since it may damage both passive components and semiconductors in the circuits [69]. Therefore, to implement the self-powered wireless sensor nodes in the nuclear power plant, an investigation of radiation type and dose rate in a nuclear power plant is necessary.

Among different types of radiations, gamma radiation and neutron radiation are the main types that need to be considered in the nuclear power plant, since they are by far the most penetrating ones [70]. Generally, radiation resides in various stages of nuclear power cycle: fuel rod fabrication, reactor operation, spent fuel reprocessing and storage. The doses level in the fuel fabrication can be neglected since it is below the sensitivity amount of most electronic devices. But, the doses around reactor core and spent fuel are more distance dependent, so that it can be extremely high within the core of reactor or spent fuel storage.

Houssay summarized the radiation dose rate distribution near both commercial advanced gas cooled reactor (CAGR) and pressurized water reactor (PWR), and the radiation levels during the different phases of spent fuel processing [69]. The radiation dose rates in a typical CAGR and a PWR are summarized in the following tables.

Table 3-2 Radiation rates in a typical CAGR

Locations	Operation state	Gamma dose rate(Gy/h)	Neutron dose rate (Gy/h)	Neutron flux (n/cm^2/h)
In core	On load	10^7	10^7	10^{17}
	Shut down	10^4	10^{-1}	10^{10}
Outside the radial shield	On load	10^2	10	$5\cdot10^{10}$
	Shut down	10^{-3}	Negligible	10^4
Above the pressure dome	On load	10	1	10
	Shut down	$5\cdot10^{-3}$	Negligible	Negligible
Coolant loop	On load	$5\cdot10^{-1}$	Negligible	Negligible

Table 3-3 Radiation rates in a typical PWR

Locations	Gamma dose rate (Gy/h)	Neutron dose rate (Gy/h)
Pressure vessel annulus	10^2	$3 \cdot 10^2$
Coolant loop area	$5 \cdot 10^{-1}$	Negligible
Outside loop area	$2 \cdot 10^{-3}$	$2 \cdot 10^{-4}$

The processing of spent fuel needs special care since the gamma radiation dose rates may range from background radiation to as high as 10^4 Gy/h during different processing steps. Vitrification step may generate the largest dose rate, while the rates in mechanical cutting, washing and chemical processing are milder. Comparing to gamma radiation, neutron radiation’s impact is negligible. The storage of spent fuel process produce less radiation dose rate compare to the processing phase. Klas Lundgren recorded the dose rates near the BWR spent fuel canister with different wall thickness, the gamma radiation dose rate at the outer surface of encapsulation may still as high as 20Gy/h even after cooling down for 20 years [71].

3.1.3 Target site for installation

At the initial stage of this project, several potential candidates of target locations were chosen such as reactor vessels, steam generators (PWR), pumps, and steam pipes of primary loop and secondary loop (PWR). To narrow down the targeting sites, criteria need to be made:

(1) Accessibility and safety: The self-monitoring sets need to be installed in places that are accessible and safe. For example, adding external structures to the reactor vessels is usually prohibited. Besides, the electronics will lose functions quickly under the extreme intense radiation dose rate.

(2) Enough energy: To ensure the system can harvest enough energy to power all electronics, sites must have stable energy sources (heat and vibration). For example, even the vessel has very high inside temperature, the inner temperature difference is small.

(3) Installation space and mounting: Targeted sites should have enough space for installing. For example, heat exchangers, rods have very limited space for installing a whole package; the pumps, generators always have excessive vibration which makes mounting process more difficult.

(4) Necessity for monitoring: systems should be deployed to places needed to be monitored. For example, although outside loop has enough vibration and fluid kinetic energy, it's far away from reactor so that radiation is weak and water temperature and pressure are not vital.

Based on above criteria, the ideal installation sites are the primary loop and secondary loop (PWR), where the waste energy is tremendous and harvestable, and the monitoring is necessary. Besides, the relative large space and simple geometry bring convenience to the installation and maintenance.

3.2 Design Guide—Requirement survey

In this stage, only thermal energy harvesting is considered. Thus, the power generation requirement of TEG is determined by the power consumption of all the electronics. The total amount of generated power should be, at least, larger than the power consumption, so that extra power can be stored in a battery during charging cycle and supply electronics continuously in the off cycle.

For this application, there are two main circuits need to be powered, energy management and wireless communication circuits, which consist of five main electronics, i.e. DC/DC converters, microcontroller, wireless transmitter, Langasite sensors, sensor conditioning circuits. An investigation of the energy consumption of each elements was done and the results are shown followed.

Table 3-4 Estimated power requirement of each electronic component

	Estimated Power Requirement	
Component	Sleep Mode (W)	Normal-Operation Mode (W)
DC/DC Converter	<0.01	0.01-0.10
Microcontroller	<0.01	0.05-0.15
Wireless Transceiver	<0.10	0.10-0.50
Conditioning Chip	<0.01	0.01-0.10
Other Electronics	<0.01	0.01-0.15
Total	<0.14	0.18-1.00

3.3 System level design

The system level integrated design includes the design of thermoelectric energy harvester, energy management circuit, wireless communication device, sensors package and signal conditioning microprocessor. The harvested energy will primarily be used to power electronics after regulating the output voltage, and the surplus of which will be stored in a battery. In off power mode, battery will serve as the energy source to power the electronics.

A diagram of integrated design is shown in the following figure.

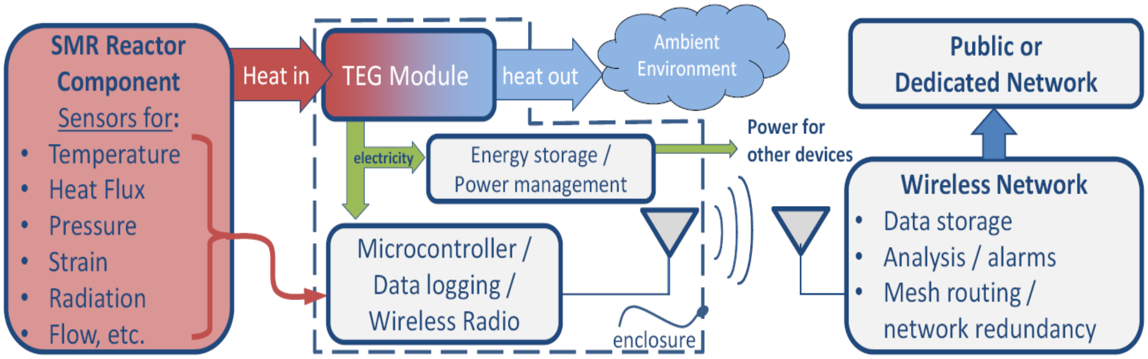

Figure 3-3 System level design diagram

The sensor package is developed by another partner team. A langasite sensor is similar to a piezoelectric resonator, whose frequency is sensitive to both pressure and temperature. Analyzing the frequency, one can measure the instant temperature and pressure simultaneously.

3.4 Introduction to Electrical part

The electronic Part consists of following two sub-systems: power system, sensor and wireless communication system. The langasite sensor is not involved in current phase since it is still under developing. Therefore, thermal couples and pressure transducer are used to collect and input data.

In order to store the energy produced by the thermal energy harvester, a 4.1V Li-ion Battery, which powers most of the sensors and the wireless communication system, is used in the project. In most cases, the voltage output of the thermal energy harvester is lower than 4.1V, thus a step-up converter is needed to charge the battery. SEPIC converter chip LT1513 from Linear Technology Co. is applied to build the step-up charger. It starts to charge the Li-ion Battery when the thermal energy harvester output voltage reaches 2.4V. Meanwhile, LM2700 step-up converter is also used in the second stage to boost the battery voltage to 12V to power the pressure sensors. The diagram of electrical part design with different elements as well as the energy & data flow is displayed in Figure 3-4.

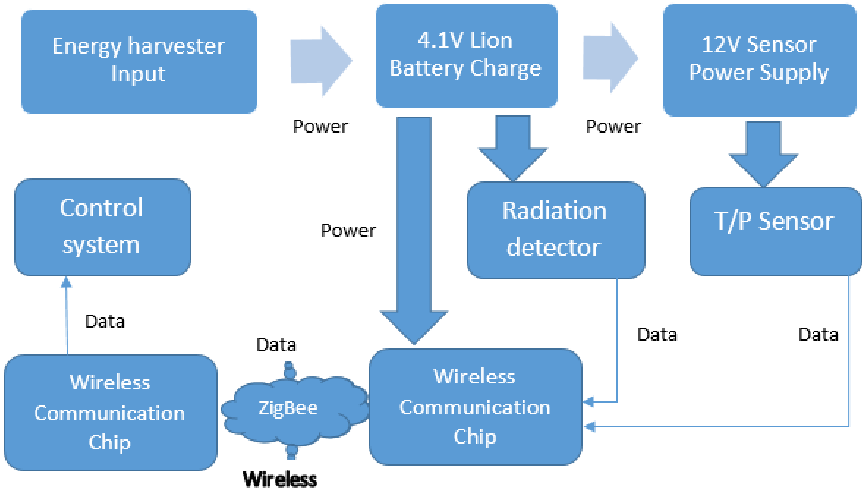

Figure 3-4 Schematic diagram of electrical part

The wireless communication is achieved by the CC2530 wireless microcontroller through the Zigbee protocol. It transfers the information over a range of several hundred meters, which is suitable for the application of this project. The wireless chips and most of the sensors can be directly powered by the Li-ion battery since the supply voltage range of them fits in the range of 3.3-5V, while the pressure sensor is a special case which requires a 12V supply and can be powered with the help of the LM2700 step-up converter. The data that sensors gathered will be sent to the wireless chip and transmitted to a computer for display. The images of energy management circuit (converter and charger) and wireless communication circuits are shown in Figure 3-5.

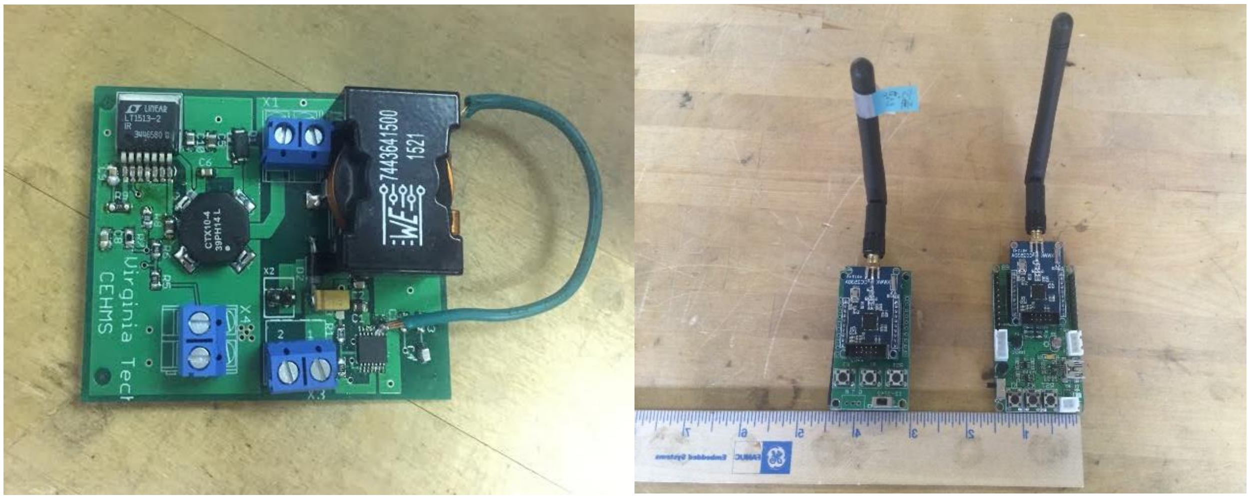

(a) (b)

Figure 3-5 Images of electrical part circuits: (a) integrated energy management circuit; (b) wireless communication chips with transmitter (left) and receiver (right).

3.5 Detailed design for harvester

3.5.1 Thermoelectric module selection

Considering the temperature range of the targeted sites and the power generation requirement, commercial Bi_2Te_3 modules that are available in the market have already been capable for this application. This eliminates the need to design and fabricate a module by ourselves, and makes this work more repeatable and less cost.

To ensure the system works reliably and effectively, two criteria were set in the selection of commercial TEM products: 1) be able to power the electronics in the off-power mode; 2) use as less TEMs as possible. Three commercially available TEGs are selected from three suppliers as potential TEM, whose detailed properties are summarized in the following table.

Table 3-5 Specifications of potential thermoelectric modules for this applications.

	Hz-2 Hi-z Technology	TG12-2.5-01LS Marlow	TEG1-1263-4.3 TECTEG
Size (mm)	29×29×5.08	29.97×34.04×4.04	30×30×
Thermal resistance (℃/W)	~2.48	3.7	Not specified
Open circuit Voltage (V) /Temperature difference (℃)	6.53/200	9.63/180	10.7/270
Match load Power (W) /Temperature difference (℃)	2.5/200	2.4/180	5.2/270
Maximum working temperature	400 ℃	230 ℃	300 ℃

In fact, all these listing thermoelectric modules have similar performance in their working range, and meet the requirement for power consumption. Since temperature at targeted site might reach above 300 ℃, although this does not necessarily means the hot side temperature of module will be above 300 ℃, a high-temperature sustainable module would be favored for its higher reliability. Besides, the module should have larger thermal resistance so that a larger temperature difference can be achieved across both sides when applying to the overall harvester system. For these reasons, the Hz- 2 modules from Hi-z Technology are selected in this design. The picture of Hz-2 module can be found in figure 2-3.

3.5.2 Heat sink design

An ideal heat sink for this design should be able to dissipate the absorbed energy efficiently with low thermal resistance and small size. Forced convection heat sinks are first considered. However, the extra energy cost for the external fan can hardly lead to a considerable augment in power generation (This extra fan could be viewed as an effective method to reduce heat sink thermal resistance. However, the TEM in this applications are designed to have larger thermal resistance, thus the reduction in overall thermal resistance is only moderate). Therefore, only natural convection heat sink are considered in this design. The detailed modeling of heat sink equivalent thermal resistance will be introduced in next chapter, but the efficiency in terms of geometry will be discussed here.

For a given vertical heat sink, fin geometry can be illustrated in the following Figure 3-6. When fin height and length are selected, an optimum space between fins can be thus determined as [72]:

$$S_{opt} = 2.714 \frac{L}{{Ra_y}^{0.25}} \tag{3}$$

$$Ra_y = \frac{g\beta(T_s - T_\infty)y^3 Pr}{\nu^2} \tag{4}$$

where Ra_y is Rayleigh number, L is fin length; T_{sink} is the average temperature at heat sink fin surface; y is the heat sink length. In a very first stage of design, the heat sink surface average temperature is targeted at less than 60 ℃, so that the major temperature is on the TEM and the size of heat sink is reasonably small. Once the overall size of heat sink is determined, the optimum fin geometry can be thus determined, so that a commercial heat sink can be thus selected from market.

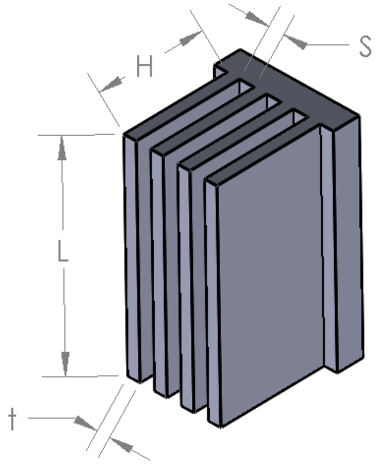

Figure 3-6 Fin geometry of heat sink

To further reduce the size of heat sink and thus the overall device size, a parallel thermal circuit is proposed, in which two heat sinks are employed in a symmetric design using two TEMs. Thus, the heat need to be dissipated is divided for each of heat sink without introducing more complexity in system design.

Besides the criteria made for the heat sink selection above, the heat sink should also be able to fix with other parts conveniently. Thus a heat sink with partial removal of extrusion was finally selected, as shown in Figure 3-7. Each single heat sink has a size of 125mm (width) ×150mm(length) ×49mm(height), a fin height of 41mm, and an average fin space of 5.5mm.

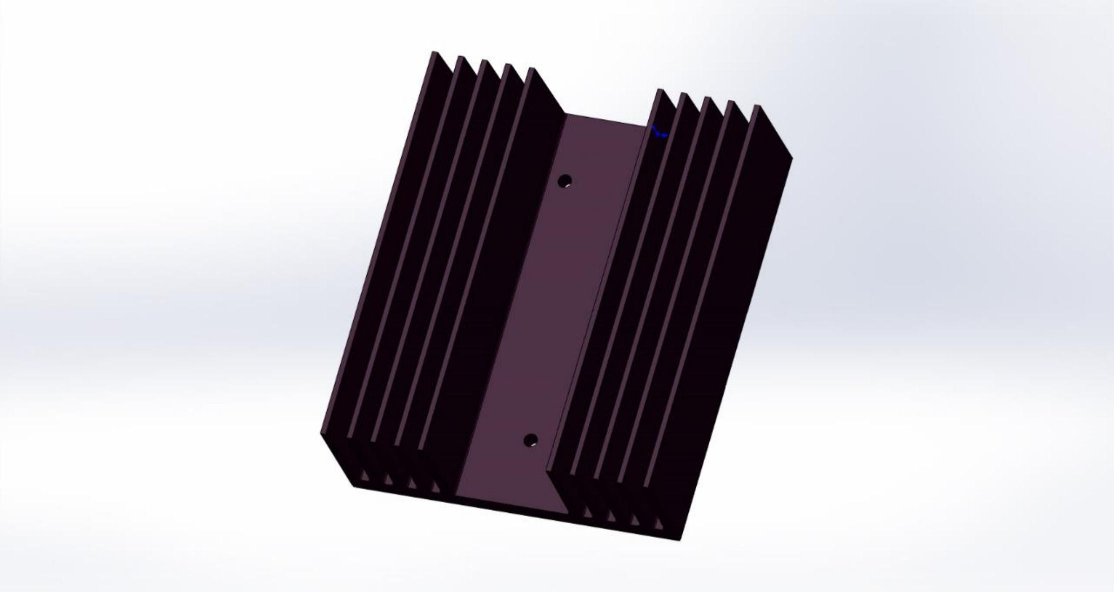

Figure 3-7 Final design of heat sink

3.5.3 Heat pipe design

Heat pipe is a state of art heat transfer device that have hundreds times higher efficiency than normal metal in heat transfer process. Considering the generator will be assembled onto the coolant loops where pipe insulation layer can be thick, an advanced heat transfer tool is to be employed to conduct heat from the pipe to the ambient air. Therefore, a gravity assisted heat pipe is proposed in the integrated design. Detailed description and modeling can be found in next chapter.

To select an effective heat pipe for this application, a suggested process is stated as follow:

1). Investigate several operational parameters: heat load, temperature profile of heat source, operation mode.

2). Select the pipe material, wick structure, and working fluid.

- Determine appropriate working fluid

- Select compatible wall material
- Determine wick structure
- Decide protective coating

3). Finalize detail pipe geometrical parameters.

4). Calculate the operation limits of heat pipe to make sure it works for this application.

For this application, to ensure the system can harvest more than 1 W of energy, 50~150W of heat should be extracted from the steam pipe (considering the efficiency of TEM in different temperature range is typically 1~2%). The temperature at evaporating end is the steam temperature. Besides, the system is installed vertically so that gravity could be used to enhance heat transfer in the heat pipe.

When determining the working fluid, temperature and heat transfer capability are the key parameters to be considered. The heat transfer capability can be described by liquid transport factor, which is defined as

$$M = \frac{\rho_L \sigma \lambda}{\mu_L} \tag{5}$$

where ρ_L, μ_L are the density and viscosity of liquid, respectively; σ is the surface tension ; and λ is latent heat. The liquid transport factor of various heat pipe working fluids in terms of temperature are summarized in the following figure.

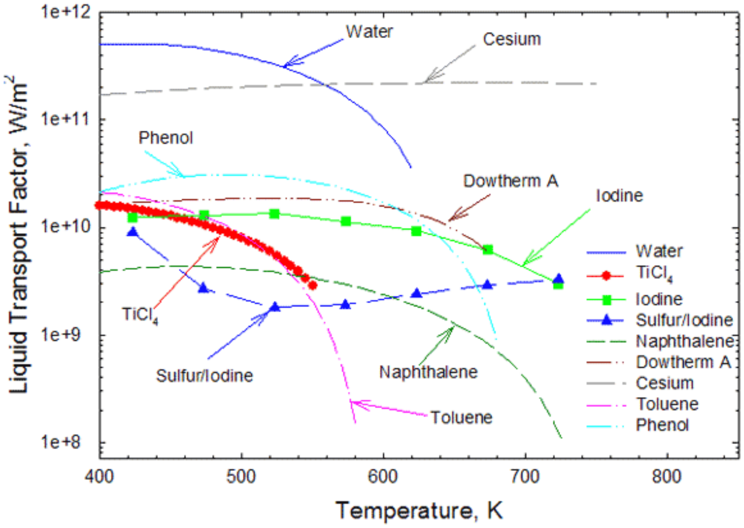

Figure 3-8 Liquid transport factors of various potential working fluids

Water is selected as the working fluid, since it remains the most efficient working fluid in targeted temperature range. Then, the wall material that compatible for water that can be selected are copper and nickel [73]. Copper-nickel alloy is selected as wall material for its low cost with readily availability and good resistance to corrosion in high temperature range.

The demanding heat pipe geometry and amount in different working conditions are summarized in the Table 6. The finalized diameter and length of heat pipe are designed to be 19.05mm (3/4 inch) and 200mm, respectively, which should be thick enough to transport enough heat and long enough to penetrate the insulation layer. Only one heat pipe is used so that the design in geometry makes the system mechanically more stable and the assembly easier.

Table 3-6 Heat pipe demanding in different temperature and power input (200mm length, and 40mm evaporator and condenser length assumed)

Input power (W)	Evaporator temperature (℃)	Minimum Heat pipe diameter (mm)	Numbers of heat pipes needed
50	100	6.35 (1/4”)	1
50	200	6	1
100	100	15.88 (5/8”)	1
100	200	12.7	1
100	250	19.05	1
150	200	19.05	1
150	250	19.05	2

Figure 3-9 shows the picture of the ordered heat pipe. This customized product is a copper-water heat pipe provided by Noren Products Incorporated. In this design, the length of evaporator, condenser and adiabatic sections are 50mm, 60mm and 90mm, respectively. This heat pipe was cut from a longer heat pipe and soldered with a cap at the cut surface. Phosphor is selected as the wick material; while methanol is filled as additional working fluid.

Figure 3-9 Final selection of heat pipe

3.5.4 Integrated design of thermal part

The first generation of design for this application is developed in Stony Brook University by Tewolde *et. al* [45]. By using 4 TEMs (Hi-z 2), they successfully generated a power output of 1.0W, with an overall size of 12” by 12”. However, this design can be improved by the following manners: 1) Reducing overall size of generator design; 2) Increasing efficiency of TEM. The detailed design is shown if Figure 3-10.

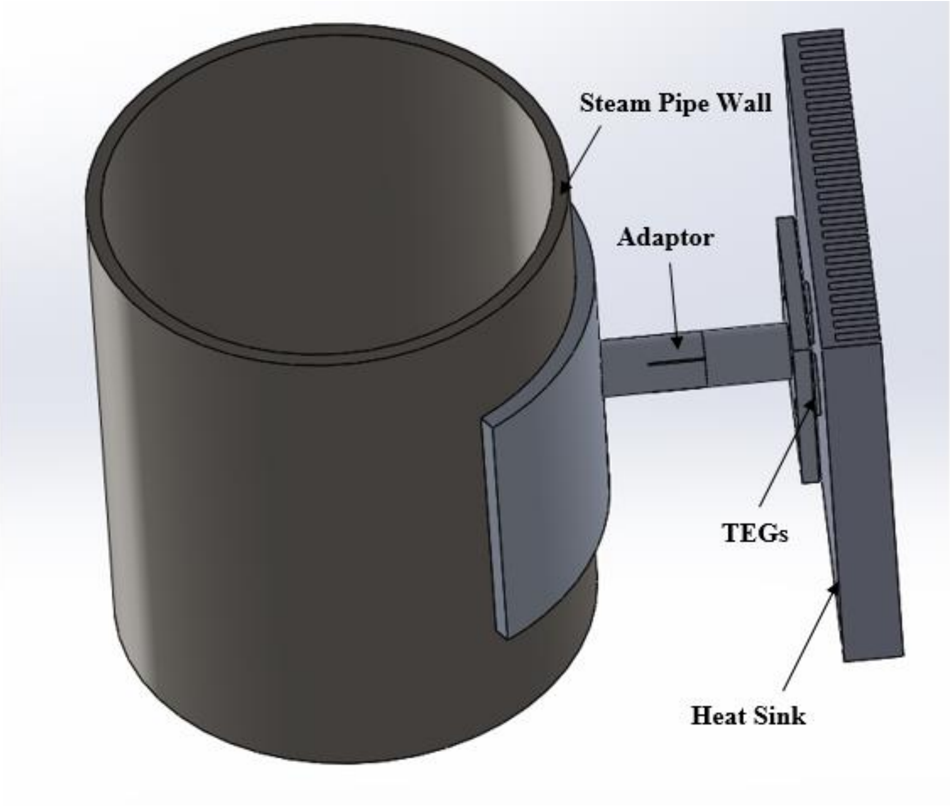

Figure 3-10 First generation prototype

As stated in the 4.2 section, in this design, a parallel thermal circuit was proposed to reduce the necessary large surface on the cold side heat sink for heat dissipation. This design effectively reduces the size of heat sink, and therefore reduces the size of overall device. Besides, building a symmetrical geometry helps to improve the system stability considering there might be severe vibration in pipelines.

A metal block made of 9091 aluminum is designed to serve as heat distributor that divides the heat flow into two directions with identical amount. This block is connected with heat pipe through a blend hole in the center of the block, and connected with TEMs through thermal grease. Shallow rectangular indents with 1mm depth are machined on the surfaces contacting with modules serving as guides for the TE modules. The width of each guiding indent is 30mm so that the module can be “inserted” into the block to make sure the two TEMs are placed symmetrically at both sides of the aluminum hot block. A deep grove is cut along the height direction, makes this block a U-shaped “clamp” structure.

The two heat sinks are connected through three bolts with 10-24 pitch, the TEMs and aluminum block are sandwiched between the two heat sinks. A similar shallow grove is also machined on the heat sink base surface to mount the TEM. By applying the same torque on the bolts, the U shape block will have slight deformation so that the heat pipe and TEMs are clamped. Flanges or saddles will be needed when installing the whole device onto the steam pipes.

The picture of U shape aluminum block and the integrated design are summarized in the following Figure 3-11.

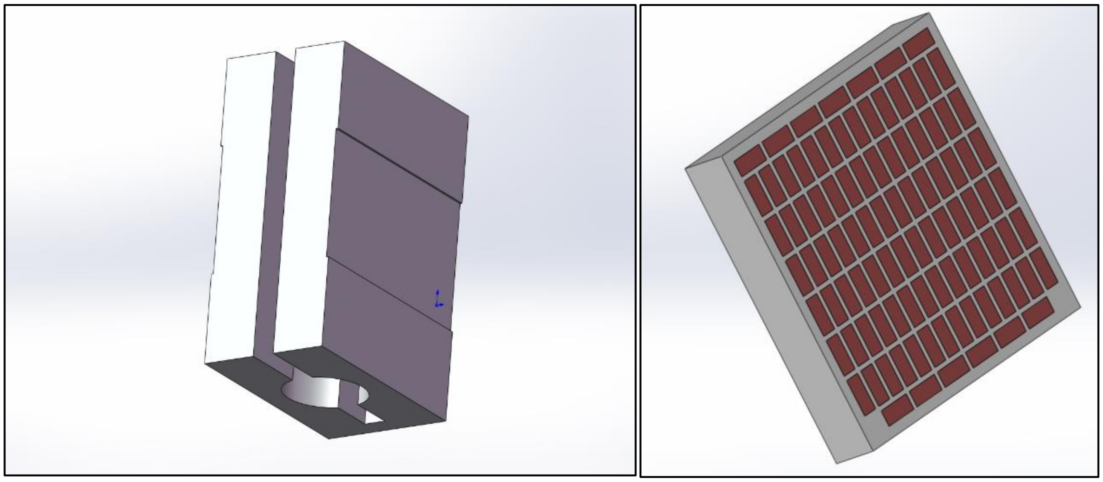

(a) (b)

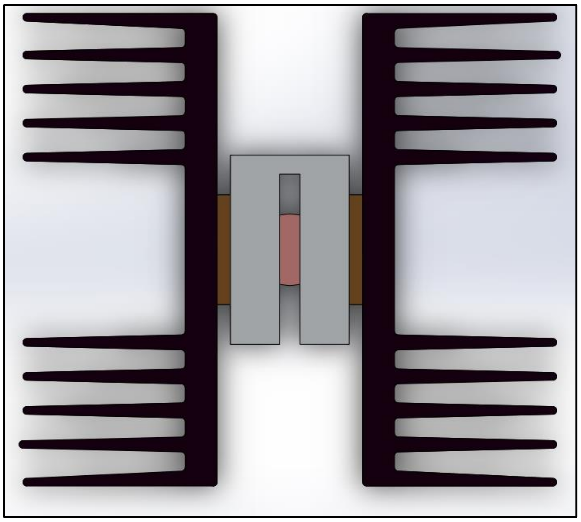

(c)

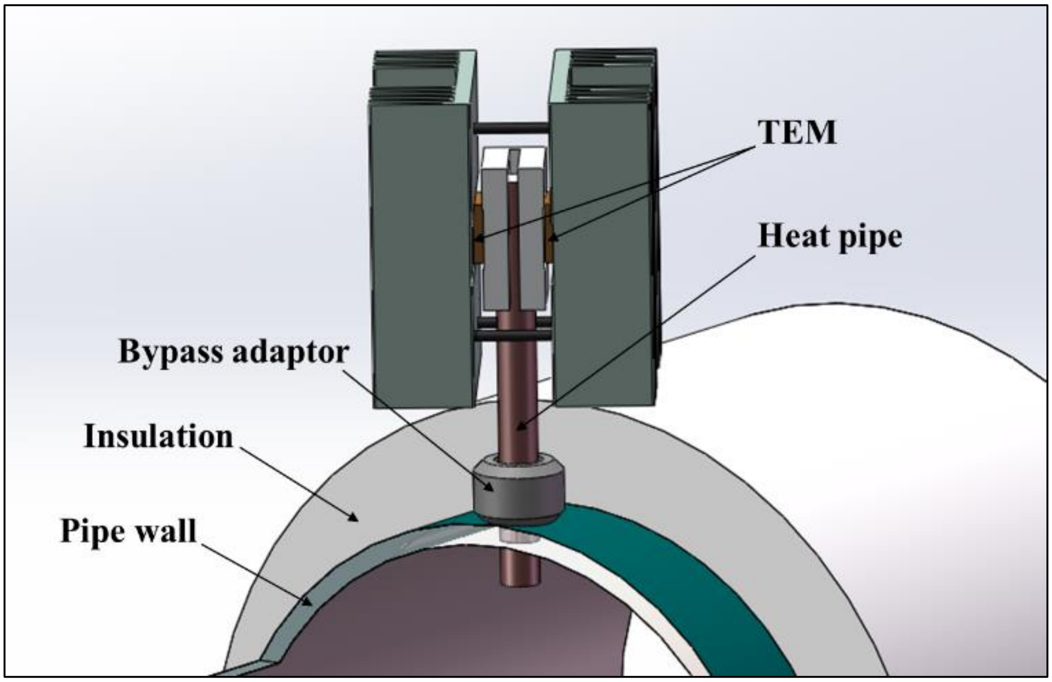

(d)

Figure 3-11 Design of the U shape aluminum block (a); CAD drawing of the module (b); top view of thermoelectric harvester assembly (c); the assembly of the whole system on a coolant pipe (d)

4 Analytical modeling

4.1 1-D Heat transfer circuit

Considering the generator system is primarily targeted on harvesting energy from coolant loops in nuclear power plants, where the source temperature can be treated as constant, the modeling of the heat transfer process was performed in steady state. Now, it is convenient to calculate the thermal resistance of different elements in steady state.

As is shown in Figure 4-1, the thermal circuit basically consists of six sectors: heat source, heat pipe, hot side block, TEG modules, heat sinks and contact resistance at each interface. In steady state, the heat transfer modeling can be reduced to a simple way: by calculating the equivalent thermal resistance of each element in the heat flow path, and aggregating them in a way similar to calculate the overall electrical resistance in electric circuits.

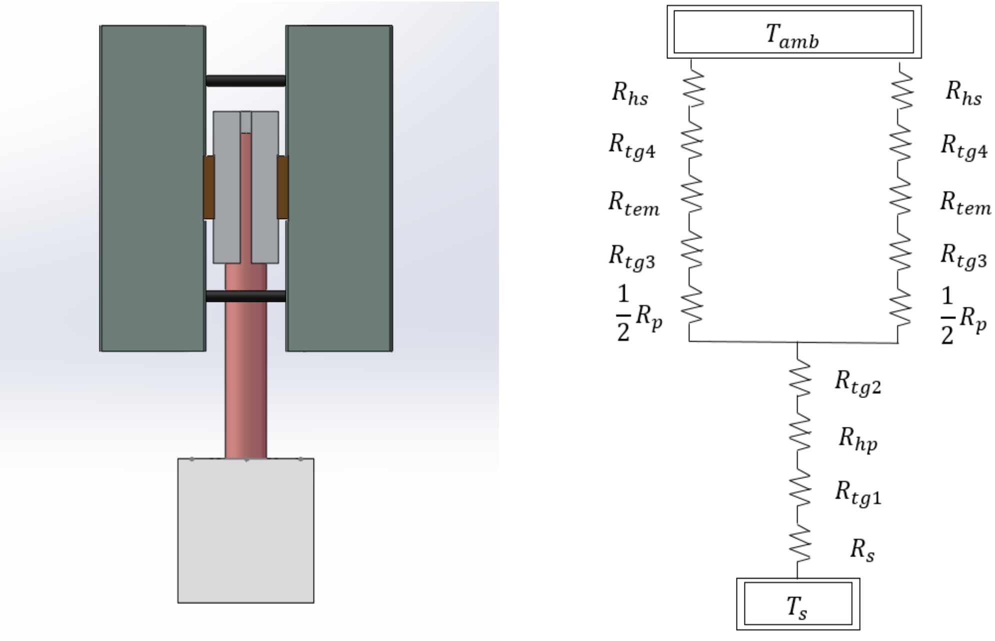

Figure 4-1 CAD design of the experimental system (left); Schematic diagram of heat transfer circuit of the overall design (right): Rs: resistance at source. Rhp: heat pipe resistance. Rp: U shape plate thermal resistance. Rtem: TEM resistance. Rhs: Heat sink resistance. Rtg: contact resistance with thermal grease.

The thermal resistance of a solid can be denoted as

$$R = \frac{\Delta T}{q} \tag{6}$$

This equation can be applied to calculate thermal resistance of all the elements in this diagram.

4.2 Heat pipe thermal resistance

The modeling of heat transfer process in a heat pipe can be difficult. However, in this application, the heat pipe works at steady state so that applying the steady state assumption avoids the discussion of heat transfer in transient state and operation limits.

Following assumptions have been made underlies this modeling:

1) The startup process of heat pipe is not considered.

2) The pressure drop in the heat pipe is enough to make sure the liquid can flow back to evaporator so that dry out will not happen.

3) Heat pipe worked at nucleate boiling regime, and heat transfer from wick to working fluid only through boiling; heat and mass transfer in the vapor liquid interface is in steady.

4) Wick structure is homogeneous and form a layer that is fully saturated with working fluid, water, so that only conduction is considered in wick.

5) The convection and radiation at the outer surface of heat pipe is not considered.

The overall thermal resistance of a heat pipe should be as low as possible so that heat can be transferred from evaporator to condenser with lowest energy cost. By calculating the equivalent thermal resistance at each section along the heat transfer path, the overall thermal resistance of a heat pipe can be therefore obtained. The thermal resistances inside a heat pipe included in this modeling are shown in Figure 4-2.

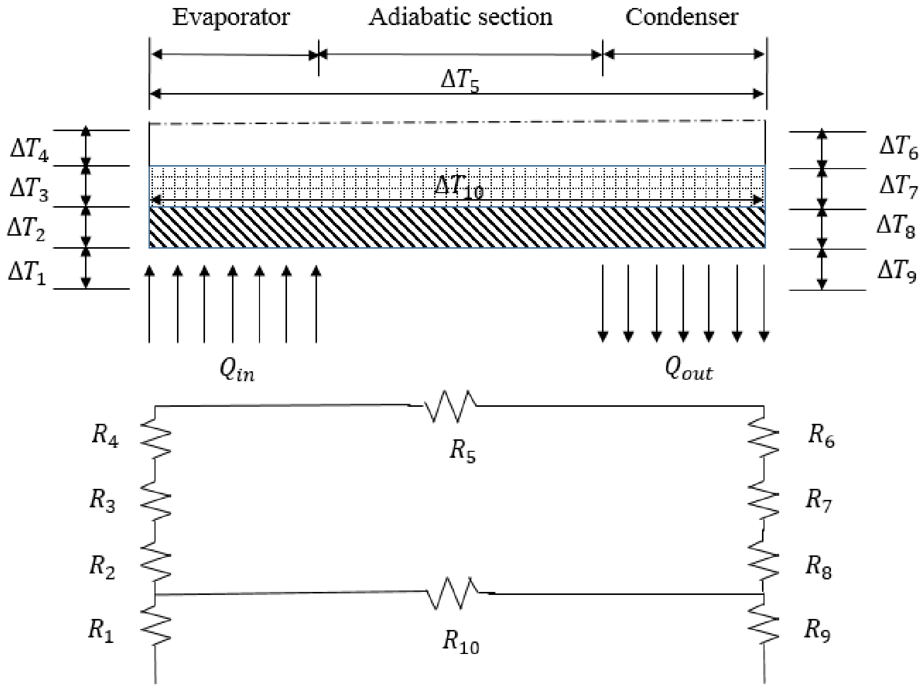

Figure 4-2 Schematic diagram of heat transfer circuit a typical heat pipe

The effective length of a heat pipe instead of geometrical length is considered since mass flow will vary in both the evaporator and the condenser region [74].

$$l_{eff} = \frac{l_e + l_c}{2} + l_a \tag{7}$$

Along the heat transfer path, there are mainly 9 thermal resistances that should to be considered:

1) Heat was transferred to the heat pipe through convection with the steam at the outer surface of evaporator side, the equivalent thermal resistance will be

$$R_1 = \frac{1}{h_{ex} A_{ex}} \tag{8}$$

where h_{ex} is the convective heat transfer coefficient, which can be found by calculating the average Nusselt number. The Nusselt number of a cross flow pass a perpendicular cylinder can be found as [36].

$$Nu_D = 0.3 + \frac{0.62 Re_D^{\frac{1}{2}} Pr^{\frac{1}{3}}}{\left[1 + \left(\frac{0.4}{Pr}\right)^{\frac{2}{3}}\right]^{\frac{1}{4}}} \left[1 + \left(\frac{Re_D}{282000}\right)^{\frac{5}{8}}\right]^{\frac{4}{5}} \tag{9}$$

where Re_D is the Reynolds number. Then, h_{ex} can be found since

$$h_{ex} = \frac{Nu_D k_s}{D} \tag{10}$$

2) The heat absorbed at the outer surface will be conducted both radially and axially in the outer copper shell, and then will be conducted to the wick structure in radial direction. Heat transfer in the wick structure can be very difficult since the fluid flow in the wick structure is complex. However, the assumption could be made that working fluid is saturated in the wick structure so that the problem will be massively simplified into heat conduction without significant loss in accuracy. The conductive thermal resistance in both radial and axial directions can be calculated as

$$R_r = \frac{ln\left(\frac{r_o}{r_i}\right)}{2\pi k L} \tag{11}$$

$$R_a = \frac{L}{k\pi(r_o^2 - r_i^2)} \tag{12}$$

The thermal conductivity k of wick structure in both series and parallel is determined through

$$k_{wl} = (1-\varepsilon)k_w + \varepsilon k_l \tag{13}$$

$$k_{wl} = \frac{1}{\frac{1-\varepsilon}{k_w} + \frac{\varepsilon}{k_l}} \tag{14}$$

where ε is the porosity of wick structure. The above calculation also validates for conductive thermal resistance in wick and pipe wall at condensing side.

3) As heat is conducted to the interface of wick layer and working fluid layer at evaporator, nucleate boiling occurs so that heat can be transmitted to the working fluid with a small temperature difference and therefore a small thermal resistance. Rohsenow made a correlation

(equation 15 and equation 16) between heat transfer and fluid property following the method similar to forced convective heat transfer correlation [75]:

$$Nu = \frac{1}{C_{sf}} Re^{1-x} Pr^{-y} \tag{15}$$

$$\frac{c_{pf}\Delta T_{sat}}{L} = C_{sf}\left[\frac{\dot{q}}{\mu_l L}\left(\frac{\sigma_l}{g(\rho_l - \rho_v)}\right)^{0.5}\right]^{x}\left[\frac{\mu_l c_{pl}}{k_l}\right]^{1+y} \tag{16}$$

For water-copper interface, constant C_{sf} is 0.013, and the variable x and y here are 0.33 and 0.7, respectively [76]. Here, $\dot{q}$ is the heat flux per unit area, which needs to be estimate before calculation and then iterate till it converged with the result corresponding on overall heat flow q. The heat flow through dry surface is neglected since the dry surface area here in the evaporator section is small in this application. The equivalent thermal resistance will be

$$R_4 = \frac{(2\pi RT)^{0.5} RT^2 \Delta T_4}{A_4} \tag{17}$$

At condenser side, we only consider film condensation, so this correlation also validate at the condenser side of vapor fluid interface.

4) After the heat is transferred to the working fluid, there is a mass flow at the vapor liquid interface. This leads a small thermal resistance existing at evaporating surface. The equivalent thermal resistance can be found based on Clapeyron equation as:

$$R_5 = \frac{RT\Delta P_v}{\dot{q} L P_v} \tag{18}$$

In laminar flow, combined with equation 18, the pressure change in the above equation can be calculated as [74]:

$$\Delta P_v = \frac{8\mu_v \dot{m} l_{eff}}{\rho \pi r_v^4} \tag{19}$$

5) At outer surface of condenser side, heat conducted to next aluminum block through conduction.

After deriving the thermal resistance at each elements, the total thermal resistance in a heat pipe can be thus aggregated as

$$R_{hp} = R_1 + R_9 + \left(\frac{1}{R_{10}} + \frac{1}{\sum_{i=2}^{8} R_i}\right) \tag{20}$$

4.3 Heat sink thermal resistance

In this application, two heat sinks are attached at both cold sides of the thermoelectric modules. To ensure the TEM cold side temperature is as low as possible, the thermal resistance of the heat sink should be as low as possible, so that temperature gradient across the module can be maximized.

Thermal resistance of heat sink is composed of three parts: spreading resistance at base plate, conductional resistance at base plate, convectional and conductional resistance at the fins [77]. The conductive resistance at base side can be easily deducted from Equation 21 as

$$R_b = \frac{t_b}{k_b A_b} = \frac{t_b}{k_b (W_b L_b)} \tag{21}$$

The spreading resistance is due to the change of surface area from small to larger along the heat flow path. The determination of spreading resistance is introduced by Yovanovich as [78]:

$$R_{sp} = \frac{1 - 1.410\epsilon + 0.344\epsilon^3 + 0.043\epsilon^5 + 0.034\epsilon^7}{4k_b\sqrt{A_{tem}}} \tag{22}$$

where ϵ is the ratio of surface area between the smaller one to bigger one, which are TEM surface area and aluminum heat sink base plate area, respectively.

The thermal resistance at the fins including conductive and convective and radiative resistances inside cooling channels, among which natural convection impacts more when fins are sparse and radiation impacts more when the fins are condensed. For this heat sink, an overall thermal resistance at fins can be denoted as [77]:

$$R_{fa} = \frac{1}{(h_c + h_r)(A_p + \eta_f A_f)} \tag{23}$$

Here, h_f is the convective heat transfer coefficient; h_r is the equivalent radiation coefficient. The fin efficiency, η_f, of rectangular shape fin can be determined as.

$$\eta_f = \frac{q_b}{q_{max}} = \frac{\tanh(mH_f)}{mH_f} \tag{24}$$

$$m = \sqrt{\frac{h_c P_f}{k_b A_c}} = \sqrt{\frac{2h_c}{k_b t_f}} \tag{25}$$

The terms A_p and A_f are primary plate area and fin area, respectively. Then the effective area is

$$A_{eff} = A_p + \eta_f A_f = (N-2)W_b L + W_a L + \eta_f \left(2NW_b H_f\right) \tag{26}$$

Since the heat sink will be exposed to ambient air, and there is only natural convection. The convectional heat transfer coefficient of rectangular fin can be calculated as [79]

$$h_f = \frac{Nu_{\sqrt{S}} k_{amb}}{\sqrt{S}} \tag{27}$$

where $Nu_{\sqrt{S}}$ is the Nusselt number with $\sqrt{S}$ as a characteristic length.

$$Nu_{\sqrt{S}} = Nu_{\sqrt{S}}^{\infty} + f(Pr) G_{\sqrt{S}} Ra_{\sqrt{S}}^{0.25} \tag{28}$$

$$Ra_{\sqrt{S}} = Gr \cdot Pr = \frac{g\beta(T_{sink} - T_{amb})\sqrt{S}^3}{v^2} \tag{29}$$

To calculate the thermal resistance at the fin side, an iteration will be needed since the heat sink surface temperature is an unknown at the very beginning. For a given heat flow, an initial estimation for T_{sink} is given; then a convective heat transfer coefficient can be calculate, so that an intermediate fin side resistance can be acquired. After that the surface temperature T_{sink1}can be calculated by the following equation

$$T_{sink1} = q_{hs} \times R_{fa} + T_{amb} \tag{30}$$

where q is the given heat flow. Compare the T_{sink1} and T_{sink} and run this iteration until they converge with an acceptable error, the actual value of R_{fa} can be achieved finally.

The radiation effect in the fin area has less impact on the resistance than the convection, and can be found elsewhere [77].Detailed modeling of heat transfer in a U channel can be found in [80]. The overall heat sink thermal resistance in steady state is thus

$$R_{hs} = R_b + R_{sp} + R_{fa} \tag{31}$$

4.4 Thermoelectric module coupled processes

The physics during the operation of a pair of p-type and n-type thermoelectric legs consists of five parts: heat conduction, Joule heating, Seebeck effect, Peltier cooling/heating and Thompson effect [81]. Among these processes, Seebeck effect corresponds to the energy conversion from heat to electricity, in which a temperature gradient between two ends of thermoelectric material will induce a voltage difference. Based on this phenomenon, commercial thermoelectric modules have been developed, which typically consist of multiple P/N junctions connected thermally in parallel and electrically in series, electrical conductors, ceramic insulator and substrates. Equation 33 explains the working principle of a thermoelectric module containing n pairs:

$$\alpha = \alpha_P - \alpha_N \tag{32}$$

$$V = n\alpha(T_h - T_c) \tag{33}$$

where α_P and α_N represent the seebeck coefficients of both positive and negative legs, and $(T_h - T_c)$ is the temperature difference. The seebeck coefficient is a natural temperature-dependent property of material, whose value varies from positive to negative depending on material polarity. In a low temperature application, the temperature gradient across the TEG is relatively small so that the Thompson effect can be neglected [82].

To harvest energy, an external load R_L is needed so that the generated power will be dissipated on this resistive load. According to Ohm's law, the electrical current flows in the external resister will be

$$I = \frac{n(\alpha_P - \alpha_N)\Delta T}{R_i + R_L} \tag{34}$$

where R_i is the internal electrical resistance of the module which can be found through material electrical conductivity and leg geometry. Thus, the energy generated by the TEG can be denoted as

$$P = I^2 R_L = \frac{n^2(\alpha_P - \alpha_N)^2(\Delta T)^2 R_L}{(R_i + R_L)^2} \tag{35}$$

Then, the efficiency of thermoelectric module can be calculated as

$$\eta = \frac{P}{nq_h} = \frac{I^2 R_L}{n\alpha I T_h + \mathrm{n}K(T_h - T_c) - \frac{1}{2} n I^2 R_L} \tag{36}$$

The diagram of energy harvesting and heat transfer processes in a commercial TEG is shown in figure 4-3.

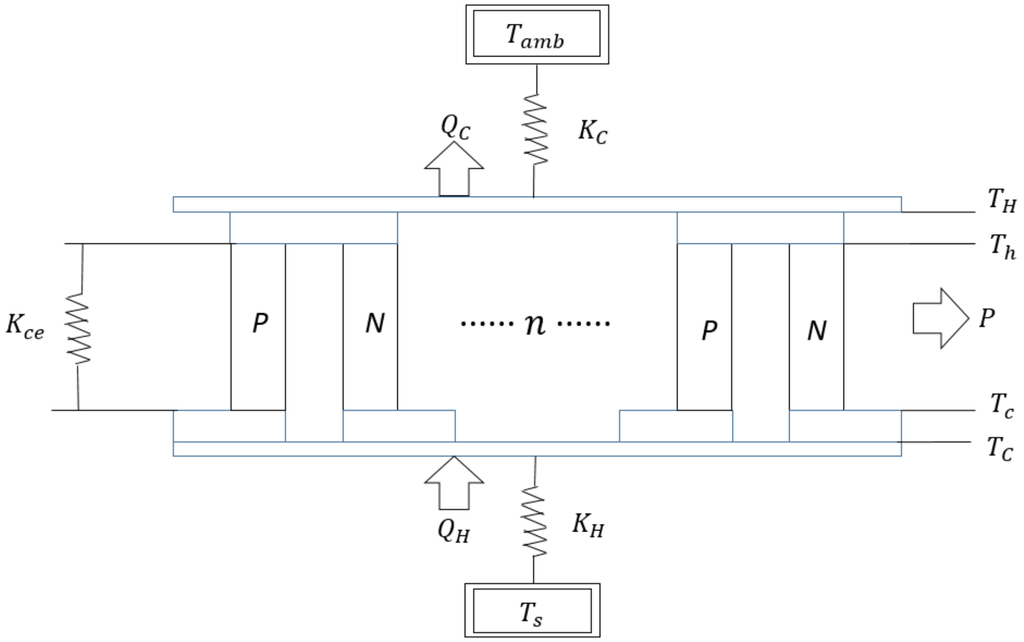

Figure 4-3 Schematic diagram of heat transfer and energy conversion in a typical thermoelectric module.

In steady state, thermal resistance of each part of TEGs can be deducted by the Newton's Law separately. As shown in Figure 4-3, the overall thermal resistance of a TEG is composed of resistances in five layers: electrical insulator layers at top and bottom sides, aluminum connector layers at top and bottom sides and the functional layer. Note that the temperature difference between both sides of TEG is not exactly same as the difference between both ends of legs. By modeling resistances in the five-layer-structure using a typical commercial product Hz-2 (from Hz Technology Corporation), thermal conductance at each layer is compared in the following table. The thermal resistance of sealing materials, typically ceramic and polymers used to protect thermoelectric legs, is usually overlooked but is considered in this modeling.

Table 4-1 Detailed results of thermal resistance simulation (based on Hi-z 2)

Layer	Resistance Equation (37~41)	Value (W//K)	percentage
Insulation layers	$R_{in} = 2t_{in}/(k_{in}A_{teg})$	0.0476	1.9%
Top connector layer	$1/R_{top} = 1/R_{ce,t} + 1/nR_{al}$	0.0098	0.4%
Bottom connector layer	$1/R_{bot} = 1/R_{ce,b} + 1/[(n-1)R_{al}]$	0.0099	0.4%
Functional layer	$\frac{1}{R_{fun}} = \frac{1}{R_{ce,f}} + \frac{1}{nR_P} + \frac{1}{nR_N}$	2.4158	97.3%
Overall resistance	$R_{tem} = R_{in} + R_{top} + R_{bot} + R_{fun}$	2.4832	

To analysis energy generation and heat transfer processes in the TEG, a condensed model is used as shown in the Figure 4-3. The thermal conductance at the hot side, K_H, is the summed conductance of all elements in the heat flow path from the source to the hot side of module, as stated in Equation 42; the conductance at cold side, K_C, is the summed conductance of heat sink and thermal grease, as shown in Equation 43.

$$\frac{1}{K_H} = R_s + R_{tg1} + R_{hp} + R_{tg2} + \frac{1}{2}\left(\frac{1}{2}R_p + R_{tg3}\right) \tag{42}$$

$$\frac{1}{K_C} = \frac{1}{2}\left(R_{hs} + R_{tg4}\right) \tag{43}$$

Inside the thermoelectric module, the thermal conductance is composed of K_{PN} and K_{ce}, which are thermal conductance of pairs and insulating ceramic. The summed thermal conductance of one pair of legs and the conductance of insulating material are expressed as

$$K_{PN} = \frac{k_P \cdot L_P}{A_p} + \frac{k_N \cdot L_N}{A_N} \tag{44}$$

$$K_{ce} = \frac{k_{ce}\left(A_{teg} - nA_P - nA_N\right)}{L_{ce}} \tag{45}$$

where k_P, k_N and k_{ce} are the thermal conductivity of P-type, N-type legs and insulating material, respectively. L_P and L_N are the leg heights and there is $L_P = L_N = L_{ce}$; A_N and A_p are the cross section area, and $A_N = A_p$. Given the results listed in table 1, the thermal resistance of the connecting layers are negligible, therefore, the temperature difference at these layers are negligible. Then, it is reasonable to assume the temperature difference at two ends of legs is equivalent to the difference between hot side and cold side.

The internal electrical resistance of a TEG mainly comes from the semi-conductive thermoelectric legs in series.

$$R_i = n\left[\frac{\rho_P \cdot L_P}{A_p} + \frac{\rho_N \cdot L_N}{A_N}\right] \tag{46}$$

In this modeling, Joule heating is considered as an internal heat generation process, where the generated heat is conducted to the hot side and cold side equivalently. Combining the Peltier effect and the heat conduction, the rates of incoming heat and removal heat at the hot and cold junction of a single pair can be calculated as

$$q_h = \bar{\alpha} I T_h - \bar{K}_{PN}(T_h - T_c) + \frac{1}{2} I^2 \bar{R}_{PN} \tag{47}$$

$$q_c = \bar{\alpha} I T_c - \bar{K}_{PN}(T_h - T_c) - \frac{1}{2} I^2 \bar{R}_{PN} \tag{48}$$

$$T_m = \frac{T_h + T_c}{2} \tag{49}$$

where, $\bar{\alpha}$ is the Seebeck coefficient at the mean temperature of both sides, $\bar{K}_{PN}$ and $\bar{R}_{PN}$ are the conductance and electrical resistance of a pair at the mean temperature, respectively. In fact, the first term on the right side of Equation 47 refers to Peltier effect; the second term refers to the heat conduction; and the third one refers to Joule heat generation.

Let $\bar{\alpha} = \alpha = \frac{\alpha_P + \alpha_N}{2}$, $\bar{K}_{PN} = K_{PN}$ and $\bar{R}_{PN} = R_{PN}$. According to the energy conservation law, the power output can be also expressed as

$$P = n(q_h - q_c) = n\alpha I(T_h - T_c) - nI^2 R_{PN} \tag{50}$$

Based on analysis above, at the top and bottom interfaces of a module, since the heat flux is continuous, the relationship between hot/cold side conductance, K_H and K_C, and the internal heat flux, q_h and q_c, can be denoted as

$$nq_h + q_{ce} = K_H(T_s - T_h) \tag{51}$$

$$nq_c + q_{ce} = K_C(T_c - T_{amb}) \tag{52}$$

$$q_{ce} = K_{ce}(T_h - T_c) \tag{53}$$

Above are the governing equations of this modules. Substitute q_h and q_c in the above equations in terms of K_H, K_C and q_{ce}, the hot side and cold side temperature can be determined in terms of known variables, T_s, T_{amb}.

$$\begin{aligned} T_h = {} & [\alpha n^2 I^3 R_{PN}/2 - (0.5nK_C + n^2 K_{PN} + nK_{ce}) I^2 R_{PN} + n\alpha I K_H T_s \\ & - (nK_{PN} + K_{ce})(K_H T_s + K_C T_{amb}) - K_H K_C T_s] \\ & \times [n^2 \alpha^2 I^2 + n\alpha(K_H - K_C) I - (nK_{PN} + K_{ce})(K_H + K_C) - K_H K_C]^{-1} \end{aligned} \tag{54}$$

$$\begin{aligned} T_c = {} & -[\alpha n^2 I^3 R_{PN}/2 + (0.5nK_H + n^2 K_{PN} + nK_{ce}) I^2 R_{PN} + n\alpha I K_C T_{amb} \\ & + (nK_{PN} + K_{ce})(K_H T_s + K_C T_{amb}) + K_H K_C T_{amb}] \\ & \times [n^2 \alpha^2 I^2 + n\alpha(K_H - K_C) I - (nK_{PN} + K_{ce})(K_H + K_C) - K_H K_C\ ]^{-1} \end{aligned} \tag{55}$$

By substituting equations 54 and 55 into equations 51 and 52, the heat flow in and out the thermoelectric module can be derived as

$$\begin{aligned} Q_h = {} & K_H(T_s - T_h) \\ & = [\alpha n^2 K_H R_{PN} I^3 - 2nK_H(n\alpha^2 T_s + nK_{PN} R_{PN} + 0.5K_C R_{PN} + K_{ce} R_{PN}) I^2 \\ & + 2n\alpha K_H K_C T_s I + 2K_H K_C (nK_{PN} + K_{ce})(T_s - T_{amb})] \\ & \times [-2n^2 \alpha^2 I^2 - 2n\alpha(K_H - K_C) I + 2(nK_{PN} + K_{ce})(K_H + K_C) \\ & + 2K_H K_C]^{-1} \end{aligned} \tag{56}$$

$$\begin{aligned} Q_c = {} & K_C(T_c - T_{amb}) \\ & = [\alpha n^2 K_C R_{PN} I^3 + 2nK_C(n\alpha^2 T_{amb} + nK_{PN} R_{PN} + 0.5K_H R_{PN} + K_{ce} R_{PN}) I^2 \\ & + 2n\alpha K_H K_C T_{amb} I + 2K_H K_C (nK_{PN} + K_{ce})(T_s - T_{amb})] \\ & \times [-2n^2 \alpha^2 I^2 - 2n\alpha(K_H - K_C) I + 2(nK_{PN} + K_{ce})(K_H + K_C) \\ & + 2K_H K_C]^{-1} \end{aligned} \tag{57}$$

Then, a function of ΔT can be achieved by plug T_h and T_c in equation 51~53.

$$C_1(\Delta T)^3 + C_2(\Delta T)^2 + C_3 \Delta T + C_4 = 0 \tag{58}$$

Where

$$C_1 = \frac{n^4\alpha^4}{(nR_{PN}+R_L)^2} - \frac{\alpha^4 n^5 R_{PN}}{(nR_{PN}+R_L)^3}$$

$$C_2 = -\frac{\alpha^2 n^3 R_{PN}(K_H - K_C)}{2(nR_{PN}+R_L)^2} + \frac{\alpha^2 n^2 (K_H - K_C)}{nR_{PN}+R_L}$$

$$C_3 = -\frac{\alpha^2 n^2 (K_H T_s + K_C T_{amb})}{nR_{PN}+R_L} - (nK_{PN}+K_{ce})(K_H+K_C) - K_H K_C$$

$$C_4 = K_H K_C (T_s - T_{amb})$$

This governing equation can be solved to derive the closed form solution for T_s and ΔT. But due to its complexity, the exact closed form solution will not be displaced here. However, we can do some investigation on the simplification to the equation based on known parameters. For example, $C_1 \sim \alpha^4$, $C_2 \sim \alpha^2$, when ΔT is small, the first terms $C_1(\Delta T)^3$ is hereby orders lower than the seconder term $C_2(\Delta T)^2$, and the first term tend to be negligible. Thus the equation becomes a quadratic function, in which at least one solution can be tracked in the reasonable range, from 0 to $(T_s - T_{amb})$. When both the first and second terms can be neglected, only the last two terms remain in the equations, which leads to a linear relation between ΔT and T_s.

Since the parallel heat loss through insulating material is considered, then power generation can be calculated either through equation 35 or through equation 50. The efficiency in this case is derived as

$$\eta = \frac{P}{n * q_h + K_{ce}\Delta T} = \frac{I^2 R_L}{n\left(\alpha I T_h + K_{PN}(T_h - T_c) - \frac{1}{2} I^2 R_L\right) + K_{ce}\Delta T} \qquad (59)$$

4.5 Modeling methods in this work

Three modeling methods are investigated in this work.

Method I (constant heat flow model): this is the most simplified model to analyze the thermoelectric process, in which a constant heat flow is assumed in the thermal circuit. By assuming constant heat flow, the energy conversion in the module is neglected. The constant heat flow modeling is introduced in Energy harvesting book [1]. A typical heat transfer circuit based on this modeling method is shown in Figure 4-4.

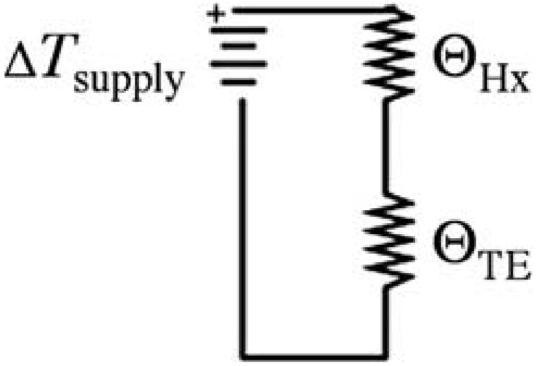

Figure 4-4 A typical thermal circuit in a thermoelectric energy harvesting device [1].

In this modeling, the heat flow is constant, thus the overall thermal resistance of system can be calculated as

$$R_{tot} = \frac{1}{K_H} + \frac{1}{2K_{pn}} + \frac{1}{K_C} \tag{60}$$

Then a heat flux can be calculated using equation 6-1. The voltage, power and efficiency can be calculated through equations 33~36.

Method II (constant heat sink resistance model): This model takes the energy conversion, parallel heat loss in module into consideration. The detailed process is described in previous section. The temperature difference is the main unknown variable that need to be solved using Equation 58. The heat sink thermal resistance is treated as a constant, whose value is the averaged thermal resistance in the working temperature and heat flow range. Then the voltage, power and efficiency can be calculated using equation 33~35.

Method III (heat sink resistance coupled model): In this model, the temperature's influence on the heat sink thermal resistance is considered and coupled to the existing system. The cold side conductance K_C is now a variable depended on the different heat flows through heat sink, which originally are induced by different source temperature. Thus, given an initial guess on the thermal resistance (took as mean value from Method II), an intermediate heat flow can be derived. Then by plugging the heat flow back to the thermal resistance iteration, a refined thermal resistance and therefore a final result of voltage, power and efficiency generation will be derived.

The difference of modeling 1 and 2 is the treatment of heat sink temperature, the uncoupled modeling took the average thermal resistance 0.891 into calculation; while the heat sink uncoupled modeling sets up an iteration depicted in Figure 4-5.

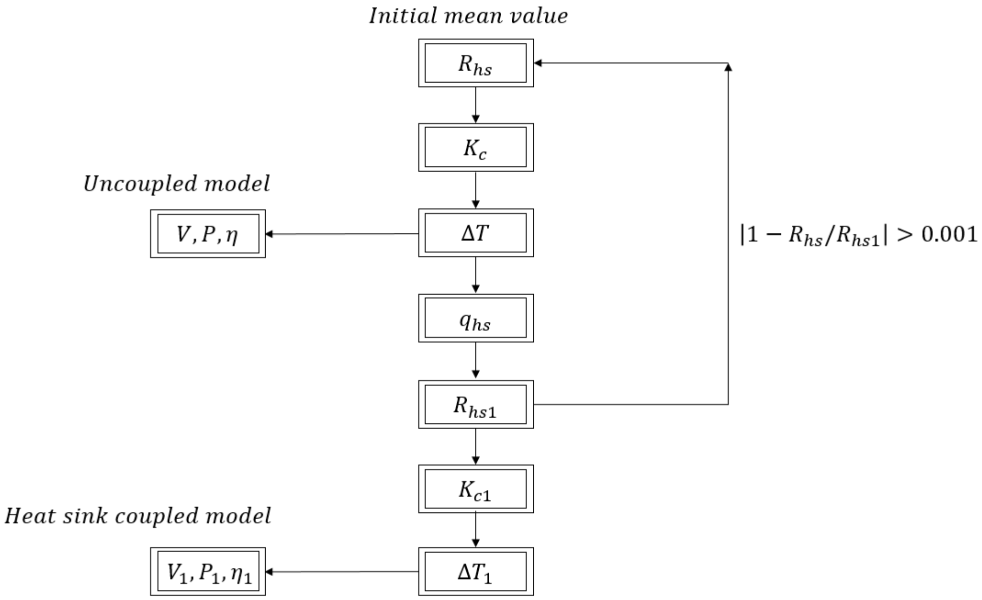

Figure 4-5 Schematic of method II (Uncoupled model) and method III (Heat sink resistance coupled model)

4.6 System level Optimization

In this part, the detailed value of variables in previous modeling will not be used. With T_h, T_c, $Q_h$and Q_c derived, the closed form solutions for open circuit voltage, power output and the efficiency in terms of T_s, T_{amb} and I can be determined as

$$\begin{aligned}V_o &= n\alpha(T_h - T_c)\\ &= [\alpha^2 n^3 I^3 R_{PN} + \alpha n^2 I^2 R_{PN}(K_H - K_C)/2 + n^2\alpha^2 I(K_H T_s + K_C T_{amb})\\ &\quad - n\alpha K_H K_C(T_s - T_{amb})]\\ &\quad \times [n^2\alpha^2 I^2 + n\alpha(K_H - K_C)I - (nK_{PN} + K_{ce})(K_H + K_C)\\ &\quad - K_H K_C]^{-1}\end{aligned} \tag{61}$$

$$\begin{aligned}P &= n\alpha I(T_h - T_c) - nI^2 R_{PN}\\ &= \Bigg\{-\frac{\alpha n^2 R_{PN}(K_H - K_C)I^3}{2}\\ &\quad + [n^2\alpha^2(K_H T_s + K_C T_{amb}) + nR_{PN}(nK_{PN} + K_{ce})(K_H + K_C) + nR_{PN}K_H K_C]I^2\\ &\quad - n\alpha K_H K_C(T_s - T_{amb})I\Bigg\}\\ &\quad \times [n^2\alpha^2 I^2 + n\alpha(K_H - K_C)I - (nK_{PN} + K_{ce})(K_H + K_C)\\ &\quad - K_H K_C]^{-1}\end{aligned} \tag{62}$$

$$\begin{aligned}\eta &= 1 - Q_c/Q_h\\ &= \{-\alpha n^2 R_{PN}(K_H - K_C)I^3\\ &\quad - [2n^2\alpha^2(K_H T_s + K_C T_{amb}) + 2nR_{PN}(K_H + K_C)(nK_{PN} + K_{ce}) + 2nR_{PN}K_H K_C]I^2\\ &\quad - 2n\alpha K_H K_C(T_s - T_{amb})I\}\\ &\quad \times \Bigg[\alpha n^2 K_H R_{PN} I^3 - 2nK_H\left(n\alpha^2 T_s + nK_{PN}R_{PN} + \frac{K_C R_{PN}}{2} + K_{ce}R_{PN}\right)I^2\\ &\quad + 2n\alpha K_H K_C T_s I + 2K_H K_C(nK_{PN} + K_{ce})(T_s - T_{amb})\Bigg]^{-1}\end{aligned} \tag{63}$$

Equations 61~63 provide direct interrelation between output and input parameters of this coupled system. The outputs, voltage, power and working efficiency, can now be evaluated in terms of system inputs, such as source temperature, ambient temperature, current and material properties.

The optimization techniques for this application can be in following areas:

1) Total pairs of P/N legs and electrical current: in another word, by adding more generators, and by using different external electrical load, the number of legs and current can be manipulated. In this simulation, N is the number of the pairs of modules at both sides of aluminum block, thus the total number of P/N legs at each side of adaptor is $N \times n$. The reason to add modules at both

sides simultaneously is to ensure the heat transfer circuit is symmetric so that the modeling above can be applied.

2) K_H and K_c value and ratio: By tuning the contact resistance, both hot side and cold side configurations, the aggregated thermal conductance K_H and K_c can be adjusted to find the maximum ratio and value.

3) K_{ce} and K_{pn} ratio: K_{ce} here could refer to any kind of sealing material surround the P/N legs (could be air conductance, which will bring the convection and radiation, or vacuum which means K_{ce}=0).

4) Heat sink geometry: For a given size of heat sink, selecting the optimum fin geometry.

The optimization target variables to which the techniques can be applied are

1) Power output

2) Efficiency

3) Voltage output

5 Experimental

5.1 Lab-based experiment

In the lab-based test, setting up a steam pipe is obviously impractical, thus a brass block is designed to substitute for steam pipe and served as the heat source. A 1.5 inch long 200W cartridge heater, CIR-10151/120V from OMEGA Engineering, is used to heat the brass block. For better thermal conduction on each interface, efficient thermal conductive grease from OMEGA Engineering is used to further reduce contact resistance and meanwhile provide good electrical insulation between TEGs and metal surfaces.

A temperature controller was brought from OMEGA Engineering to control the temperature of cuboid brass heat source. Two temperature increasing rate, 10K/20min and 10K/10min, were adapted in the experiment to examine the stability of temperature profile. The temperature range selected for the lab-based test is from 30 ℃ to 250 ℃. The controller was programmed to ensure the source temperature increases slowly and smoothly. Therefore, for each measurement, the assumption that heat transfer in each element is in steady state is valid.

Temperature at five targets are measured through K type thermal couples and recorded by NI temperature DAQ; the voltage generation of each single TEG and two in series were collected in open circuit and match load cases with another NI DAQ, respectively. The first prototype and experimental setup for match load case measurement in lab-based test is shown in Figure 5-1 and 5-2.

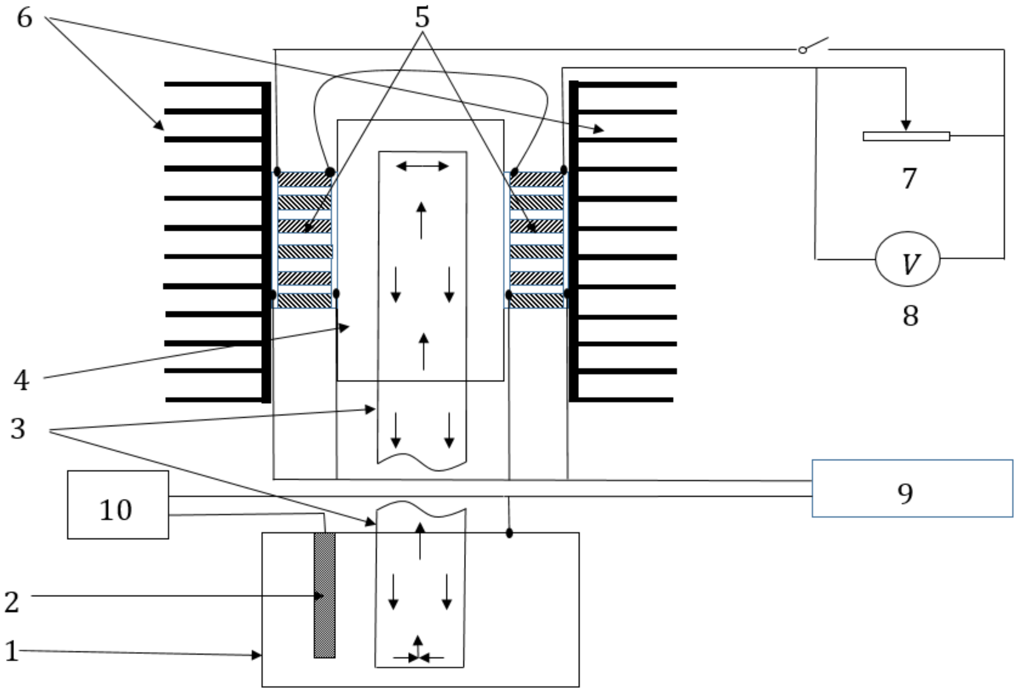

Figure 5-1 Schematic diagram of thermoelectric generator experimental setup. 1: Heat source block. 2: Cartridge heater. 3: Heat pipe. 4: U shape hot side block. 5: Thermoelectric modules. 6: Heat sinks. 7. Electrical load. 8: Voltage reading DAQ. 9: K type thermal couples and temperature reading DAQ.

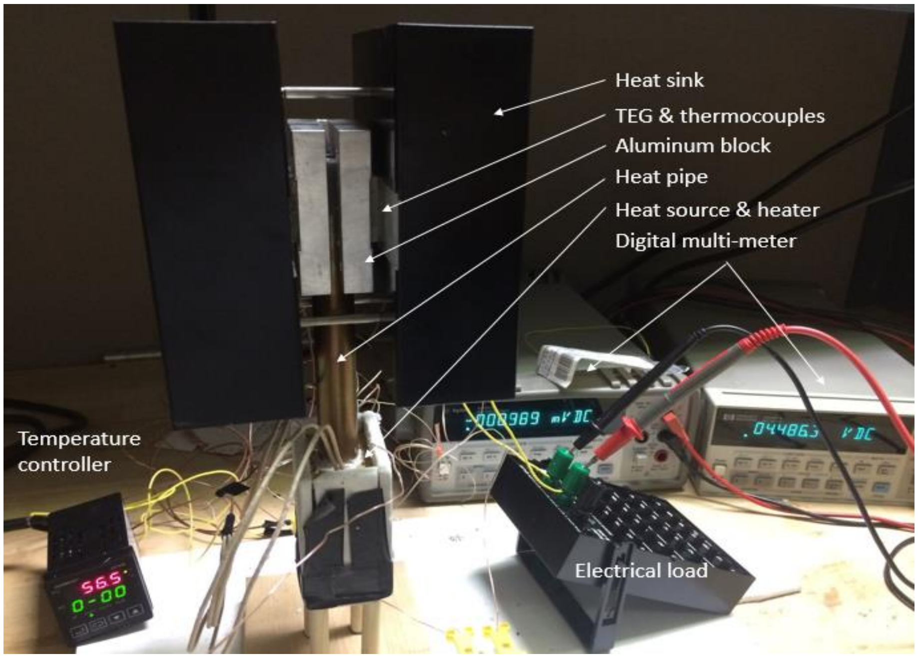

Figure 5-2 Prototype and the assembly for lab-based test

To demonstrate the effectiveness of heat pipe in this project, a comparison study has been conducted. By using an aluminum rod with exactly same dimension as heat pipe to substitute the heat pipe and repeating experiments under the same condition, the significance of heat pipe in the overall system can be evaluated. In fact, aluminum, with its high thermal conductivity of 167 W/(m·K) and excellent machinability, is a reasonable substitution for heat pipe as baseline.

5.2 Radiation-based experiment

A radiation-based in-situ experiment was performed to test the gamma radiation impact on the thermoelectric generator, power management circuit and wireless communication circuit. The first phase of radiation-based experiment, which is on the generator assembly and thermoelectric modules, was completed in collaboration with Westinghouse Electric Company in Pittsburgh.

The prototype was setup at a certain distance to the gamma radiation source in the radiation chamber so that the gamma radiation dosage collected after the experiment can reach to the accumulated dosage level of implementing device on a secondary loop in PWR for 40 years. Another 3 identical clean hz-2 thermoelectric modules were deployed at various distances to the gamma radiation source, by which different accumulated dosage in 3 modules can be yielded eventually.

The experimental setup is shown in the following Figure 5-3. The radiation chamber was insulated with thick metal walls. Cables can be extended from the inner side to the outside through the holes on the wall, which will be sealed with plugs after setting up. Lead bricks are placed in front of the holes so that gamma radiation through the holes can be blocked. The prototype was tilted to face the radiation source together with 3 modules placed at different distance to the radiation source. Three modules were sealed after the radiation process, and were tested in Virginia tech.

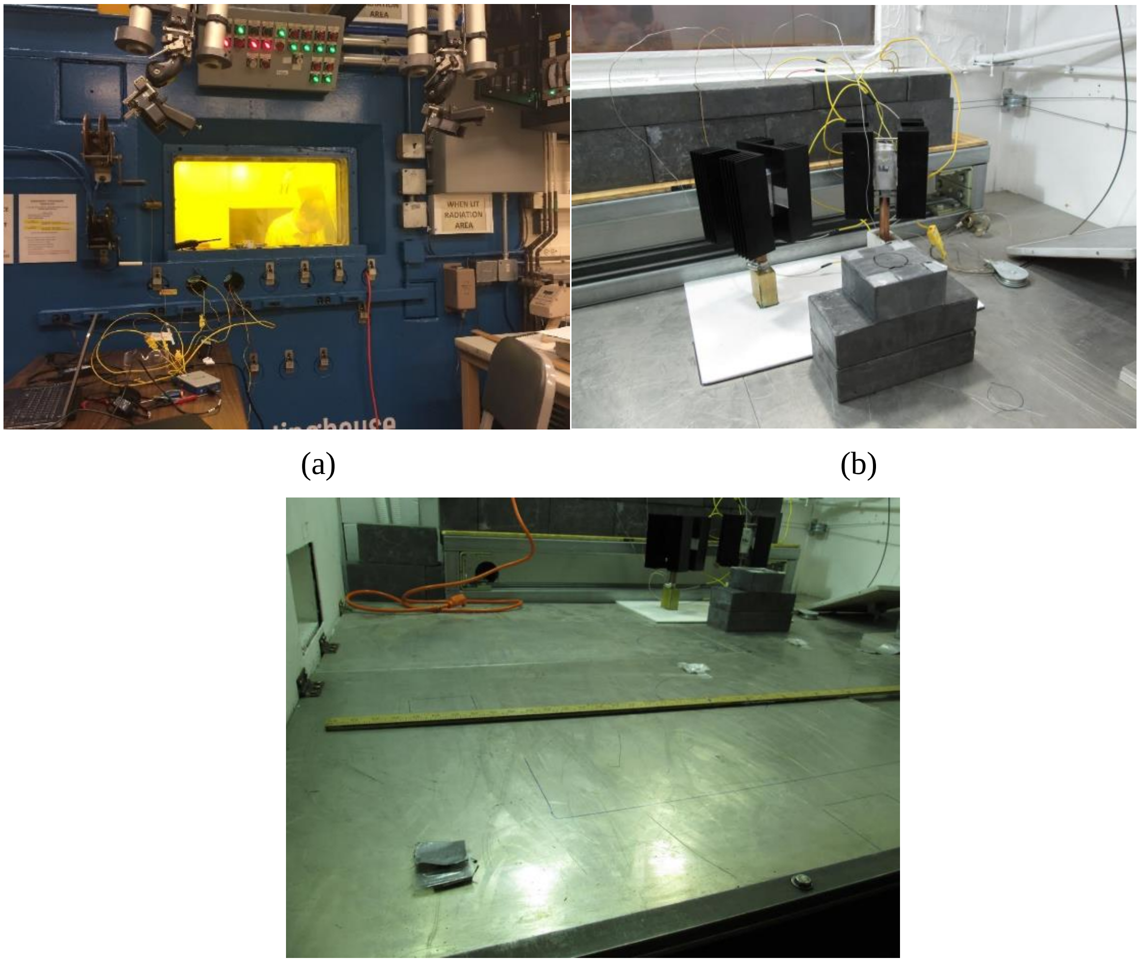

(a) (b)

(c)

Figure 5-3 Radiation experiment setup: (a) outside chamber; (b) assembly setup; (c) single modules deployment

As is stated above, the current phase of project is targeting on secondary coolant loop where radiation level is low. The accumulated gamma radiation in this area during a single period (around 40 years) is about 10^6rads. Therefore, the assembly and the nearest module were designed to receive at least same level of gamma dosage to verify the feasibility of harvester in nuclear radiation condition. Dosimetry were attached to the samples to collect radiation dosage during the experiment.

The distance between modules and the radiation source and corresponding accumulated dosage level are giving as follow

Table 5-1 Details of dosage level reached in gamma radiation experiments

	Assembly	Module 1	Module 2	Module 3
Dosimetry results (rads)	1.36×10^6	1.36×10^6	6.79×10^5	4.07×10^5

After radiation, the assembly set and the three thermoelectric modules were brought back to Virginia tech and tested immediately. The detailed results regarding to the experimental results will be discussed in next chapter.

6 Results and discussions

6.1 Heat sink optimization and selection

An optimization study has been done for the heat sink geometry and performance. According to the thermal circuit net resistance calculation, a heat sink with smallest size and smallest thermal resistance is desired. The detailed parameters involved in the simulation are listed in the following table

Table 6-1 Detailed parameters for heat sink simulation

Parameter items	Value
Ambient temperature	25 ℃
Heat sink thermal conductivity	205 W/(m·K)
Thermal conductivity of air at T_{sink} (50 ℃)	0.02816 W/(m·K)
Kinetic viscosity at T_{sink}	1.807x10^{-5} m^2/s
Thermal expansion coefficient	0.0032
Prandtl number	0.71
Emissivity of anodized aluminum	0.77
Stephen-Boltzmann constant	5.67 x10^{-8}

However, a heat sink cannot be made as small enough and the fins cannot be designed as condensed as possible since the fins have an optimum distance as stated in previous chapter. With a given size of heat sink, the fin number and height are two variables that could be optimized. Based on the detailed modeling of the heat sink, the fin height and numbers are selected from 0 to 0.2m, and from 4 to 14, respectively. The heat sink thermal resistance and fin efficiency in terms of fin height and numbers are plotted in Figure 6-1 and Figure 6-2.

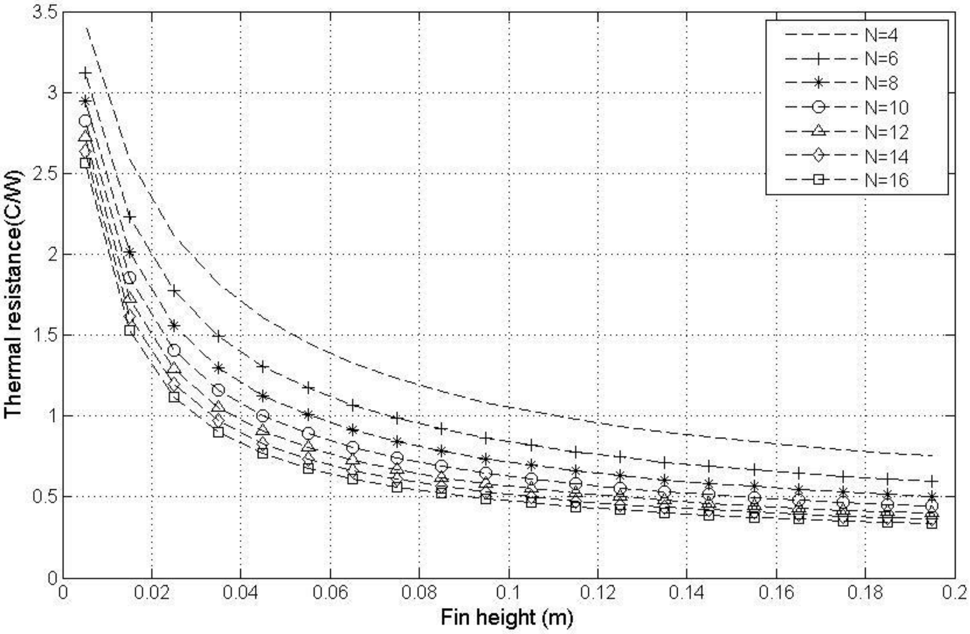

Figure 6-1 Heat sink thermal resistance in terms of fin height and fin numbers.

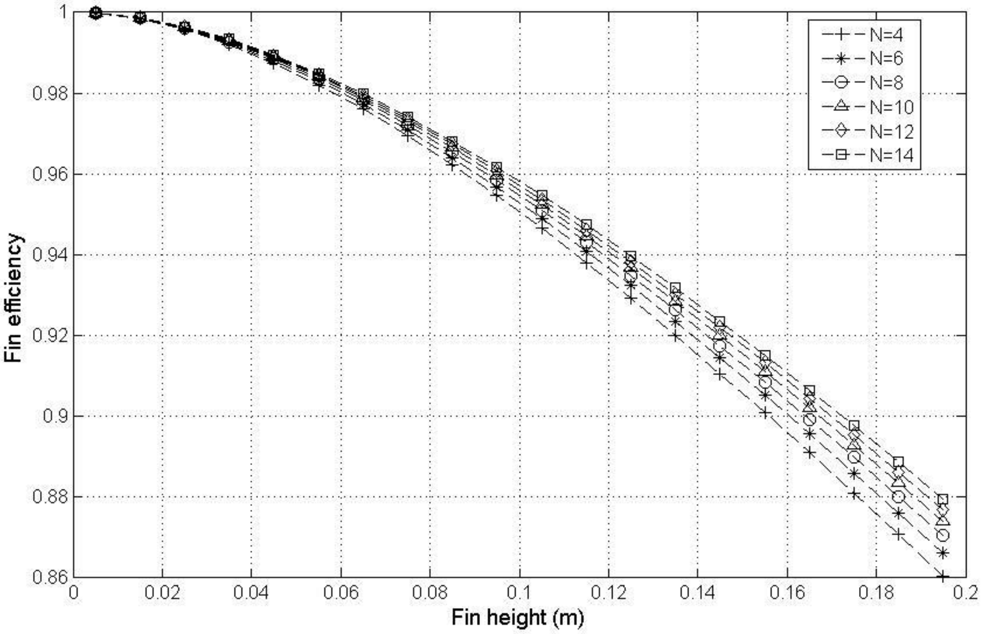

Figure 6-2 Heat sink fin efficiency in terms of fin height and fin numbers.

Figure 6-1 indicates two facts: The first fact is that with the increase of fin height, the thermal resistance will drop fast initially, then decrease mildly after reaching about 0.04m and finally saturated at a certain value. This means after the fin height reaches to a critical value, the natural convection will not be enhanced since the extra height from the base plate will not be utilized. The second fact is that when the number of fins increases, the reduction in thermal resistance is getting smaller, and finally saturate at a certain number. As shown in Figure 6-1, the fin numbers of 12 and 14 will leads very limited increase, less than 10 %, at each same fin height.

Figure 6-2 indicates similar trends as indicated in Figure 6-1, where larger fin height yields less fin efficiency, and increasing fin number yield gradually reduced improvement in fin efficiency.

Unfortunately, all the simulation above is based on ideal case, in which customization in heat sink will be needed. Making a customized heat sink can be time-consuming and expensive in current situation. Therefore, using a commercial product that has similar geometry is more advisable. The heat sink chosen here has a fin height of 0.041m, closed to the critical value, and a fin number of 10 (Note that the heat sink has a blank area without fins in the center. The average fin space in the finned area is closed to the N=14 case (the reduction in the wetted area can be compensated by increasing heat sink length). The calculated heat sink thermal resistance is actually a variable that changes with different heat flow values. The performance of this heat sink is examined by using a simulation with Comsol heat transfer model, due to its irregular shape. The input heat flux and the ambient temperature are fixed to 50W and 25 ℃, respectively. Then by finding the mean temperature at the input surface, the overall thermal resistance is acquired as 1.16K/W in this case.

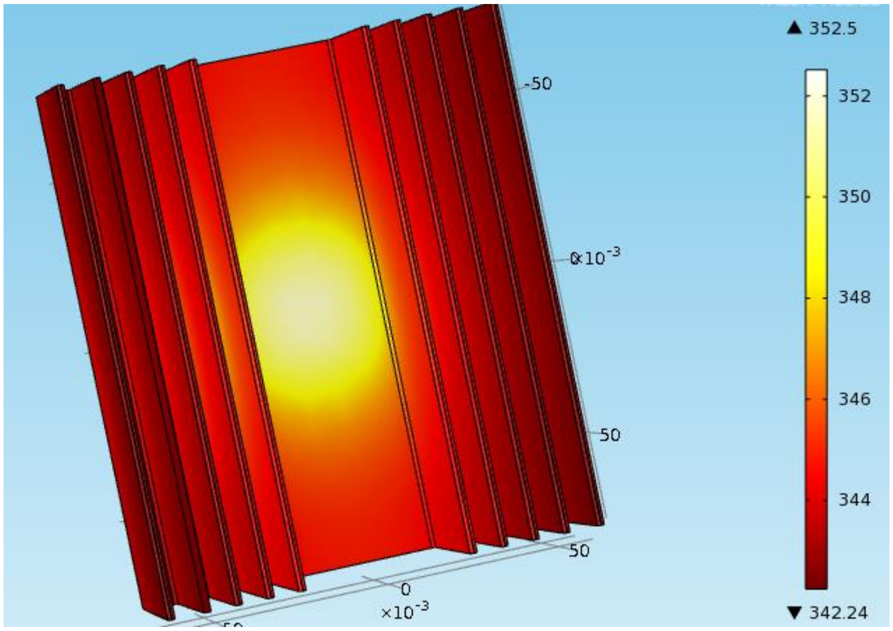

Figure 6-3 Finite element validation of heat sink performance.

The detailed analytical results of heat sink thermal resistance will be introduced in later sections. Based on above analysis, the selection of heat sink is reasonable in terms of its balance between geometry and performance.

6.2 Open circuit voltage and Seebeck coefficient

Due to the existence of individual difference between thermoelectric modules, the open circuit voltages of two modules are tested with the assembly to calculate the Seebeck coefficient of each module. The repeatable results of open circuit voltage generation profile and temperature profile are summarized in following Figure 6-4.

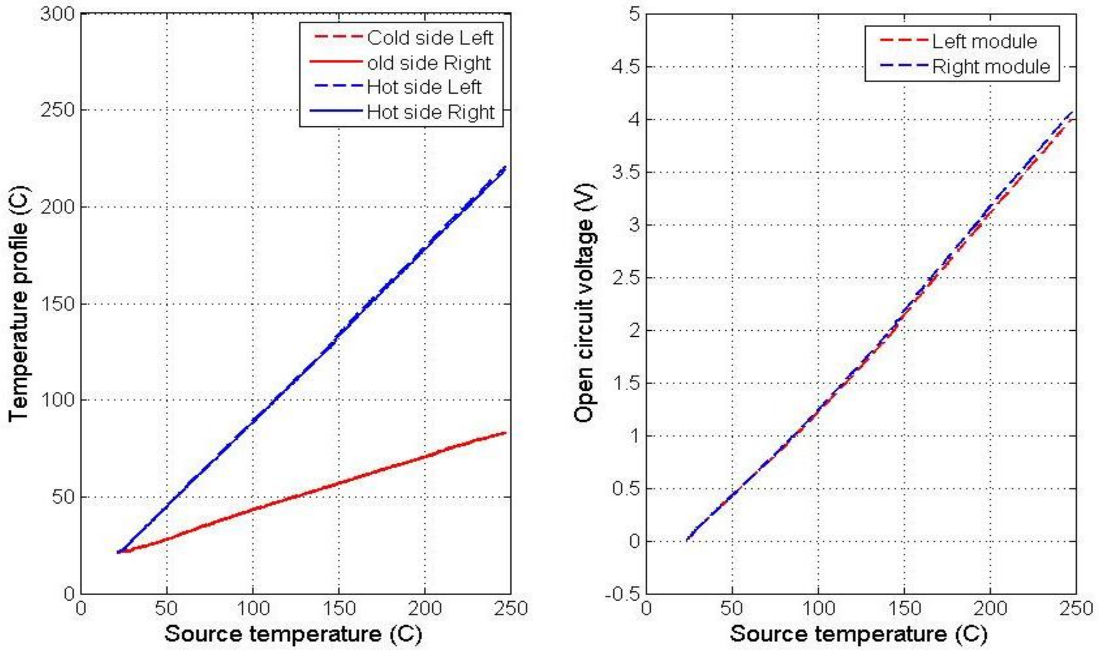

Figure 6-4 Temperature distribution of modules at both sides, “symmetricity verification” (left); Open circuit voltage (right).

Figure 6-4 (left) shows the temperature distribution of both modules. In this figure, the overlapped curves indicate that only a very small difference exists between the hot side temperatures of two modules, which may come from individual property difference. In fact, the hot side temperature has a 1.5 ℃ difference as the source temperature reaches to 246 ℃. Figure 6-

4 (right) depicts the voltage generation curves of both modules, where we can see the difference between the open circuit voltage is small, and both reach to about 4V as the source temperature approach to 250 ℃.

Figure 6-5 shows the difference of Seebeck coefficient between experimental and datasheet value. The difference between experimental results and its datasheet value is large, which might be from the measurement error or the individual difference between TE modules. The averaged summed Seebeck coefficient of P/N on this range can be calculated using equation 2-1 as 0.285 mV/K.

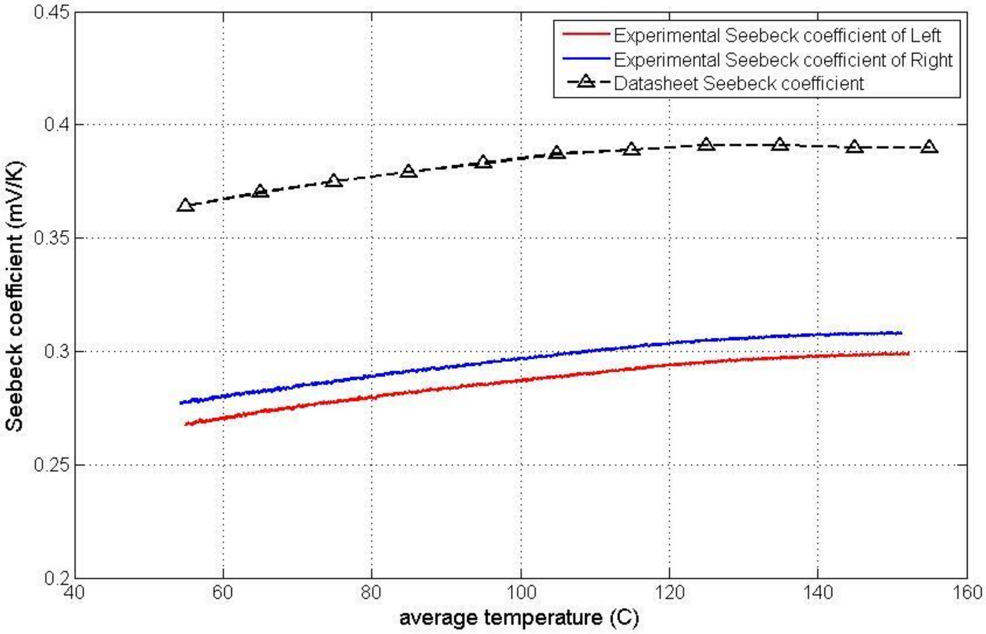

Figure 6-5 Comparison of seebeck coefficient from data sheet and open circuit experiment.

6.3 FEA simulation with core parts

6.3.1 Case 1 FEA simulation for module

To verify the 1-D model of thermoelectric module input parameters, a finite element simulation based on the exact dimensions of product was carried out. At first, a CAD 3-D modeling of TEG was drafted using Solidworks; and then the modeling was imported to the commercial Finite Element Analysis (FEA) software Comsol.

The simulation was done in Comsol Multiphysics by directly using Partial Differential Equation modeling, instead of using existing heat transfer or electrostatic models, since the coupled system cannot be solved with either one. The following governing equations are written directly into the unit-less mathematical code. For this steady state simulation, the coupled governing equations of thermoelectric process can be written as follow.

$$-\nabla\big((\sigma\alpha^2 T + k)\nabla T\big) - \nabla(\sigma\alpha T\nabla V) = \sigma((\nabla V)^2 + \alpha\nabla T\nabla V) \tag{64}$$

$$\nabla(\sigma\nabla V) - \nabla(\sigma\alpha\nabla T) = 0 \tag{65}$$

where V and T are the two variables; symbol ∇ refers to gradient. In this FEA model, Thomson effect and the convection effect at the edges are neglected; the transient heat diffusion term is also ignored. Note that the heat transfer and the electrical force are analyzed in 3 directions, thus the difference caused by the 1-D assumption in the analytical modeling can be examined. The temperature dependent Seebeck coefficient, electrical and thermal conductivity are read from product's data sheet. The boundary conditions for this system are temperature at each side and electric potential at one of the two electrical connection pins.

The material properties chosen for this simulation are manually imported from product datasheet. The Seebeck coefficient value of the thermoelectric module is 0.378mV/K, which is the averaged value of P/N summed Seebeck coefficient in its working temperature range. The thermal conductivity and electrical conductivity of the module are also the averaged values in the working temperature range. The detailed input material parameters are summarized in the following table.

Table 6-2 Detailed TEG material parameters in the Comsol model

Parameter item	Value
P/N type leg geometry (mm)	2.98(Height)x1.52(Width) x1.52(Length)
P-type leg Seebeck coefficient (mV/K)	0.201
N-type leg Seebeck coefficient (mV/K)	-0.177
P-type leg thermal conductivity (W/m·K)	1.373
N-type leg thermal conductivity (W/m·K)	1.054
P-type leg electrical resistivity (Ω·m)	$1.53\text{x}10^{-5}$
N-type leg electrical resistivity (Ω·m)	$1.53\text{x}10^{-5}$
Aluminum thermal conductivity (W/m·K)	205
Aluminum electrical resistivity (Ω·m)	$2.7\ \text{x}10^{-8}$
Insulation thermal conductivity (W/m·K)	1.74

Figure 6-6 shows the temperature distribution and the voltage generation result of a single thermoelectric module. The insulation layer has been hidden so that the inner structure can be displayed.

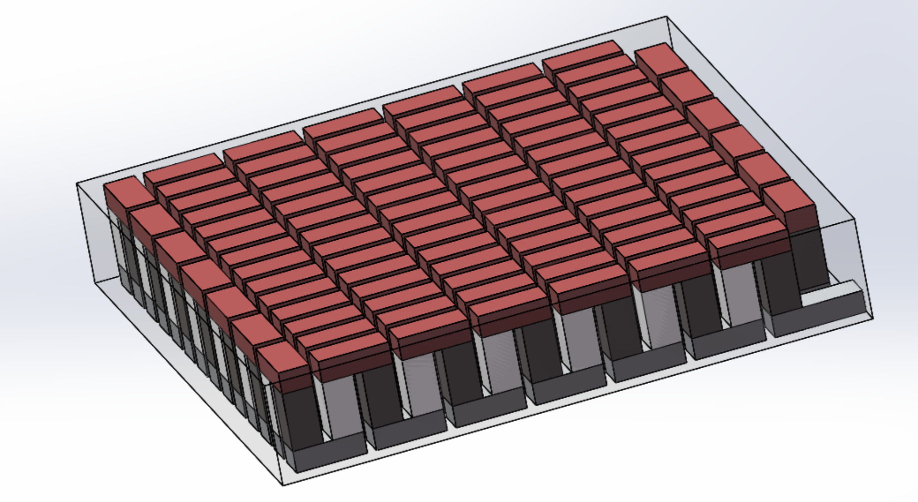

(a)

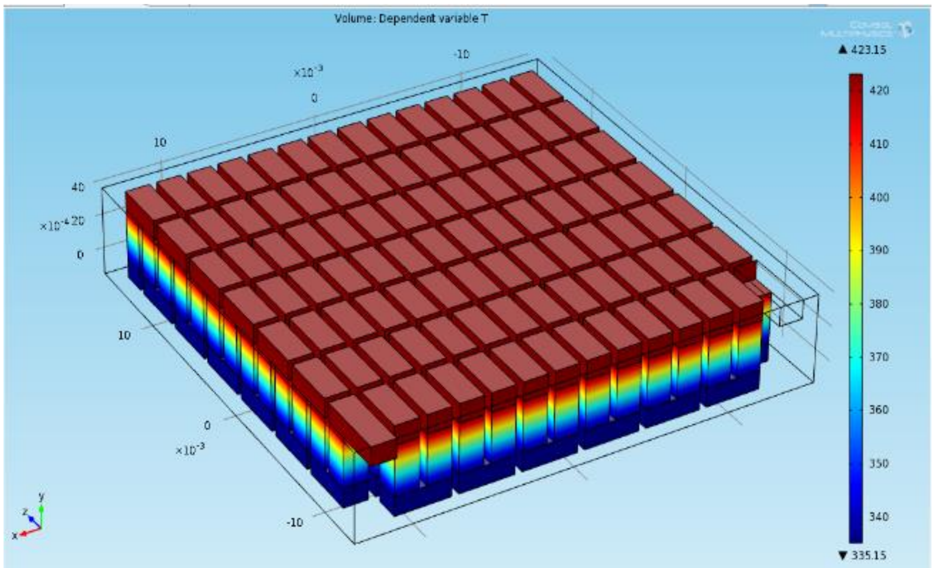
Volume: Dependent variable T
▲ 423.15
420
410
400
390
380
370
360
350
340
▼ 335.15
×10⁻³
0
-10
10
40
×10⁻⁴ 20
0
10
0
×10⁻³
-10
y
z
x

(b)

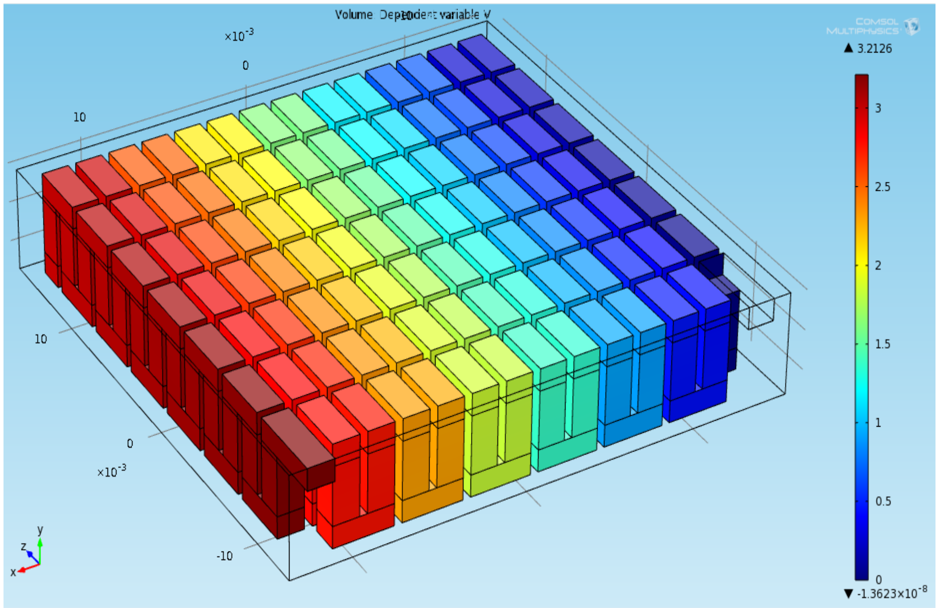
Volume: Dependent variable V
-10
▲ 3.2126
3
2.5
2
1.5
1
0.5
0
▼ -1.3623×10⁻⁸
×10⁻³
0
10
10
0
×10⁻³
-10
y
z
x

(c)

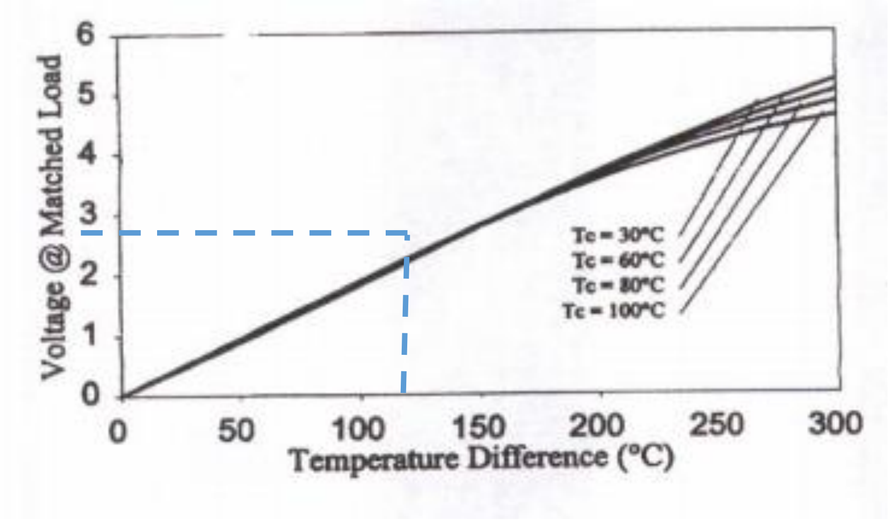

(d)

Figure 6-6 Thermoelectric module simulation results, as hot side temperature $T_h = 150°C$, $T_c = 60°C$. (a) CAD model of TEM (b) the temperature distribution across the whole elements; (c) open circuit voltage generated between two pins, $V_o = 3.21V$. (d) Match load voltage from data sheet

The open circuit voltages under different temperature differences are collected in the following table.

Table 6-3 FEA simulation results of thermoelectric module under different profiles.

Hot side temperature (K)	Cold side temperature (K)	Temperature difference (K)	Open circuit voltage of a single module (V)
323.15	303.15	20	0.7274
343.15	303.15	40	1.4548
363.15	303.15	60	2.1822
383.15	303.15	80	2.9096
403.15	303.15	100	3.6368
423.15	303.15	120	4.3640
443.15	303.15	140	5.0914
463.15	303.15	160	5.8184

The error between the datasheet and the FEA simulation results in terms of match load voltage values is less than 2%.

6.3.2 Case 2 FEA simulation on half assembly

To verify the temperature profile of the whole system, another finite element simulation for a core assembly was performed, where the heat pipe here was neglected since its thermal resistance is small. Two heat transfer governing equations in two domains, the heat sink and the adaptor, are added to the system in additional to the energy generation process in the module. The assumptions made here include all assumptions in the previous single TEG module simulation. In addition, the model assume the heat transfer and energy conversion process are symmetric; the interfaces were set to be heat resistive layer with same resistance as thermal grease layer. In addition to the boundary conditions applied in previous one, convective coefficient at the wetted surface of heat sink is assumed. The convection boundary condition is given as

$$-\vec{n}\cdot(-k_b \nabla T) = h(T - T_{amb}) \tag{66}$$

where, $\vec{n}$ represents the normal vector to the wetted surface of the heat sink, k_b is the thermal conductivity of the aluminum heat sink base (same material in base and fins).

The temperature profile and open circuit voltage generation following temperature boundary conditions and $3.1\ W/(m^2K)$ as convective coefficient are discussed. The following figures show the temperature contour of the assembly and the voltage generation on a single TEG.

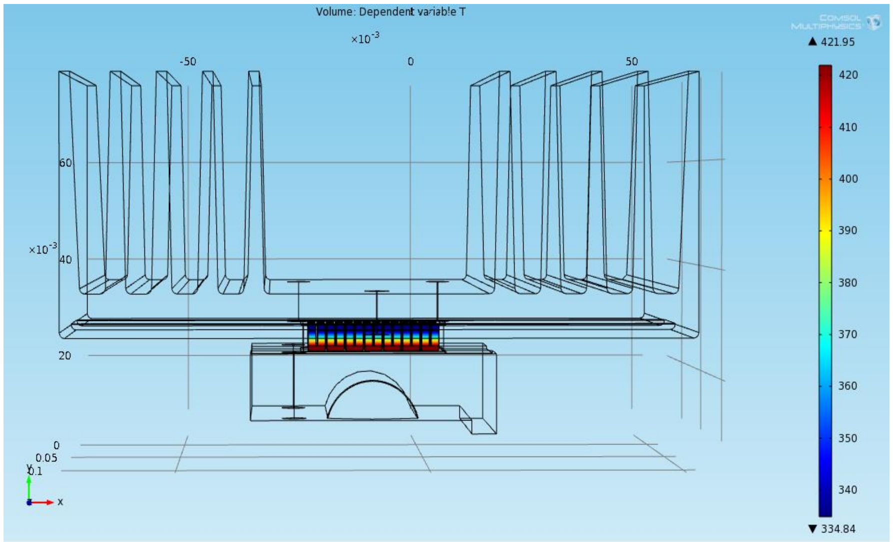

(a)

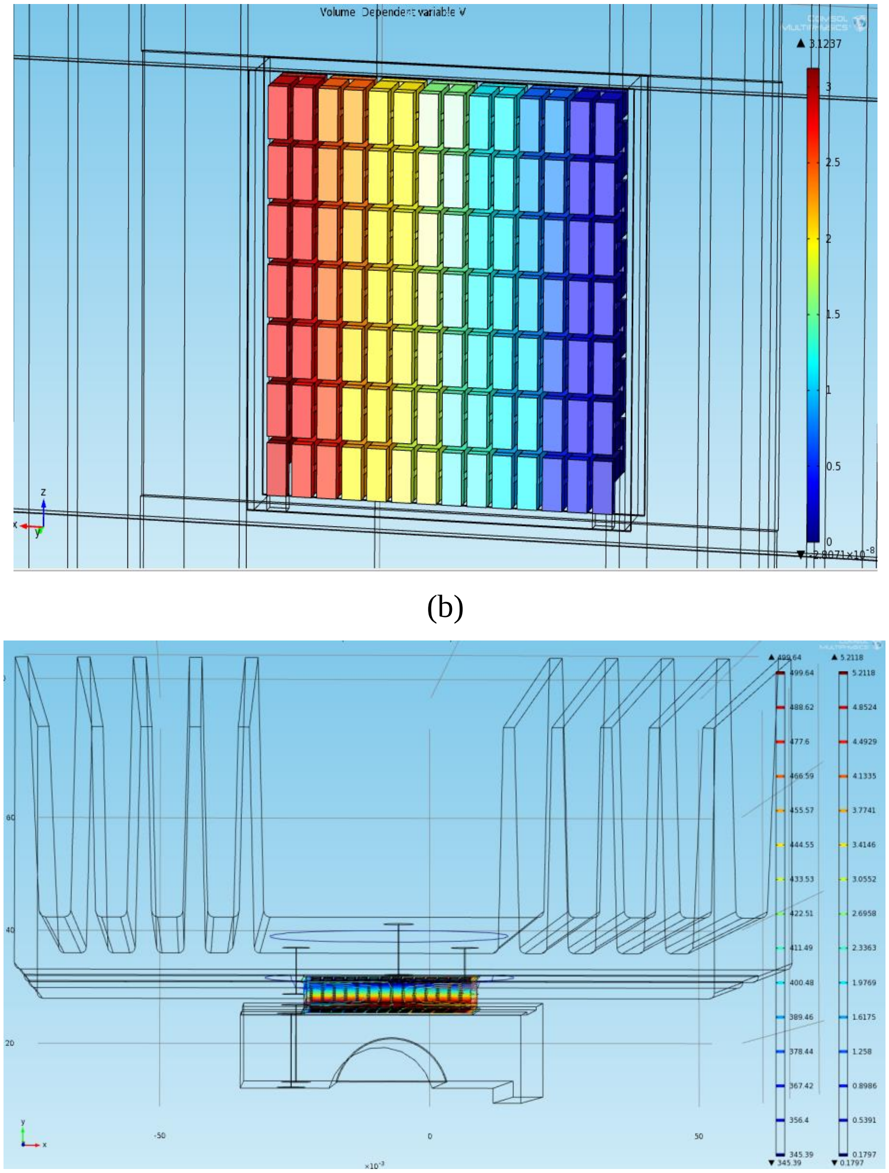

(b)

(c)

Figure 6-7 Temperature contour of a half system (a), Open circuit voltage under given conditions (b). The input boundary conditions are: $T_H = 150℃$, $T_{amb} = 25℃$, $h_c = 3.1\, W/(m^2K)$. (c) The open circuit voltage and temperature contour with boundary conditions: T_H=231 ℃, $T_{amb} = 25℃$, $h_c = 8.98\, W/(m^2K)$

Figure 6-7 shows the initial guess on the convective heat transfer coefficient, since it is unknown in this mathematical FEA simulation. A result and its boundary conditions are listed in Figure 6-7 (a)-(b). Then a simulation based on analytical results is shown in Figure 6-7 (c), with boundary conditions as T_H=231 ℃, $T_{amb} = 25℃$, $h_c = 8.98\, W/(m^2K)$. This result can be used to compare with experimental results shown in section 6.2, with an error around 20%.

6.4 Simulation & Lab-based experimental results

In the lab-based test, the steam pipe is substituted with a brass block, whose equivalent thermal resistance needs to be identified firstly. The center-to-center distance between heat pipe and cartridge heater is 25.4mm; the height and the width of cuboid metal source are 61mm and 30mm, respectively. The outer surface of the cuboid heat source is enveloped by a layer of thermal insulation ceramic to reduce the heat conduction to the base and the convection with the air. Thus, we assume there is no heat loss in the heat source.

$$R_{sl} = \frac{L_s}{k_s H_s W_s} = 0.129\,(\mathrm{K}/W) \tag{67}$$

6.4.1 T_s impact

Figure 6-8 shows the temperature profile of hot side temperature T_h and cold side temperature T_c, in terms of heat source temperature from both 3 different analytical modeling methods and experimental results. For hot side temperature, since both 3 modeling methods focused more on the TEM and cold side, all of three modeling provided very close estimation in the whole temperature range with error less than 5%. For cold side temperature, in temperature range higher than 150 ℃, the simplified modeling yields the moderately accurate estimation of temperature, with an error of 5%. The constant resistance modeling offers the worst estimation on the temperature distribution with 14.5% error, which might be triggered by the error in estimating thermal resistance of heat sink. The refined modeling considering the coupling of resistance and temperature reach to the most accurate estimation of temperature profile, with an error less than 4% among whole temperature range. In high temperature range, the heat sink coupled method predicts less heat sink thermal resistance, which leads to a lower cold side temperature. However, this trend does not appears evidently in the lab-based test, which might because the increased heat loss in entire system in high temperature range counterbalances the effect of reduction in heat sink thermal resistance. In fact, both modeling considered radiation and convection on heat sink and assumed the heat dissipation through all elements except heat sinks to be negligible. In other words, the system is well thermally insulated. However, the influence of radiation and convection on other parts rather than heat sinks increases along with that on heat sink in high temperature range.

The result in Figure 6-8 also suggests that the system could achieve about 130℃ temperature difference as the source temperature reach to 245 ℃, which is a considerable result among the whole available 220 ℃ temperature difference from source to ambient. The hot side temperature will be less than the maximum operation temperature, 250 ℃, and closed to 230 ℃, which is the suggested working temperature with highest efficiency from datasheet.

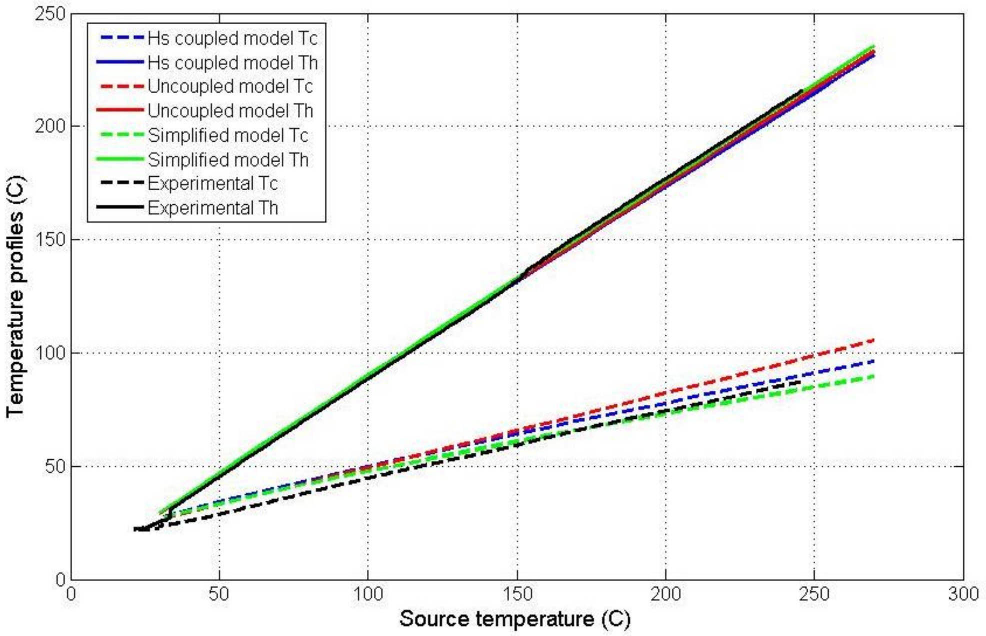

Figure 6-8 Hot side temperature and cold side temperature results in different modeling and experimental results.

Figure 6-9 shows the match load voltage and power generation in terms of source temperature. An external load at 7.9 Ω, closing to the internal resistance 7.86 Ω, was used for this test. The match load voltage is achieved experimentally at 246 ℃, with a value of 4.15V. Both heat sink uncoupled and coupled models achieved very accurate results at low temperature range (<150 ℃) with error less than 1.5%. As source temperature increases, the uncoupled modeling provides best result, the coupled modeling achieves moderate results and the simplified modeling offers the most deviant results. At 246 ℃ for source temperature, the method II and III yield 4.25V and 4.5V, respectively. The power generation curve exhibits similar trend as the voltage curve, with coupled resistance model owning the best estimation in low temperature range and uncoupled model yielding the best in high temperature range. At 246℃, the experimental power output is 2.22W, while the uncoupled model and coupled model estimate values of 2.27W and 2.51W and error of 2.2% and 11.5%, respectively. The experimental result does not exactly follow a quadratic curve, which further proves that in high temperature range, the heat loss is getting significant and cannot be overlooked.

Figure 6-10 indicates that the simplified model shows a linear relationship between source temperatures and module overall efficiency, while the other two give curved lines. The error between modeling result and the data sheet value is about 5%. The result shows that the heat sink's impact is more obvious at high temperature. The difference between the two sophisticated models and the simplest one primarily comes from the fact that the refined models took heat loss through insulating ceramic into consideration. In fact, the high thermal conductivity of insulating material will reduce the heat flow through P/N legs significantly, which eventually reduce the power generation within the same input heat flow. The simplest model does not consider the energy loss through insulating materials around TEM and the energy conversion from heat to electricity. The experimental result of efficiency is not acquired since the measurement of heat flow is almost impossible when the controller is applied. The inconstant heat flow from the controller, aiming at maintaining the source temperature stable, rendered the measurement through common heat flux sensors unavailable.

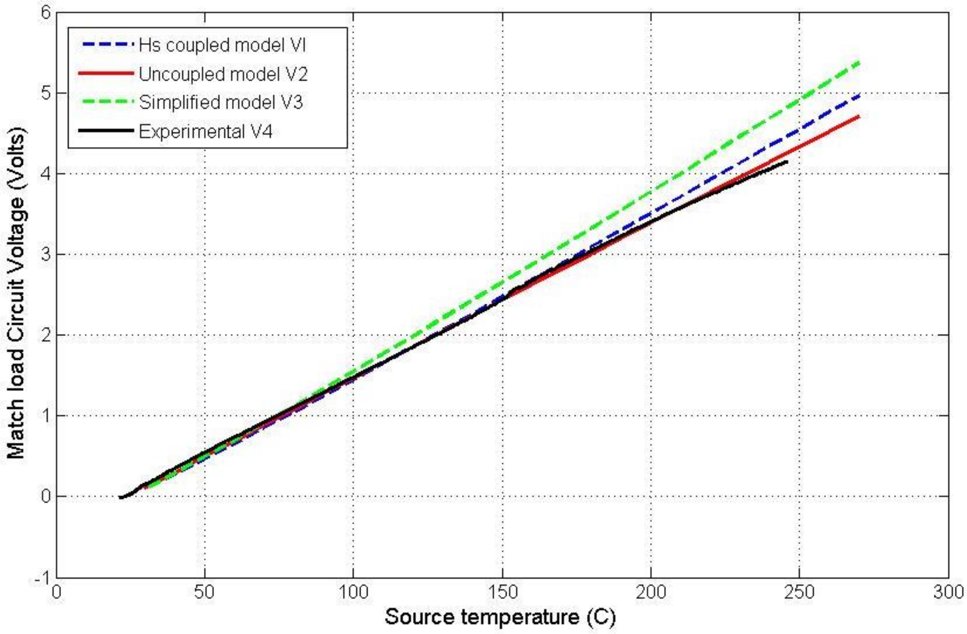

(a)

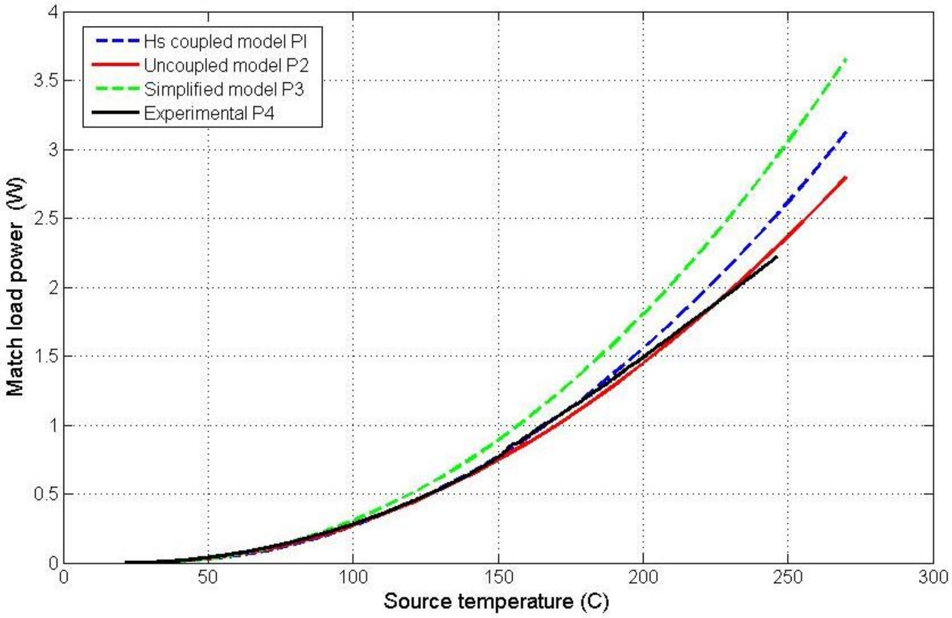

(b)

Figure 6-9 Match load voltage generation at $R_L = 7.8\Omega$ vs source temperature (a); Match load output power vs source temperature (b).

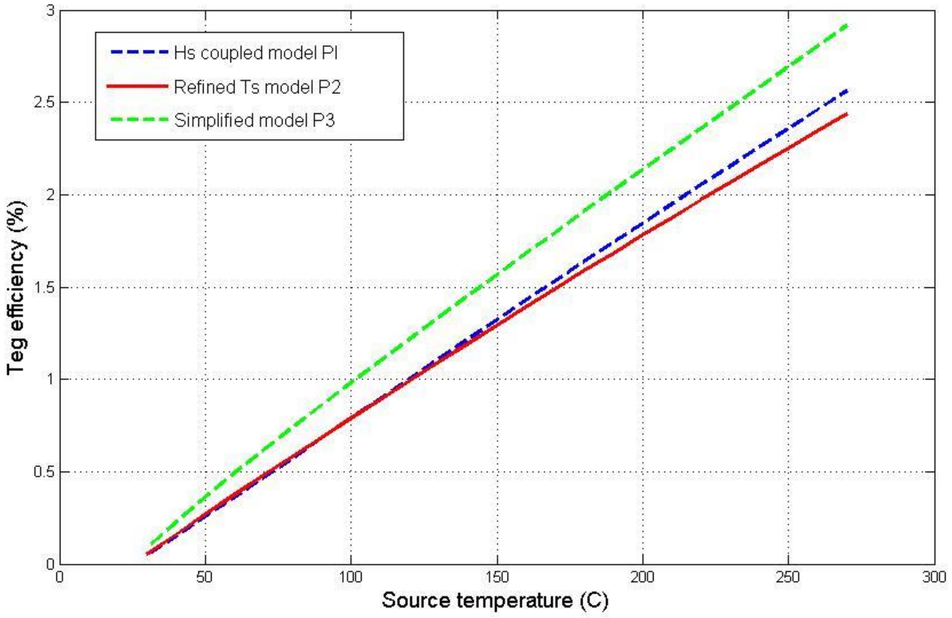

(a)

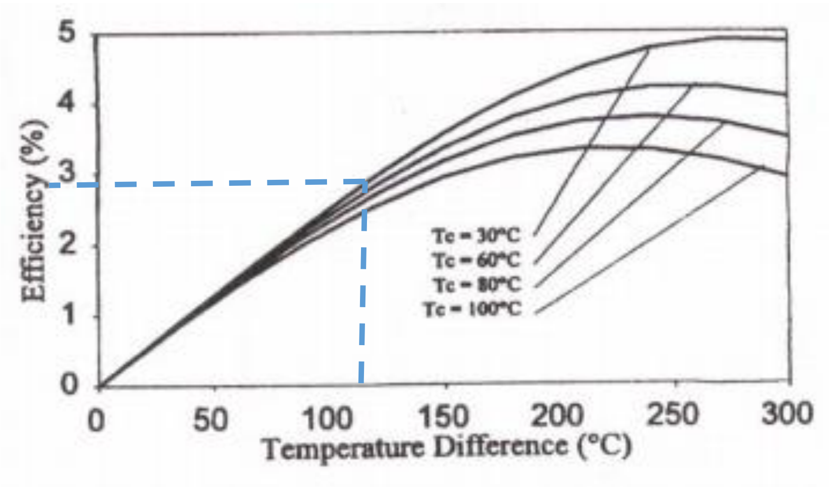

(b)

Figure 6-10 Efficiency of module vs source temperature. (a) Modeling results; (b) Hi-z2 datasheet

Comparing to the efficiency from the data sheet, the efficiencies estimated by Method II and III are lower than the values in data sheet, which is primarily due to the heat loss through sealing material is considered in these methods.

It also should be noticed that, in the high temperature range, both Methods estimated higher values than experimental results, and the proposed Method III has even lower accuracy than Method II. Both of these deviances might be caused by following to facts: 1) the error in measurements, especially the inaccuracy of resistor; 2) all models neglect the heat loss through the source, the heat pipe, the adaptor and modules, whose impacts increase with the temperature.

6.4.2 External load impact

To analyze the impact of external load on the voltage, power generation and the coupling effect between thermal circuit and electrical circuit, a resistor box, whose resistance range is set to be 0Ω to 20Ω, is connect serially with the TEGs. The measurements were taken under different temperature conditions from 100 ℃ to 250 ℃.

Figure 6-11 depicts the voltage generation under various temperature differences and external loads. The trend that heat sink coupled model offers closest match load circuit voltage under fixed temperature still exists in all temperature range; while in low temperature range, the simplified modeling yields better result than uncoupled modeling. However, the error from the modeling results compare to experimental results in the high temperature range is large, with 14.7% achieved by the heat sink coupled model at 20 Ω, and more than 20% for uncoupled model. Figure 6-12 shows the external load's effect on the power generation under different source temperatures. From this figure, the maximum power in each temperature case is reached as the external load equals to TEG internal resistance in series. Under the 250 ℃ of source temperature, the uncoupled model and coupled model predict maximum power of 2.58W and 2.92W, respectively, both of which are higher than the experimental values. Due to the second order of the voltage in power calculation, the error of refined model becomes significantly large, more than 21%.

It should be noticed that the reason for this relatively large error lies in two directions: 1) material properties change within temperature is not considered in the modeling 2) Experimental measurement error. The first reason can be easily proved by fact that the four experimental results curves provided yielded peak values at different external resistance, which suggests the internal resistance varies through the temperature range, instead of being a constant. The second one can also possibly result in large error since the resistor box used is not accurate enough and measurement of resistance in low resistance range is difficult.

The efficiency diagram of three models at different load are plotted at Figure 6-13, from which one can identify the maximum efficiency of system will be achieved as the external load reach to 10Ω in all temperature cases. This further proves that power and efficiency of the system have different dependency on the external load, which could theoretically be derived from governing equations. The maximum efficiency is reached at 2.29% for coupled modeling, while the efficiency at the match load is 2.15%.

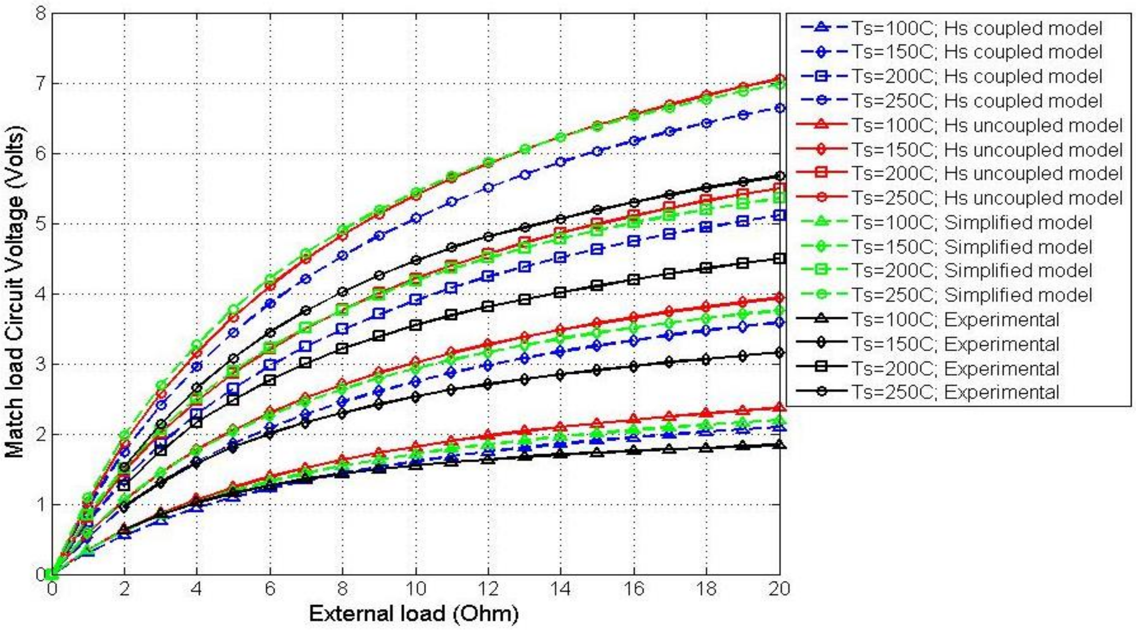

Figure 6-11 Voltage generation under different source temperature conditions and external load

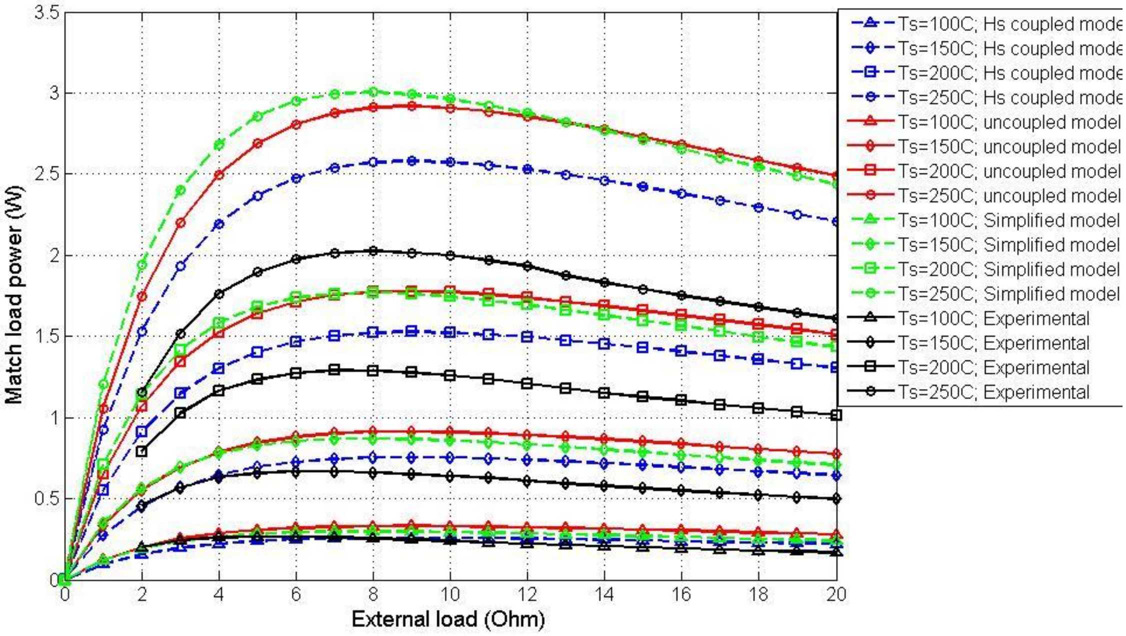

Figure 6-12 Power generation under different source temperature conditions and external load

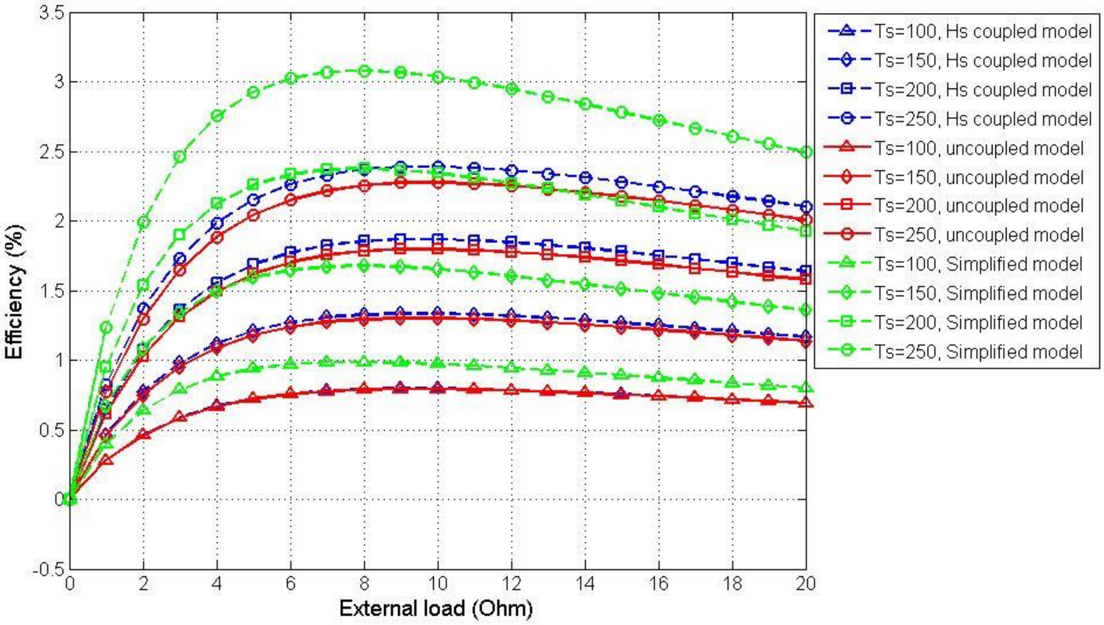

Figure 6-13 System efficiency under different source temperature conditions and external load

The impact of external loads on the system temperature profile is summarized in Figure 6-14. From Equations 29~30 and 33, one can find both hot side and cold side temperatures have dependency on external load, which further proves that thermal circuit and electricity circuit are coupled. As external load increases, the temperature gradient across the TEG increases, and the higher the source temperature is, the larger this influence will be. At source temperature of 250 ℃, the temperature difference due the external load variation from 0Ω to 20Ω is around 11.8°C according to coupled model, which account for 9.4% of the total temperature difference. The simplest model generates no change in temperature gradient because the energy conversion is not considered.

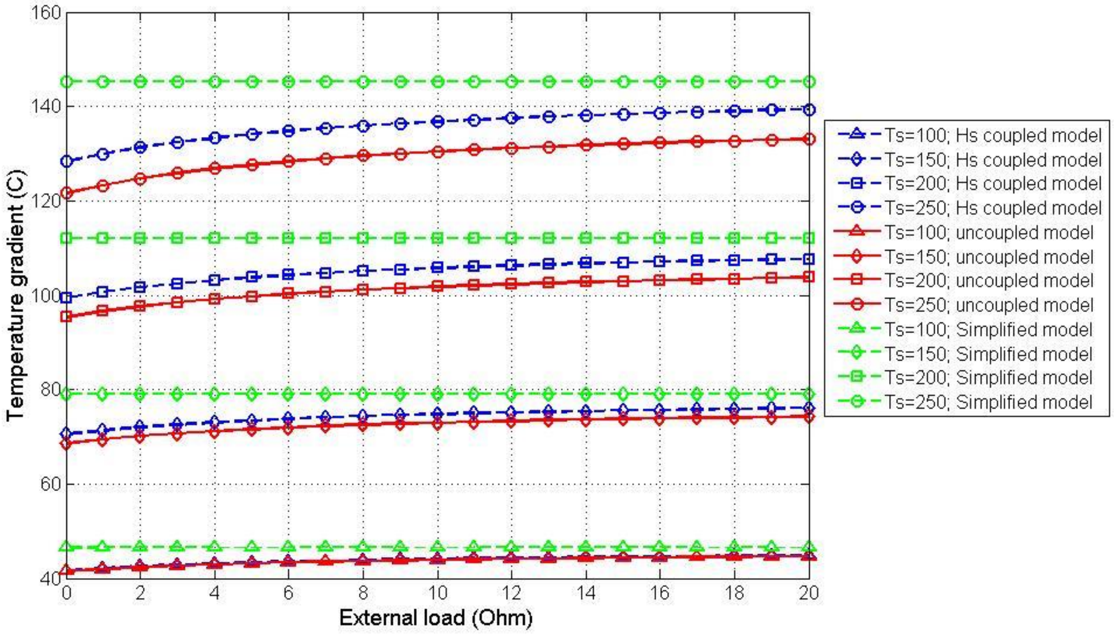

Figure 6-14 The coupling of external load on the system's temperature profile

6.4.3 Heat sink impact

As is talked in previous section, the heat sink dose have impact on the voltage and power generation. In this modeling, we assume the heat sink work in nature convection regime. In fact, the nature convection process will be governed by different convective heat transfer coefficients under different temperature profiles. Another temperature dependent effect, radiation heat transfer, is also considered in this modeling. The relation between heat sink equivalent thermal resistance, the corresponding impacts on system overall thermal resistance and source temperature is shown in Figure 6-15.

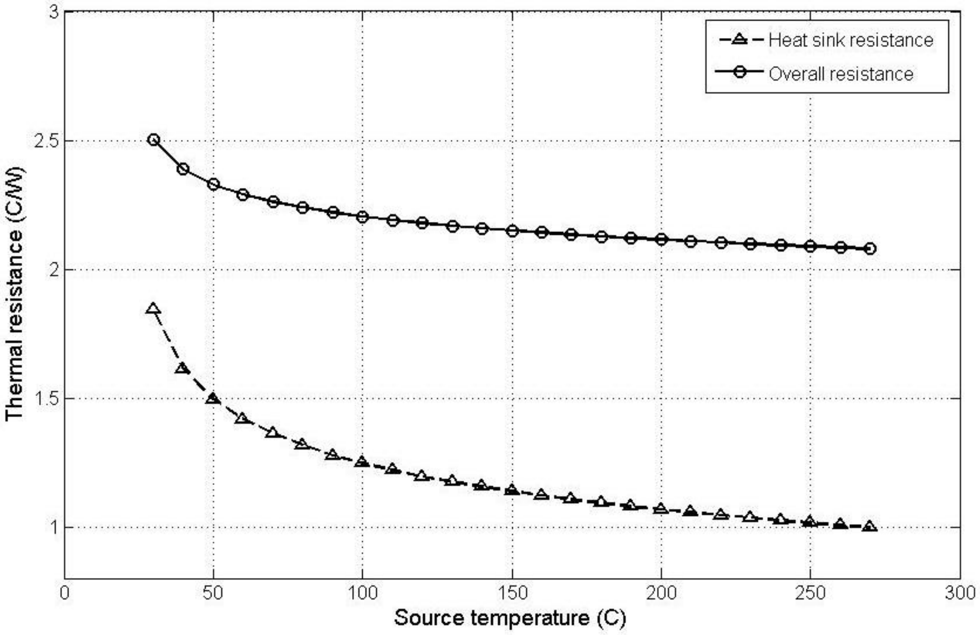

Figure 6-15 Thermal resistance change in system vs source temperature

As is shown in Figure 6-15, the thermal resistance of a single heat sink ranges from 1.84C/W to 0.99C/W in targeting temperature range. This leads a change of overall system thermal resistance around 16.8%.

6.4.4 Insulating materials impact on modeling

In all of the three modeling methods, the thermal resistance of the insulating material is considered in the heat transfer process. In most commercial thermoelectric modules, the P/N legs are often insulated with ceramic of polymers which have relatively good electrical and thermal resistivity. To examine the impact of insulating material thermal conductivity on the system outputs, an investigation of system outputs in terms of different thermal conductivity values was conducted. Both coupled and uncoupled models are employed in this study, since the experiment validation is impossible for a commercial module. The thermal conductivity of this insulation is selected from 0 to 2.0 W/(m·K) in this simulation. The measurements were taken under different temperature conditions from 100 ℃ to 250 ℃ and an external load of 7.8Ω.

Figure 6-16 provides the system outputs variation with respect to different conductivity values of insulating material (temperature difference (a), match load voltage (b), match load power (c), efficiency (d)). From (a), the effect of insulating material on the overall heat transfer process can be concluded: A lower thermal conductivity yields higher temperature difference across the module. This is valid since the insulating material is modeled as a thermal resistor parallel to the P/N legs. For T_s=250 ℃, when the thermal conductivity is 0, the corresponding temperature difference is 154.7 ℃ with heat sink coupled model, and 153.6 ℃ with uncoupled model. As thermal conductivity of material rises, the temperature difference reduced to 115.1 ℃ and 113.7 ℃ with both coupled and uncoupled models, respectively. From (b) to (d), the outputs under different material conductivity are analyzed, where we can see the match load voltage dropped from 5.68V to 4.23V with the heat sink coupled model in T_s=250 ℃ case. Similarly, the power anticipation dropped from 4.1W to 2.26W; while the efficiency reduced from 5.16% to 1.87%.

The power curves and efficiency curves witness more severe reduction than voltage curves and temperature profiles in the measured range, about 1.81 times and 2.76 times, respectively. These dramatic changes indicate the insulation material does have huge impact on both heat transfer and electrical outputs, so that the selection of insulating material is crucial. It should be noticed that even the variable is selected as the thermal conductivity of the material in this case, the parallel conductance K_{ce} (or resistance) could either be caused by radiation and natural convection heat transfer when there is no insulating materials applied.

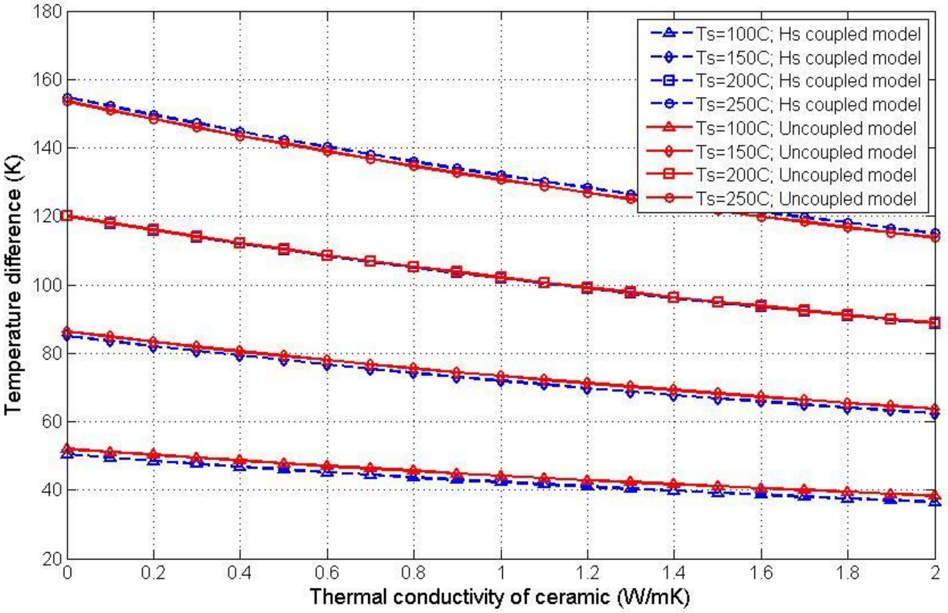
Ts=100C; Hs coupled model
Ts=150C; Hs coupled model
Ts=200C; Hs coupled model
Ts=250C; Hs coupled model
Ts=100C; Uncoupled model
Ts=150C; Uncoupled model
Ts=200C; Uncoupled model
Ts=250C; Uncoupled model
Temperature difference (K)
180
160
140
120
100
80
60
40
20
0
0.2
0.4
0.6
0.8
1
1.2
1.4
1.6
1.8
2
Thermal conductivity of ceramic (W/mK)

(a)

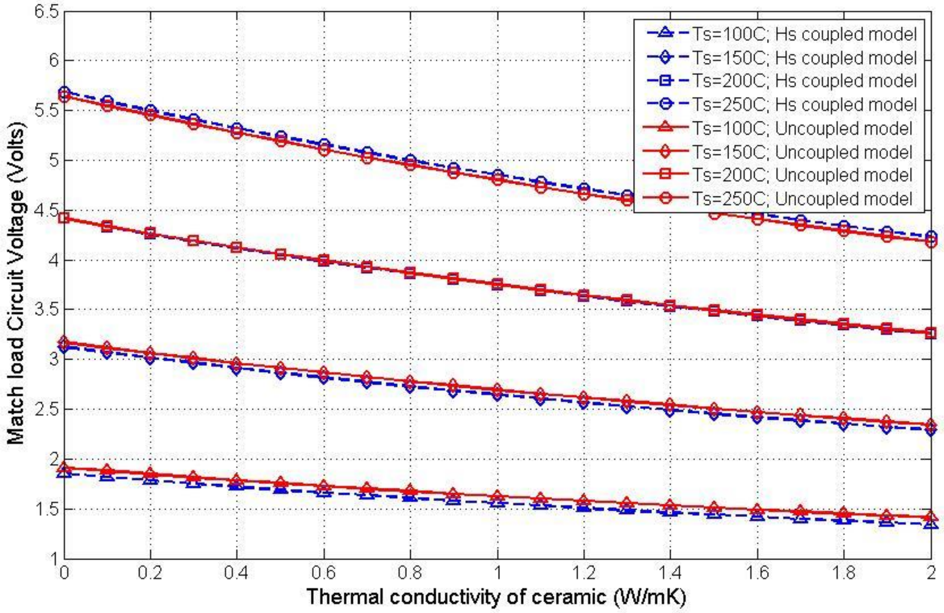
Ts=100C; Hs coupled model
Ts=150C; Hs coupled model
Ts=200C; Hs coupled model
Ts=250C; Hs coupled model
Ts=100C; Uncoupled model
Ts=150C; Uncoupled model
Ts=200C; Uncoupled model
Ts=250C; Uncoupled model
Match load Circuit Voltage (Volts)
6.5
6
5.5
5
4.5
4
3.5
3
2.5
2
1.5
1
0
0.2
0.4
0.6
0.8
1
1.2
1.4
1.6
1.8
2
Thermal conductivity of ceramic (W/mK)

(b)

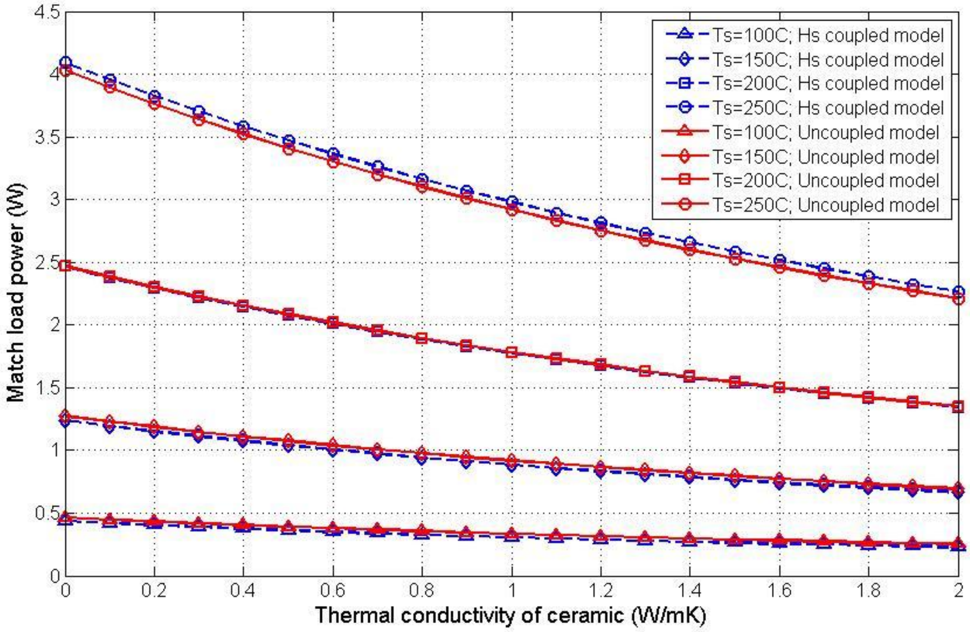

(c)

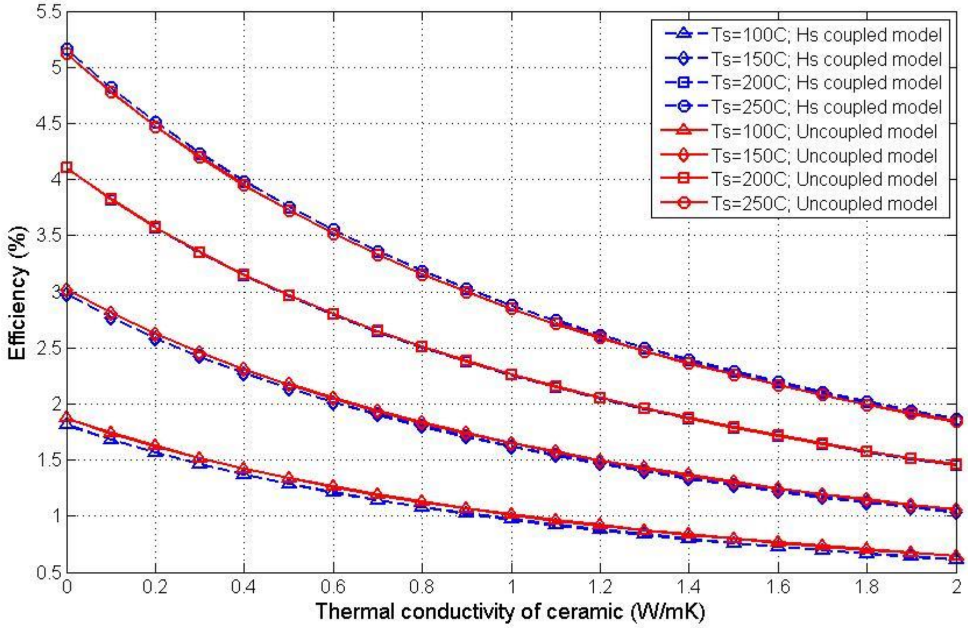

(d)

Figure 6-16 Insulating material's influence on System outputs: (a) temperature difference; (b) match load voltage; (c) match load power; (d) module efficiency

As stated above, the modeling of the TEG can be simplified to a five layer structure. The assumption underlies this modeling is that the insulating material is thermally parallel to the P/N junctions, which overlooks the conduction between P/N junctions and insulating materials in horizontal direction. This effect can be analyzed by comparing the open circuit voltage derived from analytical model and FEA model. Figure 6-17 summarizes the open circuit voltage collected within different methods.

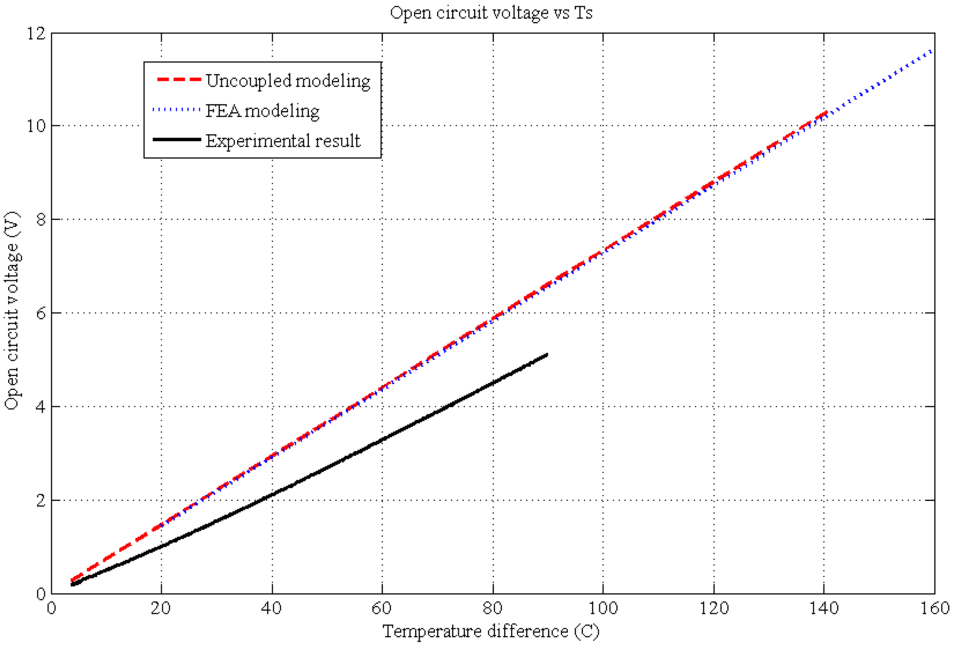

Figure 6-17 Comparison of open circuit voltages of different modeling and experimental results.

From this figure, the difference between analytical modeling result and FEA modeling is less than 1%, indicating that open circuit change due to the heat conduction from P/N junctions to insulating material is negligible. The reason for this phenomenon is primarily due to the temperature on both hot side surface and cold side surface of TEG is evenly distributed. Additionally, the thermal conductivity of both P/N junction and insulating material is between 1~2 W/(m·K). Since the temperature difference of TEG will not be impacted by the differences in three mathematical modeling, only uncoupled modeling result is plotted. The deviation of experimental results from modeling is majorly caused by the inaccuracy of Seebeck coefficient, which may come from the error in measurement or individual difference between TEG modules. This inaccuracy can also be proved from the comparison of match load voltage and power generation of both analytical and experimental results.

6.5 Comparison study of effectiveness of heat pipe

To verify the effectiveness of heat pipe in this work, a comparison study is carried out, in which an aluminum rod is used to substitute heat pipe in this assembly. This rod is made of 6061 aluminum which possess a considerably good thermal conductivity of 167W/m·K. This rod is fabricated with the same geometry and surface roughness as the heat pipe so that same thermal contact resistance can be assumed. The experiment was conducted under same conditions applied in the heat pipe assembly case.

The open circuit and match load voltage of both heat pipe-assisted system and baseline system is shown is Figure 6-18. It is obviously that heat pipe help increase open circuit voltage and match load voltage by 2.5 times simultaneously. This is because the extreme thermal conductivity of heat pipe. By utilizing phase change process, the thermal resistance within the same volume has been reduced more than 87 times, and the overall resistance reduced by more than 2.4 times, which enhances the heat flux and power generation by the same ratio and thus increases power generation by more than 5 times.

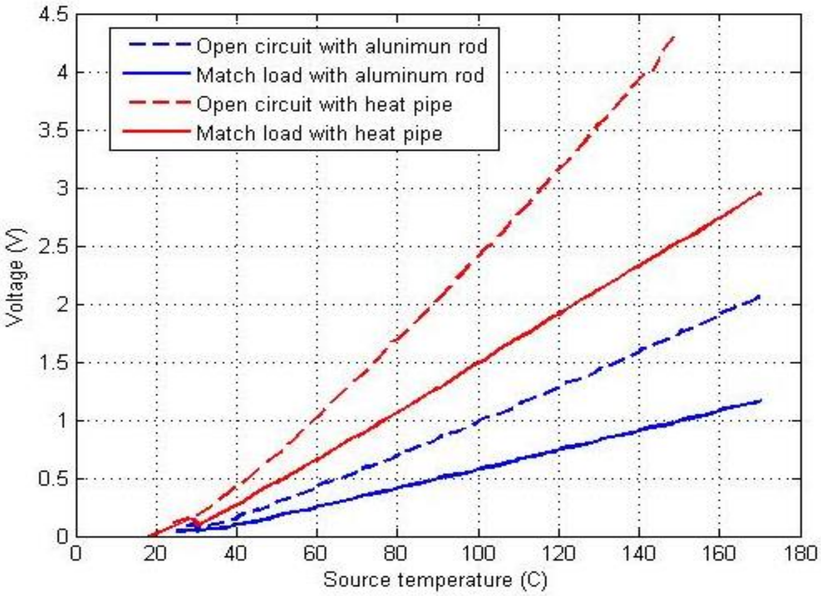

(a)

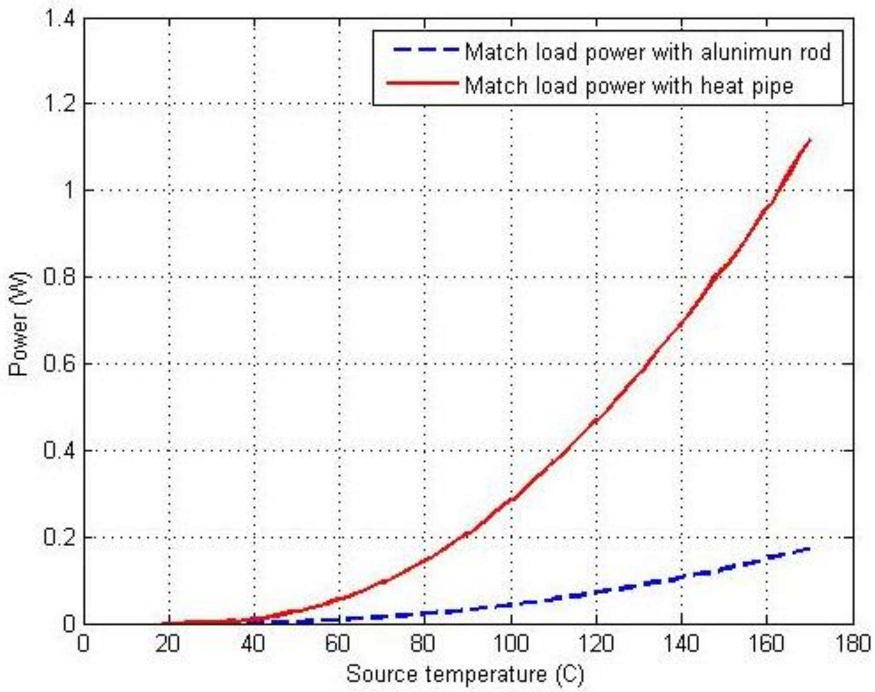

(b)

Figure 6-18 Comparison of Heat pipe-assisted system and baseline system in terms of voltage generation (a) and power generation (b)

6.6 Radiation based test results

In this post-radiation experiment, three irradiated TEMs were assembled individually with a new non-irradiated module using the previous test setup (irradiated samples on the left, non-irradiated samples on the right). Multiple times of heating processes were applied during measuring each irradiated samples, attempting to reduce systematic error in measurement. Same torque (0.42 Nm) were applied on the screws and same heating processes were used in different assembles to ensure the identical experimental conditions among the measurements of different samples. Representative results from multiple measurements for each irradiated sample assembly are selected and plotted in the Figure 6-19.

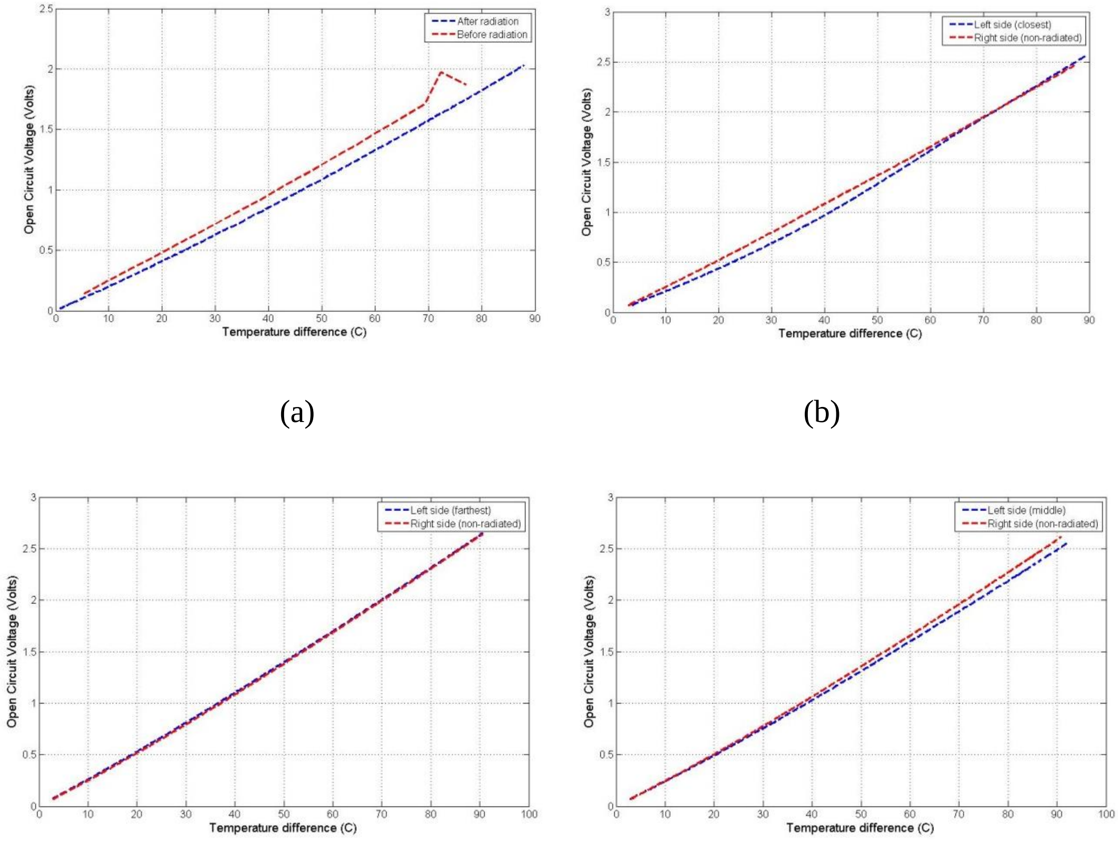

(a) (b)

(c) (d)

Figure 6-19 Post radiation experimental results: (a) Comparison of setup before with after radiation; (b) Comparison of closest module with non-radiated module; (c) Comparison of farthest module with non-radiated module; (d) Comparison of middle module with non-radiated module

As shown in Figure 6-18 (b)~(d), the discrepancies between left side samples and right side samples are negligible, which suggested gamma radiation caused little change in the thermoelectric related material properties in the experimented dosage range. The relatively large discrepancy in the Figure 6-18(a) might possibly be caused by change in the experimental conditions, in which the after radiation test was conducted with a new assembly. Thus, a conclusion could be made that the harvester system and the individual modules are unaffected by the exposure of gamma radiation.

6.7 Simulation for real application

Given the difficulty in setting up a real application based test, analytical simulations based on both models have been performed first. The steam parameters and pipe geometry used for this simulation are listed below:

Table 6-4 Input parameters for real application simulation

Parameter item	Target location	Value
Outer diameter of steam pipe (m) [67]	Both	0.5
Fluid velocity (m/s) [67]	Both	115
Mean temperature (℃) [67]	Primary loop (water)	317
	Secondary loop (steam)	292
Pressure (bar)	Primary loop	155
	Secondary loop	76
Thermal conductivity (W/m·K)	Primary loop	0.528
	Secondary loop	0.0652
Dynamic viscosity (Pa·S)	Primary loop	$8.174 \mathrm{x} 10^{-5}$
	Secondary loop	$1.925 \mathrm{x} 10^{-5}$
Specific heat capacity (KJ/kg·K)	Primary loop	6.001
	Secondary loop	5.591

As mentioned above in chapter 4, in the real case where heat pipe is inserted into the steam (water) pipe, the thermal resistance due to the convection at the outer surface of heat pipe evaporator needs to be calculated first. The equivalent thermal resistances are 0.573 and 0.309, in both steam and water coolant loops, which are large compare to the whole system.

The temperature range selected in this simulation is from 275 ℃ to 325 ℃, within both primary loop (295 ℃~325 ℃)and secondary loop (275 ℃~295 ℃) [52]. An external load of 7.9 Ω is used to calculate match load voltage and power. Figure 6-20 shows the variation of temperature profile (a), match load voltage (b) and match load power (c) with respect to different source temperatures. From 6-20 (a), we can see the hot side temperature dropped due to the extra thermal resistance at heat pipe evaporator side, comparing to the results in Figure 6-10. The maximum temperature difference yielded here is 151 ℃ at source temperature of 325 ℃ in primary loop, and 119.6 ℃ at source temperature of 295 ℃ in secondary loop. The voltages generated can reach at 5.55V and 4.5V, in primary loop and secondary loop, respectively. The maximal powers generated can reach at 3.9W and 2.45W, in primary loop and secondary loop, respectively.

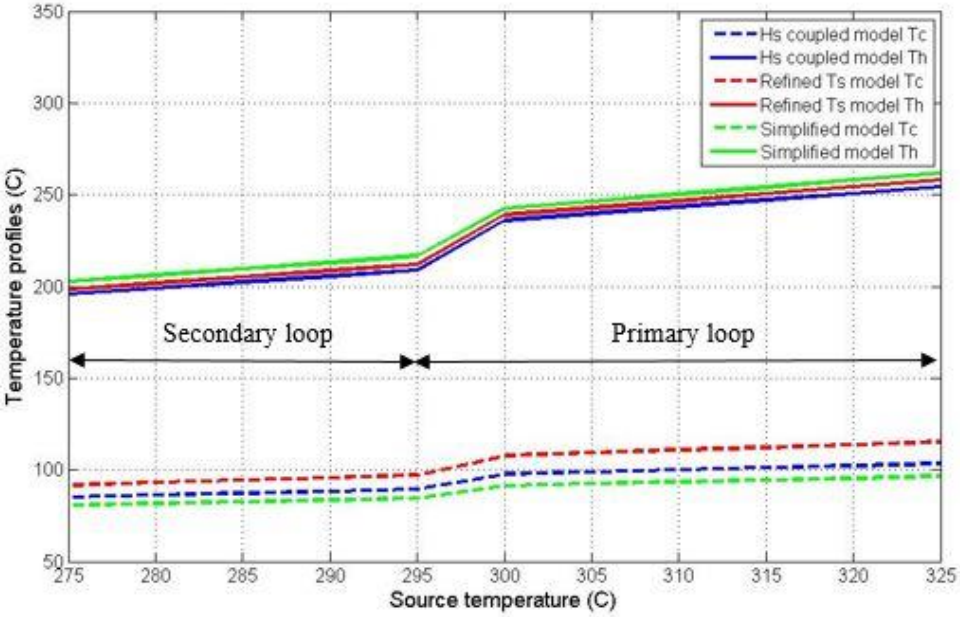

(a)

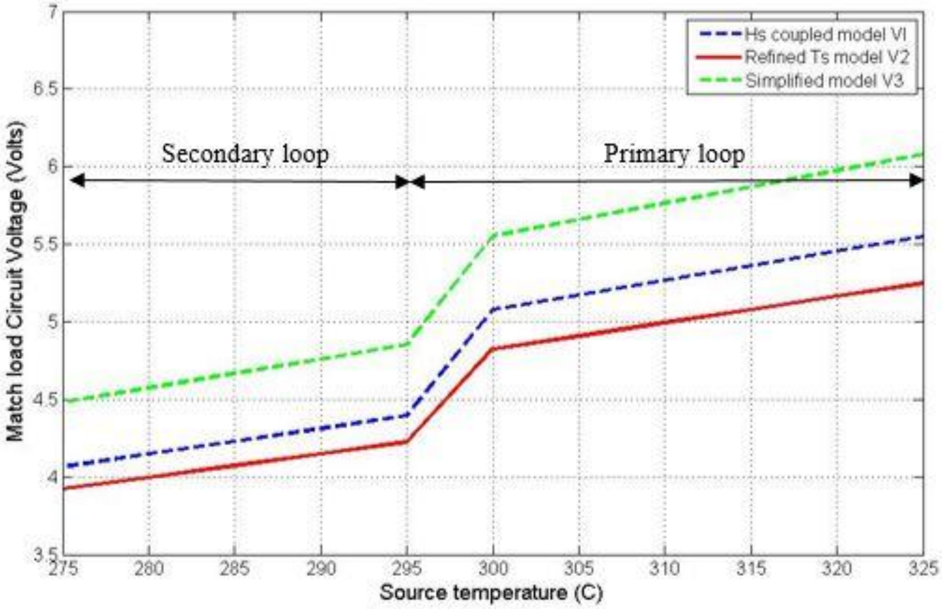

(b)

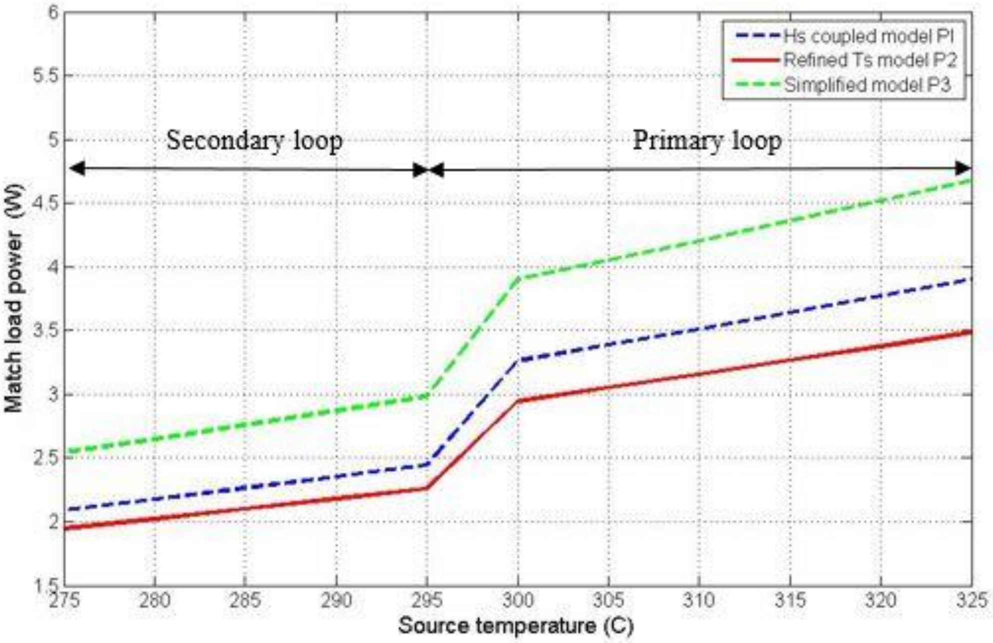

(c)

Figure 6-20 System outputs vs Source temperature in real application: (a) Temperature profile; (b) match load voltage; (c) match load power.

As is shown in the Figure 6-20, different fluid media impacts the system output significantly. Since water usually has less Reynolds number and Prandtl number than steam has, which results in an almost doubled external convective heat transfer coefficient (1082 W/m^{2}K in water, 583.6 W/m^{2}K in steam). Note that even the convective heat transfer coefficient is two orders higher than that in natural convection at cold side heat sink, the thermal resistance is still large due to the limited heat transfer area. The evaporator length of the heat pipe is selected to be 0.050m, which only leads to a 0.003 m^2 area. More modification can be done to further reduce thermal resistance at hot side, such as: 1) increasing heat pipe evaporator length (not suggested, blocking fluid); 2) adding heat sink at evaporator side (not suggested, blocking fluid); 3) Let evaporator side contact with steam/water pipe (lower resistance).

6.8 Optimization based on simulation study

6.8.1 Case 1 Number of pair optimization

As stated in previous section, the optimization towards current design could be done in several methods, among which adding extra pairs of modules at each side of system is the easiest one. Ideally, adding more thermoelectric modules leads to larger power generation. However, due to the existence of hot side and cold side thermal resistance, the power generation cannot be enhanced infinitely through adding thermoelectric modules. A simulation was carried using the current designed parameters of module, hot, cold side structure. The source temperature is assumed to be 250 ℃; the ambient temperature is fixed at 25 ℃. During the simulation, the effect of reducing spreading resistance caused by attaching more modules with the heat sink is neglected, and thus the thermal resistances at both hot and cold side can be treated as constants.

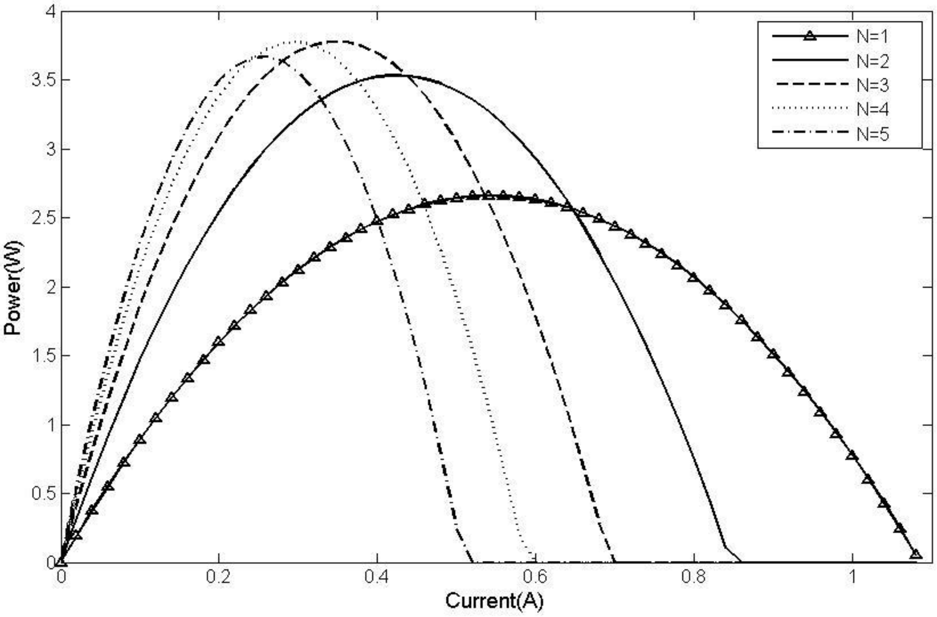

Figure 6-21 Effect of module pair number on the Power vs Current.

Figure 6-21 shows the influence of thermoelectric modules pair number on the system power generation. As the pair number increases, the peak power generation reaches to maximum at N=3, and then gradually decreases. The improvement of adding the second pair to the original 1-pair system is considerable; while adding the third one only achieved very limited improvement on power generation; adding the forth pair even degenerates the power output. In fact, by adding more modules, the overall thermal resistance at the modules reduces because of the parallel thermal circuit configuration, which leads to a decrement in temperature difference which counterbalances the increased voltage. At each certain pair number, the curve rises with the current till the peak and then falls back. The curves shifts to low current range gradually as N increases, primarily because the internal electrical resistance increases linearly with module pair number. For every curve, the maximum power is achieved at the match load situation.

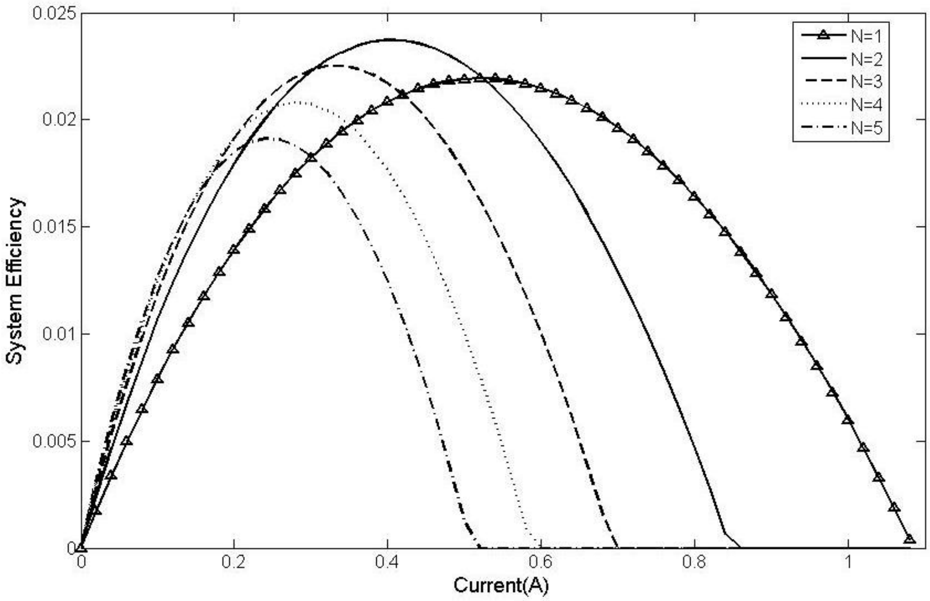

Figure 6-22 Effect of module pair number on efficiency vs current.

Figure 6-22 depicts similar trend as output power. Note that the maximum efficiency is achieved only using two pairs of thermoelectric, which further proved the maximum efficiency and power output cannot be achieved simultaneously with this design. The increment through adding second pair is small, only about 0.2%. Thus, from the prospective of efficiency, using two modules (1 pair) is already in relatively high efficiency. Further improvement for current design can be achieved in the future by adding modules depending on the user’s will.

6.8.2 Case 2 K_H and K_c values and ratio

The system performance can also be improved by tuning the values and ratios of K_H and K_c rather than changing the numbers of modules. This can be achieved by selecting different kind of heat sink, heat pipe, and applied different contact thermal resistance. In this study, we assume the overall thermal resistance of the non-module part is a fixed value, in which way the optimum ratio between K_H and K_c can be determined. The summed thermal resistance of non-module part is 10; and all the other material properties involved in this simulation remain their previous values. The current is selected as the main variable, so that the difference between thermal resistance selection can be reflected from the $I - P$ and $I - \eta$ models.

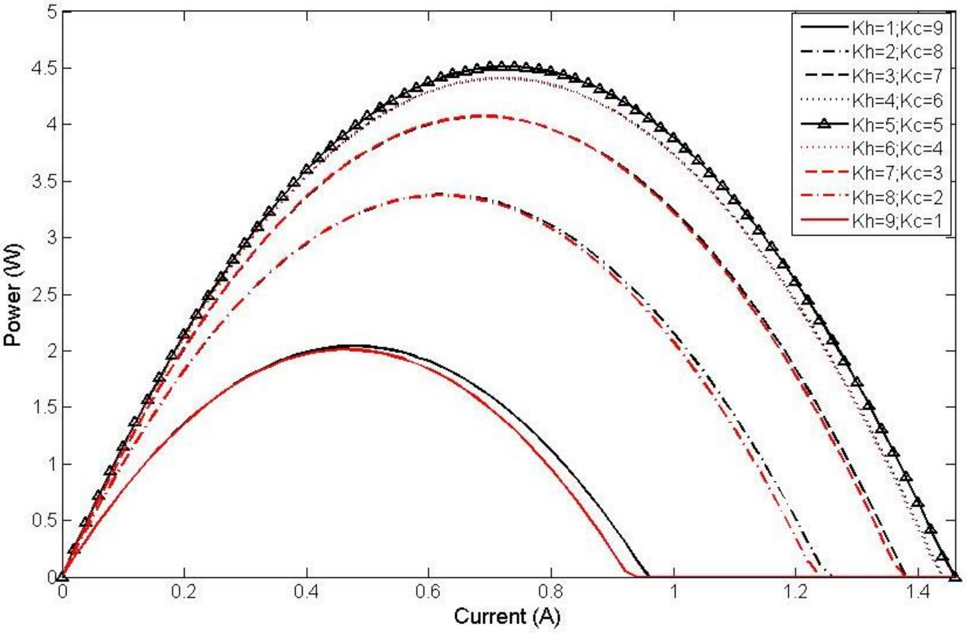

Figure 6-23 Effect of K_H and K_c on the Power vs Current

Figure 6-23 shows the Effect of non-module heat transfer part on the power generation. Within the same summed thermal resistance, large discrepancies exist among the power generation in different thermal resistance combinations. The more evenly distributed thermal resistance on both sides, the higher power generation will be yielded. An ratio of 9 or 1/9 yields around 2W of power output; while a moderate change in K_H from 2 to 8 (or K_C from 8 to 2) yields an significant improvement at about 1.5W. As ratio approaches to 1, the improvement increases slowly. Note that for each K_H and K_C, the reversibility is indicated from the overlaps, which suggested that K_H and K_C have same level of impact on the heat transfer and power generation process. The tiny difference between the curves from every "group" is primarily due to the energy conversion process which induces the difference between inflow and outflow of heat of a module. In fact, since the heat flow in the cold side is 2-3% lower than that in the hot side, leads to the conclusion that the cold side has slightly lower impact on the overall power generation.

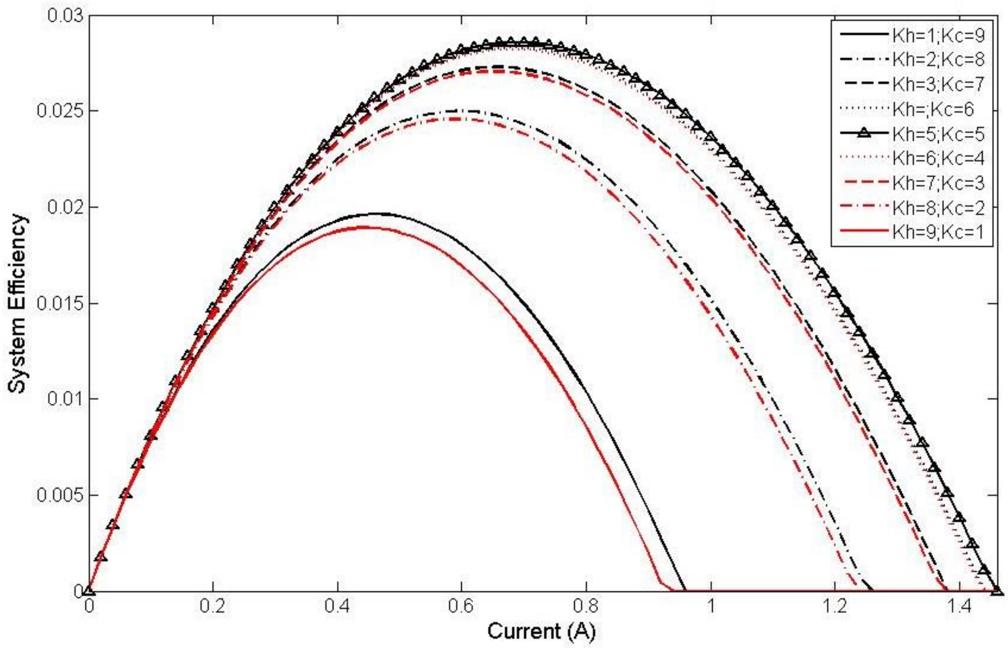

Figure 6-24 Effect of K_H and K_c on the Efficiency vs Current

Figure 6-24 suggests a similar result: the more even the thermal resistance are, the higher efficiency can be achieved.

7 Radiation impact analysis and mitigation

7.1 General radiation influences on electronics

7.1.1 Radiation impacts on passive components

Radiation's influence on the passive electrical components is in fact material and fabrication method dependent [69]. Generally, radiation does not impact on ceramics, glasses, and metal parts, but do have negative influence on some oxides and organic materials like polymers. Therefore, electrical components made of different materials have distinct radiation tolerance.

A good example is resistor. Most of the resistors are very tolerant to radiation except oxide film resistors has a low tolerance as 10Gy, and high resistance resistors tends to more sensitive to radiation. For capacitors, the dielectric materials determine their tolerance, since dielectric damage may change capacitance, leakage current and breakdown voltage. Resistors made of electrolyte are the most sensitive to radiation as they fail at 100Gy. Inductors' radiation threshold depends on former and insulator material since they are more sensitive than the metal wires. Conducting metal layers on circuit boards are immune to radiation, but the substrate may be damaged if it is made of silicon or polymer.

7.1.2 Radiation impacts on semiconductors

Radiation impacts on semiconductors mainly by two fundamental mechanisms: ionization damage and displacement damage [83].

Ionization damage: when energy deposited in a semiconductor or in insulating layers, chiefly SiO2, frees charge carriers (electron-hole pairs), which diffuse or drift to other locations where they may get trapped, leading to unintended concentrations of charge and parasitic fields. This kind of damage is the primary effect of exposure to X- and γ-rays and charged particles. It affects mainly devices based on surface conduction.

Displacement damage: incident radiation knocks out atoms from their lattice site, the resulting defects altering the electronic properties of the crystal. This is the primary mechanism of device degradation for high energy neutron irradiation, although a certain amount of atomic displacement may be determined by charged particles (including Compton secondary electrons). Displacement damage mainly affects devices based on bulk conduction.

With these two mechanisms stated above, effects of radiation in semiconductor devices can be summarized in two ways: Total ionizing dose (TID) effects which due to the progressive build-up of trapped charge in insulating layers or at the Si/SiO2 interface or of defects in the bulk of the devices. Single Event Effects (SEE) will be talked in section 7.4.

7.2 Gamma radiation influence

Depending on its energy, gamma ray photons interact with matter in various ways, among which photoelectric effect, the Compton Effect and electron-positron pair production are the three main types [84]. Photoelectric effect occurs when the energy of photon is low. In this process, a gamma photon interacts with an atom leading to the ejection of an electron from the atom after the energy of the gamma photon carried transport to electron entirely. As the energy carried by the photons increases, the probability for Campton effect and pair production are increased. In Campton effect, photon transports a portion of its energy to electron, causeing the ejection of electron and incident gamma ray with higher wavelength. In pair production, a gamma photon transforms into matter near the nucleus of an absorber atom during the form of an electron-positron pair. The high energy free electron generated during the ionizing damage spans to forbidden gap and create electron-hole pair, which leads to the increment in electrical conductivity of material, even non-conducting material.

The ionization damage is primarily due to the trapping of charge in silicon and secondarily due to the anomalies [85]. The pairs created in semiconductors, say silicon and silica, can diffuse or recombine depending on electrical field. Part of pairs recombine with other carries. However, due to the difference in mobility in silicon dioxide, electrons of the rest pairs may leave silica during circuit operation and only a small part of holes can move to silicon as well. Therefore, a charge is built up on the interface of silicon and silicon dioxide. The generation of charge on interface impacts mainly on MOS devices. For example, the operation of MOSEFT can be effected when radiation-induced trapped charge is built up in the gate oxide, as shown in Figure 7-1. It mainly causes a shift in the threshold voltage, which is the voltage needed to be applied to activate device. As the shift increases to a level that the threshold voltage reduce to zero, the device cannot be turned off and is said to have failed by going depletion mode [86].

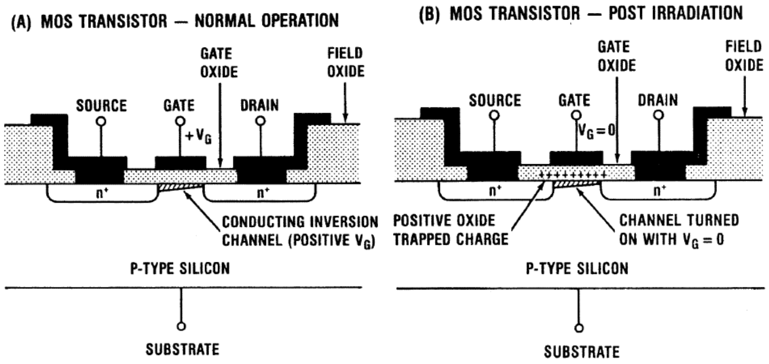

Figure 7-1 Schematic of n-channel MOSFET illustrating radiation-induced charging of the gate oxide: (a) normal operation and (b) post-irradiation [86].

Other impacts of ionizing radiation include [85]: decrease of transconductance, increase of leakage current, deterioration of noise parameters, etc.

7.3 Neutron radiation influence

Neutrons are matter particles, thus, the main effect of neutron influence on target atoms is collision which leads to displacement defects. Depending on kinetic energy of the neutron, the interaction of neutron and matter has two ways: elastic scattering for high energy neutrons and capturing effect for low energy neutrons [85]. The resulting displacement damage types are various: vacancy, divacancy, interstitial and Frenkel defects. Some of the primary defects are unstable and can be recovered, but some may cause permanent damage that charge trapping centres and increase material electrical resistivity [87].

Given the description of displacement effect in Chapter 2.1, displacement effect cast shadows particularly on bipolar transistors, primarily because the recombination centres short the lifetime of minority carries [85]. In fact, bipolar transistors exposed to radiation operates in a narrow base region. Therefore, high frequency tends to be more radiation resistive. Another parameter that might be influenced is collector based leakage current. For MOS transistors, since their operations are not based on lifetime of minority carries, they are more resistive to displacement damage than bipolar transistors. However, they are vulnerable to ionizing radiation. Even the neutrons are neutral, they are capable of producing secondary ionizing particles with lower energy during their interaction with atoms, e.g. gamma rays. Thus, MOS devices can still be influenced by neutron radiation. Generally, bipolar transistors will be influenced by neutron radiation at dose level of 10^{11}n/cm^2, while MOS transistors aren't affected until 10^{15}n/cm^2 [87].

Makowski summarized the interaction and effects of gamma and neutron radiation on semiconductors [85].

Table 7-1 Summary of interaction and effects of gamma and neutron radiation

Radiation type	Energy level	Main interaction	Primary effect	Secondary effect
Gamma	High	Pair production	Ionizing effect	Displacement effect
	Medium	Campton effect		
	Low	Photoelectric effect		
Neutron	High	Elastic scattering	Displacement effect	Ionizing effect
	Low	Capture		

7.4 Single Event Effects (SEE)

Apart from the ionizing and displacement damage, gamma and neutron radiation can cause the Single event effects. In most cases, they affect only digital devices, so they were not studied extensively until recently. Single event effects are due to a single particle crossing the sensitive area of a device or circuit. Part of these events are classified as soft, or nondestructive, since they trigger the loss of information rather than any physical damage, such as a bit flip in a memory array. The other events are termed hard, or destructive, because they do induce permanent damage, such as the gate oxide rupture following the strike of a heavy ion [85].

The main nondestructive effects and destructive effects can be concluded as following [88]:

Nondestructive effects:

- Single event upset (SEU): change of device state induced by an energetic particle, mainly in digital devices, e.g. the corruption of a single bit in a memory array,
- Single event transient (SET): a disturbed transient signal induced by an ionizing particle in a combinatorial or analog part of a circuit.

Destructive effects:

- Single event latch-up (SEL): the activation of parasitic bipolar PNPN (or NPNP) structures in bulk CMOS devices, leading to a destructive sudden increase of the supply current and overheat.
- Single event burnout (SEB): burnout of a power MOS device, when high energy particle induce high drain-source voltage higher than breakdown voltage.
- Single event gate rupture (SEGR): rupture of gate oxide occurring especially in power MOSFETs, when a heavy ion hits the gate region while a high voltage is applied to the gat.

7.5 Radiation mitigation

Radiation mitigation techniques are of great importance in both radiation protection research and industrial application. Depending on the methods implemented in different phases. The radiation mitigation techniques can be divided into two classes: 1) Methods implemented during the design and fabrication process. 2) Shielding for the most critical components.

7.5.1 Radiation hardening design

Methods can be taken to enhance radiation tolerance in both design and fabrication processes from material selection or fabrication method adjustment. To achieve better tolerance from designing modification, one can minimize the growing of charge and threshold voltage shift. Generally, the oxide layer should be designed as thin as possible so that trapped holes can be annihilated through the tunneling effect of electrons [87]. Besides, removing impurity in the fabrication of gate oxide’s material also helps to improve tolerance to TID. Adding extra guard rings also allow to modify the transconductance of parasitic field oxide transistors [85]. Markowski also summarized the methods to improve tolerance of circuits towards SEE. On the design of IC side, adding storage cells or sense amplifiers are useful to reduce SEE induced error.

However, considering the difficulty in redesign and fabrication and special usage in this project, radiation shielding for exist circuits that works well in non-radiation environment is more cost effective.

7.5.2 Radiation shielding

Study of absorption of gamma and neutron radiations using shielding materials has became an important subject in radiation physics. Radiation shielding is based on the ability of materials to reduce a wave's or ray's effect by blocking or bouncing particles through a barrier material. Gamma radiation is attenuated through photoelectric, scattering, or pair production. Neutron radiation can be tuned through a combination of elastic and inelastic scattering.

7.5.2.1 Gamma radiation shielding

Theoretically, the attenuation of gamma radiation can be expressed as following [89]:

$$I = I_0 e^{-\mu\rho t} \ or \ I = I_0 e^{-\mu d} \tag{68}$$

where I and I_0 are intensity of gamma radiation and initial intensity before shielding; μ is the mass absorption coefficient for the shielding material; d is the "thickness (g/cm 2)" and t is physical thickness. Regardless of thickness, attenuation is related to the density of material. Therefore, higher Z (atomic number) material leads to better performance. Shielding of gamma radiation primarily involves the three main types of interaction of gamma radiation with matter stated above.

Lead is particularly well-suited for gamma radiation shielding and has been used widely in industry for its readily availability and cost effectivity. Recently, other materials have been investigated with their radiation absorption coefficient such as concrete, semiconductor, polymer, Lipowitz alloy, colemanite, etc.

7.5.2.2 Neutron radiation shielding

Shielding for neutrons is not as easy as for gamma-ray since it's heavier and more energy dependent [85]. The designing of neutron radiation consists of following steps [87]:

1. Slowing down fast high-energy neutrons.
2. Absorbing slowed down neutrons.
3. Attenuating the incident gamma radiation created during the activation.

To slow down the fast high-energy neutrons, energy lost during the collision of neutrons and material atoms should be maximized. In another way, according to conservation of momentum, neutrons should collide with particles having closed atomic mass, e.g. proton (hydrogen nuclei). Thus, hydrocarbons are suitable for this purpose. To absorb the slowed down thermal neutrons, materials should have higher probability to form cross sections to interact with neutrons. Boron, cadmium and mixed materials such as borated concrete and polyethylene have high absorption cross sections are good options [90]. However, low density materials can emit gamma rays when interacting with neutrons, therefore it is more effective to incorporate both high and low atomic number elements. The low-density material can disperse the neutrons through elastic scattering, while the high-density segments block the subsequent gamma rays with inelastic scattering.

Abundant patents have been developed for the shielding of electronic devices with different materials and design concepts. Featherby invented an electronic device shielding and coating method with hardened material to protect target objects from cosmic radiation [91]. Dlugokecki made a design on the implementing radiation shielding to a plastic package for integrated circuits [92]. Strobel refined the design with partial shielding for circuits, which is particularly useful in places where radiation source is nearby and radiation from other directions can be omit safely [93].

In this project, given that the radiation is much intense and complex in a nuclear power plant, an incorporated design for both gamma and neutron radiation design is needed. Therefore, structure with multilayers in 3 directions are suggested, basically, three layers are needed: the outer layer with low-Z material to slow down neutrons; the middle layer with good absorption cross section to absorb neutrons; the inner layer with high Z material to absorb gamma radiation and the incident radiation produced in neutron interaction. Additional layers or structure such as mechanical supporting, sealing layer might be added depends on the need.

8 Conclusion and Future work

In this work, a thermoelectric generator aimed at harvesting energy from nuclear power plant pipelines to power the sensing nodes has been constructed. A system level design of self-powered sensor package and a detailed design of thermoelectric part have been presented. The feasibility of harvesting energy on high temperature pipes was studied based on three analytical modeling techniques and FEA simulations. A prototype has been fabricated and tested in both lab-based condition and radiation based condition. 2.25W of energy was generated within source temperature of 246 ℃ and temperature difference of 128 ℃ in the lab-based condition, which is sufficient to power all the electronics. The proposed model accurately estimate the voltage, power generation with error less than 1.5% in low temperature range, and about 10% in high temperature range. A comparison study has been carried out to analyze the effectiveness of heat pipe in this design, with a result showing the heat pipe significantly improved the system voltage output by 2.5 times and power output by more than 5 times. The effectiveness of power management circuits and wireless communication circuits were tested. The gamma radiation's influences on thermoelectric harvester and electronics and radiation mitigation techniques have been studied extensively through experiments and literature review. According to the experimental results, the harvester exhibits sustainability in the radiative condition with similar gamma dosage as in the real application for 40 years. A simulation based on the proved models has then been carried out to estimate the system performance in the real pipeline application, and yields a maximum power of 3.9W. Finally, an optimization has been carried towards the current design, in which the effect of modules number, thermal resistance at hot end and cold end on system output were studied and significant improvements in power and efficiency were achieved.

A 2nd generation device targeted on harvesting energy at higher temperature locations has now been proposed. A 2nd phase radiation test is now in progress with the help from Westinghouse. The signal processing circuit is now in developing progress which could analyze the signal from the langasite sensor. In the future, following recommended tasks can be accomplished to further extend the application scope and enhance the system performance:

1). It should be noticed that the errors in both modeling and experiments (especially the resistor box) still exist in high temperature range. Therefore, more experiments with more accurate equipment need to be conducted.

2). Follow the optimization methods proposed in section 6.6 to further enhance the performance of thermoelectric part.

3). Develop new versions of thermoelectric harvesters that are sustainable to higher temperature range and higher radiation condition with smaller size.

4). Investigate the vibrational energy harvesting feasibility and build a multi-source energy harvester by combining with existing one.

5). Conduct in-situ test on thermal electric energy harvester and circuits in both gamma and neutron radiation conditions.

6). Construct an overall integrated package with electrical parts and sensors and test their performance in a real application.

References

[1] Priya, Shashank, and Daniel J. Inman, eds. *Energy harvesting technologies*. Vol. 21. New York: Springer, 2009.

[2] Paradiso, Joseph, and Thad Starner. "Energy scavenging for mobile and wireless electronics." *Pervasive Computing*, IEEE 4, no. 1 (2005): 18-27.

[3] Jabbar, Hamid, Young S. Song, and Taikyeong Ted Jeong. "RF energy harvesting system and circuits for charging of mobile devices." Consumer Electronics, *IEEE Transactions* on 56, no. 1 (2010): 247-253.

[4] G. J. Snyder and T. S. Ursell, "Thermoelectric efficiency and compatibility", *Physical review letters*, vol. 91, p. 148301, 2003.

[5] Snyder, G. Jeffrey, and Eric S. Toberer. "Complex thermoelectric materials". *Nature materials* 7, no. 2 (2008): 105-114.

[6] G. S. Nolas, J. Sharp, and H. Goldsmid, Thermoelectrics: *Basic Principles and New Materials Developments*, Springer, New York, 2001.

[7] Liu, Weishu, Xiao Yan, Gang Chen, and Zhifeng Ren. "Recent advances in thermoelectric nanocomposites." *Nano Energy* 1, no. 1 (2012): 42-56.

[8] G. Slack, in CRC *Handbook of Thermoelectrics*, ed. D. M. Rowe, CRC Press, Boca Raton, 1995, pp. 407–440.

[9] Minnich, AJl, M. S. Dresselhaus, Z. F. Ren, and G. Chen. "Bulk nanostructured thermoelectric materials: current research and future prospects." *Energy & Environmental Science* 2, no. 5 (2009): 466-479.

[10] Hicks, L. D., and M. S. Dresselhaus. "Thermoelectric figure of merit of a one-dimensional conductor." *Physical review B* 47, no. 24 (1993): 16631.

[11] Hicks, L. D., T. C. Harman, X. Sun, and M. S. Dresselhaus. "Experimental study of the effect of quantum-well structures on the thermoelectric figure of merit." *Physical Review B* 53, no. 16 (1996): R10493.

[12] Alam, Hilaal, and Seeram Ramakrishna. "A review on the enhancement of figure of merit from bulk to nano-thermoelectric materials." *Nano Energy* 2, no. 2 (2013): 190-212.

[13] Venkatasubramanian, Rama, Edward Siivola, Thomas Colpitts, and Brooks O'quinn. "Thin-film thermoelectric devices with high room-temperature figures of merit." *Nature* 413, no. 6856 (2001): 597-602.

[14] Boukai, Akram I., Yuri Bunimovich, Jamil Tahir-Kheli, Jen-Kan Yu, William A. Goddard Iii, and James R. Heath. "Silicon nanowires as efficient thermoelectric materials." *Nature* 451, no. 7175 (2008): 168-171.

[15] Harman, T. C., P. J. Taylor, D. L. Spears, and M. P. Walsh. "Thermoelectric quantum-dot superlattices with high ZT." *Journal of Electronic Materials* 29, no. 1 (2000): L1-L2.

[16] Goldsmid, H. J., and G. S. Nolas. "A review of the new thermoelectric materials." In Thermoelectrics, 2001. *Proceedings ICT 2001. XX International Conference* on, pp. 1-6. IEEE, 2001.

[17] Qiu, P. F., J. Yang, R. H. Liu, X. Shi, X. Y. Huang, G. J. Snyder, W. Zhang, and L. D. Chen. "High-temperature electrical and thermal transport properties of fully filled skutterudites RFe4Sb12 (R= Ca, Sr, Ba, La, Ce, Pr, Nd, Eu, and Yb)." *Journal of Applied Physics* 109, no. 6 (2011): 063713.

[18] Shi, X., H. Kong, C-P. Li, C. Uher, J. Yang, J. R. Salvador, H. Wang, L. Chen, and W. Zhang. "Low thermal conductivity and high thermoelectric figure of merit in n-type BaxYbyCo4Sb12 double-filled skutterudites." *Applied Physics Letters* 92, no. 18 (2008): 182101.

[19] Saramat, Ali, Göran Svensson, A. E. C. Palmqvist, Christian Stiewe, E. Mueller, Dieter Platzek, S. G. K. Williams, D. M. Rowe, J. D. Bryan, and G. D. Stucky. "Large thermoelectric figure of merit at high temperature in Czochralski-grown clathrate Ba8Ga16Ge30." *Journal of Applied Physics* 99, no. 2 (2006): 023708.

[20] Yu, Cui, Tie-Jun Zhu, Rui-Zhi Shi, Yun Zhang, Xin-Bing Zhao, and Jian He. "High-performance half-Heusler thermoelectric materials Hf 1− x ZrxNiSn 1− ySby prepared by levitation melting and spark plasma sintering." *Acta Materialia* 57, no. 9 (2009): 2757-2764.

[21] Fu, Gaosheng, Lei Zuo, Jie Chen, Ming Lu, and Liangyao Yu. "Thermoelectric properties of DC-sputtered filled skutterudite thin film." *Journal of Applied Physics* 117, no. 12 (2015): 125304.

[22] Xie, Jin, Chengkuo Lee, Ming-Fang Wang, Youhe Liu, and Hanhua Feng. "Characterization of heavily doped polysilicon films for CMOS-MEMS thermoelectric power generators." *Journal of Micromechanics and Microengineering* 19, no. 12 (2009): 125029.

[23] Kwon, Sung-Do, Byeong-kwon Ju, Seok-Jin Yoon, and Jin-Sang Kim. "Fabrication of bismuth telluride-based alloy thin film thermoelectric devices grown by metal organic chemical vapor deposition." *Journal of electronic materials* 38, no. 7 (2009): 920-924.

[24] Xie, Jin, Chengkuo Lee, and Hanhua Feng. "Design, fabrication, and characterization of CMOS MEMS-based thermoelectric power generators." *Microelectromechanical Systems, Journal* of 19, no. 2 (2010): 317-324.

[25] Riffat, Saffa B., and Xiaoli Ma. "Thermoelectrics: a review of present and potential applications." *Applied Thermal Engineering* 23, no. 8 (2003): 913-935.

[26] Bahk, Je-Hyeong, Haiyu Fang, Kazuaki Yazawa, and Ali Shakouri. "Flexible thermoelectric materials and device optimization for wearable energy harvesting." *Journal of Materials Chemistry C* 3, no. 40 (2015): 10362-10374.

[27] Amatya, R., and R. J. Ram. "Solar thermoelectric generator for micropower applications." *Journal of electronic materials* 39, no. 9 (2010): 1735-1740.

[28] Longtin, Jon P., Lei Zuo, David Hwang, Gaosheng Fu, Mahder Tewolde, Yikai Chen, and Sanjay Sampath. "Fabrication of Thermoelectric Devices Using Thermal Spray: Application to Vehicle Exhaust Systems." *Journal of thermal spray technology* 22, no. 5 (2013): 577-587.

[29] "Nuclear Reactor Types" The Institute of Engineering and Technology 2008.

[30] Neild, A. Bayne. *Portable thermoelectric generators*. No. 630019. SAE Technical Paper, 1963.

[31] Haidar, Jihad G., and Jamil Ghojel. "Waste heat recovery from the exhaust of low-power diesel engine using thermoelectric generators." In Thermoelectrics, 2001. *Proceedings ICT 2001. XX International Conference* on, pp. 413-418. IEEE, 2001.

[32] Ikoma, K., M. Munekiyo, K. Furuya, M. A. K. M. Kobayashi, T. A. I. T. Izumi, and K. A. S. K. Shinohara. "Thermoelectric module and generator for gasoline engine vehicles." In Thermoelectrics, 1998. *Proceedings ICT 98. XVII International Conference* on, pp. 464-467. IEEE, 1998.

[33] Thacher, E. F., B. T. Helenbrook, M. A. Karri, and Clayton J. Richter. "Testing of an automobile exhaust thermoelectric generator in a light truck." *Proceedings of the Institution of Mechanical Engineers, Part D: Journal of Automobile Engineering* 221, no. 1 (2007): 95-107.

[34] Hsu, Cheng-Ting, Da-Jeng Yao, Ke-Jyun Ye, and Ben Yu. "Renewable energy of waste heat recovery system for automobiles." *Journal of Renewable and Sustainable Energy* 2, no. 1 (2010): 013105.

[35] Hsu, Cheng-Ting, Gia-Yeh Huang, Hsu-Shen Chu, Ben Yu, and Da-Jeng Yao. "Experiments and simulations on low-temperature waste heat harvesting system by thermoelectric power generators." *Applied Energy* 88, no. 4 (2011): 1291-1297.

[36] Goncalves, L. M., Jorge Martins, Joaquim Antunes, Romeu Rocha, and Francisco P. Brito. "Heat-pipe assisted thermoelectric generators for exhaust gas applications." In ASME 2010 *International Mechanical Engineering Congress and Exposition*, pp. 1387-1396. American Society of Mechanical Engineers, 2010.

[37] Martins, Jorge, Francisco P. Brito, L. M. Goncalves, and Joaquim Antunes. "Thermoelectric exhaust energy recovery with temperature control through heat pipes." (2011).

[38] Brito, F. P., Jorge Martins, L. M. Goncalves, Nuno Antunes, and Diogo Sousa. "Influence of heat pipe operating temperature on exhaust heat thermoelectric generation." *SAE International Journal of Passenger Cars-Mechanical Systems* 6, no. 2 (2013): 652-664.

[39] Brito, Francisco P., Jorge Martins, L. M. Goncalves, and Rui Sousa. "Modelling of thermoelectric generator with heat pipe assist for range extender application." In IECON 2011-37th *Annual Conference on IEEE Industrial Electronics Society*, pp. 4589-4595. IEEE, 2011.

[40] Date, Ashwin, Abhijit Date, Chris Dixon, and Aliakbar Akbarzadeh. "Theoretical and experimental study on heat pipe cooled thermoelectric generators with water heating using concentrated solar thermal energy." *Solar Energy* 105 (2014): 656-668.

[41] Kim, Pan-Jo, Seok-Ho Rhi, Kye-Bock Lee, Hyun-Chang Hwang, Ji-Su Lee, Ju-Chan Jang, Wook-Hyun Lee, and Ki-Woo Lee. "Heat-Pipe-Associated Localized Thermoelectric Power Generation System." *Journal of Electronic Materials* 43, no. 6 (2014): 1613-1619.

[42] Dell, Robert, Runar Unnthorsson, C. S. Wei, George W. Sidebotham, Magnus Thor Jonsson, William Foley, Eric Ginzburg, Subashis Paul, Seyoon Kim, and Anthony Morris. "Thermoelectric-based Power Generator For Powering Microcontroller Based Security Camera." In ASME 2012 *International Mechanical Engineering Congress and Exposition*, pp. 635-642. American Society of Mechanical Engineers, 2012.

[43] Remeli, M., Abhijit Date, B. Bhathal Singh, Lippong Tan, and Aliakbar Akbarzadeh. "Power generation and heat recovery using heat pipe thermoelectric generator (HPTEG)." *In SOLAR* 2014, pp. 1-9. Australian Solar Council, 2014.

[44] Maharaj, S., and Poobalan Govender. "A prototype thermoelectric co-generation unit." In Domestic Use of Energy (DUE), 2014 *Proceedings of the Twenty-Second*, pp. 1-6. IEEE, 2014.

[45] Tewolde, Mahder, Chih Chieh Lin, He Tao, Hanfei Chen, Gaosheng Fu, Di Liu, Tao Zhang et al. "Sensors for Small Modular Reactors Powered by Thermoelectric Generators." In ASME 2014 *Small Modular Reactors Symposium*, pp. V001T02A007-V001T02A007. American Society of Mechanical Engineers, 2014.

[46] Akaydin, Huseyin Dogus, Niell Elvin, and Yiannis Andreopoulos. "Energy harvesting from highly unsteady fluid flows using piezoelectric materials." *Journal of Intelligent Material Systems and Structures* 21, no. 13 (2010): 1263-1278.

[47] Kwon, Soon-Duck. "A T-shaped piezoelectric cantilever for fluid energy harvesting." *Applied Physics Letters* 97, no. 16 (2010): 164102.

[48] Arafa, M., W. Akl, M. Majeed, K. Al-Hussain, and A. Baz. "Energy harvesting of gas pipeline vibration." In SPIE *Smart Structures and Materials+ Nondestructive Evaluation and Health Monitoring*, pp. 76430L-76430L. International Society for Optics and Photonics, 2010.

[49] Hoffmann, D., A. Willmann, R. Göpfert, P. Becker, B. Folkmer, and Y. Manoli. "Energy harvesting from fluid flow in water pipelines for smart metering applications." In *Journal of Physics: Conference Series*, vol. 476, no. 1, p. 012104. IOP Publishing, 2013.

[50] Zhao, Dongliang, and Gang Tan. "A review of thermoelectric cooling: materials, modeling and applications." *Applied Thermal Engineering* 66, no. 1 (2014): 15-24.

[51] Fraisse, G., J. Ramousse, D. Sgorlon, and C. Goupil. "Comparison of different modeling approaches for thermoelectric elements." *Energy Conversion and Management* 65 (2013): 351-356.

[52] Chen, Lingen, Jianzheng Gong, Fengrui Sun, and Chih Wu. "Effect of heat transfer on the performance of thermoelectric generators." *International Journal of Thermal Sciences* 41, no. 1 (2002): 95-99.

[53] Chen, Jincan, Zijun Yan, and Liqing Wu. "The influence of Thomson effect on the maximum power output and maximum efficiency of a thermoelectric generator." *Journal of applied physics* 79, no. 11 (1996): 8823-8828.

[54] Sahin, Ahmet Z., and Bekir S. Yilbas. "The thermoelement as thermoelectric power generator: effect of leg geometry on the efficiency and power generation." *Energy Conversion and Management* 65 (2013): 26-32.

[55] Rodríguez, A., J. G. Vián, D. Astrain, and A. Martínez. "Study of thermoelectric systems applied to electric power generation." *Energy Conversion and Management* 50, no. 5 (2009): 1236-1243.

[56] Chen, Lingen, Jun Li, Fengrui Sun, and Chih Wu. "Performance optimization of a two-stage semiconductor thermoelectric-generator." *Applied energy* 82, no. 4 (2005): 300-312.

[57] Rowe, D. M., and Gao Min. "Evaluation of thermoelectric modules for power generation." *Journal of Power Sources* 73, no. 2 (1998): 193-198.

[58] Hsiao, Y. Y., W. C. Chang, and S. L. Chen. "A mathematic model of thermoelectric module with applications on waste heat recovery from automobile engine." *Energy* 35, no. 3 (2010): 1447-1454.

[59] Gou, Xiaolong, Heng Xiao, and Suwen Yang. "Modeling, experimental study and optimization on low-temperature waste heat thermoelectric generator system." *Applied energy* 87, no. 10 (2010): 3131-3136.

[60] He, Wei, Yuehong Su, S. B. Riffat, JinXin Hou, and Jie Ji. "Parametrical analysis of the design and performance of a solar heat pipe thermoelectric generator unit." *Applied Energy* 88, no. 12 (2011): 5083-5089.

[61] Jaegle, Martin, Markus Bartel, Dirk Ebling, A. Jacquot, and H. Böttner. "Multiphysics simulation of thermoelectric systems." (2008).

[62] Wang, Chien-Chang, Chen-I. Hung, and Wei-Hsin Chen. "Design of heat sink for improving the performance of thermoelectric generator using two-stage optimization." *Energy* 39, no. 1 (2012): 236-245.

[63] Weng, Chien-Chou, and Mei-Jiau Huang. "A simulation study of automotive waste heat recovery using a thermoelectric power generator." *International journal of thermal sciences* 71 (2013): 302-309.

[64] Newman, Jay (2008). *Physics of the Life Sciences*. Springer. p. 652. ISBN 978-0-387-77258-5.

[65] *Nuclear Power Reactors*. Available: http://www.world-nuclear.org/info/Nuclear-Fuel-Cycle/Power-Reactors/Nuclear-Power-Reactors/

[66] "Nuclear Reactor Types" The Institute of Engineering and Technology 2008.

[67*] The Westinghouse pressurized water reactor nuclear power plant*. Westinghouse

[68] *BWR Description*. Available: http://ocw.mit.edu/courses/nuclear-engineering/22-06-engineering-of-nuclear-systems-fall-2010/lectures-an readings/MIT22_06F10_lec06b.pdf

[69] Houssay, Laurent P. "Robotics and radiation hardening in the nuclear industry." PhD diss., University of Florida, 2000.

[70] Blizard, E. P. "Nuclear radiation shielding." *Annual review of nuclear science* 5, no. 1 (1955): 73-98.

[71] Lundgren, Klas. "Radiation levels and absorbed doses around copper canisters containing spent LWR fuel." *Thecnical report*: SKBF/KBS (1982): 82-11.

[72] A. Bar-Cohen and W. Rohsenow, "Thermally optimum spacing of vertical, natural convection cooled, parallel plates," *Journal of Heat Transfer*, vol. 106, pp. 116-123, 1984.

[73] *How to select a heat pipe*. Available: https://www.enertron-inc.com/enertron-resources/PDF/How-to-select-a-heat-pipe.pdf

[74] Reay, David, Ryan McGlen, and Peter Kew. *Heat pipes: Theory, design and applications*. Butterworth-Heinemann, 2013.

[75] Rohsenow, Warren M. *A method of correlating heat transfer data for surface boiling of liquids. Cambridge*, Mass.: MIT Division of Industrial Cooporation, 1951.

[76] Brito, Francisco P., Jorge Martins, L. M. Goncalves, and Rui Sousa. "Modelling of thermoelectric generator with heat pipe assist for range extender application." In *IECON 2011-37th Annual Conference on IEEE Industrial Electronics Society*, pp. 4589-4595. IEEE, 2011.

[77] Guitart Corominas, Joaquim. "Heat sink analytical modelling." (2010).

[78] Yovanovich, M. M., and E. E. Marotta. "Thermal spreading and contact resistances." *Heat Transfer Handbook* 1 (2003): 261-394.

[79] Culham, J. Richard, M. Michael Yovanovich, and Sen Lee. "Thermal modeling of isothermal cuboids and rectangular heat sinks cooled by natural convection." *Components, Packaging, and Manufacturing Technology, Part A, IEEE Transactions* on 18, no. 3 (1995): 559-566.

[80] Bejan, Adrian, and Allan D. Kraus. *Heat transfer handbook*. Vol. 1. John Wiley & Sons, 2003.

[81] Lineykin, Simon, and Shmuel Ben-Yaakov. "Modeling and analysis of thermoelectric modules." *Industry Applications, IEEE Transactions* on 43.2 (2007): 505-512.

[82] Bitschi, Andreas. "Modelling of thermoelectric devices for electric power generation." PhD diss., Diss., Eidgenössische Technische Hochschule ETH Zürich, Nr. 18441, 2009, 2009.

[83] Spieler, Helmuth. "Introduction to radiation-resistant semiconductor devices and circuits." In *AIP Conference Proceedings*, pp. 23-49. IOP INSTITUTE OF PHYSICS PUBLISHING LTD, 1997.

[84] Nikjoo, Hooshang, Shuzo Uehara, and Dimitris Emfietzoglou. *Interaction of radiation with matter*. CRC Press, 2012.

[85] Makowski, Dariusz. "The impact of radiation on electronic devices with the special consideration of neutron and gamma radiation monitoring." *Zeszyty Naukowe. Elektryka/Politechnika Łódzka* 111 (2007): 73-80.

[86] Oldham, Timothy R., and F. B. McLean. "Total ionizing dose effects in MOS oxides and devices." *IEEE Transactions on Nuclear Science* 50, no. 3 (2003): 483-499.

[87] Messenger, George C., and Milton S. Ash. "The effects of radiation on electronic systems." (1986).

[88] Sexton, Fred W. "Destructive single-event effects in semiconductor devices and ICs." *IEEE Transactions on Nuclear Science* 50, no. 3 (2003): 603-621.

[89] McAlister, Daniel R. "Gamma ray attenuation properties of common shielding materials." *University Lane Lisle*, USA (2012).

[90] Mukherjee, Biswanath, D. Makowski, D. Rybka, O. Kroeplin, S. Simrock, and H. J. Eckoldt. "External radiation shielding for the protection of electronic devices operating in the FLASH facility tunnel at DESY." In *Mixed Design of Integrated Circuits and System, 2006. MIXDES 2006. Proceedings of the International Conference*, pp. 65-68. IEEE, 2006.

[91] Featherby, Michael, David J. Strobel, Phillip J. Layton, and Edward Li. "Methods and compositions for ionizing radiation shielding." U.S. Patent 6,455,864, issued September 24, 2002.

[92] Dlugokecki, Joseph J., and Joseph R. Florian. "Radiation shielding for integrated circuit devices using reconstructed plastic packages." U.S. Patent 5,406,117, issued April 11, 1995.

[93] Strobel, David J., and David R. Czajkowski. "Radiation shielding of plastic integrated circuits." U.S. Patent 5,825,042, issued October 20, 1998.